UNIONE EUROPEA
Fondo Sociale Europeo
Ministero dell'Università e della Ricerca
PON RICERCA E INNOVAZIONE 2014 - 2020
REACT EU
UNIVERSITÀ DEGLI STUDI DI MILANO BICOCCA

SCUOLA DI DOTTORATO
UNIVERSITÀ DEGLI STUDI DI MILANO-BICOCCA

Department of Environmental and Earth Sciences

PhD program in Chemical, Geological, and Environmental Sciences

XXXVII Cycle

Curriculum in Geological Sciences

BICMIB - Blue-green infrastructures for the City of Milano in Bicocca – hydro-thermal groundwater modelling for geothermal systems development

Silvestri Valerio

Registration number 893265

Supervisor: Prof. Paolo Frattini

Tutor: Prof. Giovanni Crosta

Coordinator: Marco Giovanni Malusà

ACADEMIC YEAR 2024-2025

Abstract

Severe and extreme weather events, such as droughts and floods, have increasingly impacted human-environment systems and are expected to intensify. Addressing this challenge is essential to build sustainable and resilient cities. This can be achieved through two complementary strategies: implementing Blue-Green Infrastructures for water and vegetation management and reducing CO_2 emissions to mitigate climate change impacts. Blue-Green Infrastructures are designed to improve water management, promote biodiversity, reduce urban heat islands, and alleviate flood risks. This approach aligns with the European Green Deal's goals, which include significant reductions in CO_2 emissions by utilizing renewable energy sources like geothermal energy. In this study, a particular focus is given to low-enthalpy shallow geothermal systems, which are notably suitable and efficient in urban environments. The study area considered is the Milan Metropolitan Area, which is one of the most densely populated and industrialized regions in Europe.

One important aspect analysed was the thermal properties of soils under different saturation levels using and confronting two different instruments applied for this scope, aiming to create a reliable methodology to obtain accurate values of thermal conductivity. Applying these tools can provide fundamental parameters for estimating the energy potential of geothermal systems.

Additionally, were also investigated the hydrogeological parameters that govern Milan's Metropolitan Area shallow aquifer. Retrieving trustworthy hydraulic conductivity values from grain size distribution analysis and classifying the considered layers in hydrofacies supported a deeper understanding of the local's geological and hydraulic properties of the underground.

Several numerical modelling were generated utilizing 3D finite-difference models with MODFLOW to simulate groundwater flow and thermal transport. The objective was to assess various geothermal system configurations. The findings revealed the importance of tailoring geothermal systems to the specific thermal and hydraulic properties of soils and groundwater. Optimal design significantly enhances systems' efficiency, demonstrating the feasibility of improving energy production by installing specific geothermal configurations.

An additional contribution was given by the municipality of Milan, which provided permits issued for the construction of geothermal systems in the city, in this way was possible to apply the theoretical outcomes to real case studies with arithmetic and statistical analysis. The database, developed through the digitalization and standardization of permit data, allowed the creation of spatial analyses of system performance. It also facilitates feasibility assessments for retrofitting existing installations into non-conventional configurations, offering a pathway to enhance efficiency and sustainability at a regional scale.

Overall, the study underscores the potential of geothermal systems to contribute to urban sustainability by integrating energy and water management while reducing greenhouse gas emissions. By leveraging advanced modelling techniques and high-resolution data, the research provides a replicable framework for implementing geothermal solutions in metropolitan areas, addressing both environmental and socio-economic challenges.

Riassunto

Gli eventi meteorologici estremi, come siccità e inondazioni, hanno avuto un impatto crescente sui sistemi uomo-ambiente e si prevede che tali fenomeni si intensifichino ulteriormente. Per affrontare questa sfida, è essenziale creare città sostenibili e resilienti. Questo obiettivo può essere raggiunto attraverso due strategie complementari: l'implementazione di infrastrutture blu-verdi per la gestione delle risorse idriche e della vegetazione e la riduzione delle emissioni di CO_2 per mitigare gli effetti del cambiamento climatico. Le infrastrutture blu-verdi sono progettate per migliorare la gestione idrica, promuovere la biodiversità, ridurre l'effetto isola di calore urbana e alleviare i rischi di inondazione. Tale approccio è in linea con gli obiettivi del Green Deal europeo, che include una significativa riduzione delle emissioni di CO_2 attraverso l'uso di fonti di energia rinnovabile come l'energia geotermica. In questo studio, particolare attenzione è rivolta ai sistemi geotermici a bassa entalpia, specialmente adatti ed efficienti negli ambienti urbani.

L'area di studio considerata è la Città Metropolitana di Milano, una delle regioni più densamente popolate e industrializzate d'Europa.

Un aspetto importante analizzato riguarda le proprietà termiche dei suoli a diversi livelli di saturazione, utilizzando e confrontando due strumenti differenti progettati per questo scopo con l'obiettivo di creare una metodologia affidabile per ottenere valori accurati di conducibilità termica. L'applicazione di tali strumenti fornisce parametri fondamentali per stimare il potenziale energetico dei sistemi geotermici.

Inoltre, sono stati indagati i parametri idrogeologici che governano la falda superficiale dell'area metropolitana di Milano. L'ottenimento di valori attendibili di conducibilità idraulica attraverso l'analisi della distribuzione granulometrica e la classificazione degli strati considerati in idrofacies ha supportato una comprensione più approfondita delle proprietà geologiche e idrauliche del sottosuolo locale.

Sono stati generati numerosi modelli numerici utilizzando modelli a differenze finite tridimensionali con MODFLOW per simulare il flusso delle acque sotterranee e il trasporto termico. L'obiettivo era valutare diverse configurazioni di sistemi geotermici. I risultati evidenziano l'importanza di adattare i sistemi geotermici alle specifiche proprietà termiche e idrauliche dei suoli e delle acque sotterranee. Un design ottimale migliora significativamente l'efficienza dei sistemi, dimostrando la fattibilità di incrementare la produzione energetica attraverso l'installazione di configurazioni geotermiche specifiche.

Un ulteriore contributo è stato fornito dal Comune di Milano, che ha messo a disposizione i permessi rilasciati per la costruzione di sistemi geotermici nella città. Grazie a questi dati è stato possibile applicare i risultati teorici a casi studio reali attraverso analisi aritmetiche e statistiche. Il database, sviluppato mediante la digitalizzazione e standardizzazione dei dati relativi ai permessi, ha consentito la creazione di analisi spaziali delle prestazioni dei sistemi. Ha inoltre facilitato le valutazioni di fattibilità per la riconversione di installazioni esistenti in configurazioni non convenzionali, offrendo un percorso per migliorare l’efficienza e la sostenibilità su scala regionale.

Nel complesso, lo studio sottolinea il potenziale dei sistemi geotermici di contribuire alla sostenibilità urbana integrando la gestione energetica e idrica, riducendo al contempo le emissioni di gas serra. Sfruttando tecniche avanzate di modellizzazione e dati ad alta risoluzione, la ricerca fornisce un quadro replicabile per l’implementazione di soluzioni geotermiche nelle aree metropolitane, affrontando sia le sfide ambientali che quelle socioeconomiche.

Table of contents

4. Hydrogeological parameterisation 47

5. Numerical model generation 61

List of abbreviations and acronyms

3D	Three dimensional
AI	Artificial intelligence
ATES	Aquifer thermal energy storage
BGIs	Blue-green infrastructures
C	Clay
C+S	Clay and silt
CAPEX	Capital expenditure
CC	Climate change
FDM	Finite difference numerical model
G	Gravel
GHG	Greenhouse gas
GSHP	Ground source heat pump
GW	Groundwater
GWHP	Groundwater heat pump
LID	Low impact developments
LSTM	Long short-term memory
MCM	Metropolitan City of Milan
MM	Metropolitans of Milan
MoM	Municipality of Milan
MUSA	Multilayered Urban Sustainability Action
NBS	Natural based solutions
NLP	Natural language processing
O-L	Conventional open-loop
OPEX	Operating costs
S	Sand
SuDS	Sustainable drainage systems
UD-ATES	Uni-directional ATES
UHI	Urban heat island
WSUD	Water-sensitive urban design
XRD	X-ray diffraction

List of figures

List of tables

List of equations

1. Introduction

1.1 Theoretical background

Severe and extreme weather events (droughts/floods) have become an accepted part of human-environment systems over the last decade and are likely to become more intense and frequent in the future. This highlights the exposure and vulnerability of many natural and human ecosystems. This is also true for urban environments, which tend to become larger and more densely populated. Nowadays 55% of the world's population is living in urban areas and the predictions from the United Nations report in 2018 on the world urbanisation prospects are 68% of the global population living in urbanised areas (United Nations, 2018). The creation of more sustainable and resilient cities to Climate Change (CC) is imperative to allow the increment of population and, at the same time, to mitigate the effects of CC events affecting the inhabitants of urbanized areas. To reduce the impacts related to CC it is fundamental to tackle this issue using two combined solutions, implementing at a city scale Blue (water management) - Green (vegetation) Infrastructures (BGIs) and reducing the CO_2 emissions.

1.1.1 Blue-Green infrastructures

BGIs can be called by different names according to the scope they are addressed to solve, among others Low Impact Developments (LID), Water-Sensitive Urban Design (WSUD), Sustainable Drainage Systems (SuDS), or again Nature-Based Solutions (NBS) (Fletcher et al., 2015). As it is shown, BGIs do not have a specific definition because they gather several aspects in their meaning, but all of them are used to address societal challenges (e.g. climate change, food and water security, pollution control, or natural disaster mitigation). It can be considered to include all artificial, natural, and semi-natural multifunctional environmental systems around, within, and between urban areas (Ghofrani et al, 2017). The European Commission has developed a Green Infrastructure Strategy, aiming to ensure that the protection, restoration, creation, and enhancement of green infrastructure become an integral part of spatial planning and territorial development whenever it offers a better alternative, or it is complementary, to standard grey choices (European Commission, 2019). It includes features like parks, green roofs, rain gardens, wetlands, and permeable surfaces, which help to enhance biodiversity, improve air quality, manage stormwater, and provide recreational spaces. Grey infrastructures are not capable any more to cope sever CC events (Mohammed et al., 2021), especially while becoming more frequent and intense in the future; furthermore, they are considered to damage the environment and biodiversity, resulting also in being more expensive to build and maintain compared to BGIs (Wild et al., 2024). One of the best examples for applying this methodology in urban environments is given by depaving cemented areas such as squares or parking lots, by replacing the asphalt with soil and grass several benefits will arise. The green area will decrease the surface temperature during summer's heat waves, the grass will lead to an increment of biodiversity (insects and plants) and finally, the soil will be capable of draining the rainwater in the aquifer helping its recharge and enhancing the water management (Aimar, 2023; Brear, 2018). An example of this technique is given by the depaving works carried out in one of the main squares of Bicocca University (Piazza della Scienza) between 2023 and 2024. Sewers, as an example of grey infrastructure, are not adequate anymore to face extreme events (Wild et al., 2024); manhole clogging is one of the most frequent reasons for urban and sub-urban flooding (Beg et al., 2018). Another factor is given by burying streams or rivers in urbanized areas to obtain more freedom on where to develop new buildings, but on the other side, when an extreme event occurs the water level of the buried stream/river can rise to the street level, causing floods. Therefore, BGIs not only help to mitigate the CC effects, but can also secure healthy environments and health improvements, including physical and mental health, for people residing within and close to it (Tzoulas et al., 2007).

This project follows up on the findings of De Caro et al. (2019), which examined the influence of Milan's BGIs on groundwater (GW) levels and the sustainability of future urban development. The study's objective was to mitigate underground facility flooding caused by a GW rebound consequent to the industrial decline, which led to a reduction in GW abstraction during the 1990s. As previously stated, the implementation of BGIs would enhance water resilience by integrating green spaces for natural water management, improving air quality, and supporting local ecosystems. To evaluate the impact of BGIs a numerical model was developed to simulate the GW flow. This model was used to estimate the potential usage of GW from decommissioned rail yards for irrigation and geothermal energy. The results demonstrate that strategic BGIs implementations can confer ecological and social benefits while reducing CO_2 emissions through geothermal energy (Hähnlein et al., 2012), thereby ensuring integrated water and energy management. The 2019 study has been continued with an emphasis on the energetic management gained from the aquifer through the utilisation of geothermal energy.

1.1.2 CO_2 emission reduction

The European plan proposed in July 2021 in the context of the European Green Deal (Fit for 55), requires all member states to reduce their greenhouse gas (GHG) emissions by 55% before 2030, as an intermediate step towards the net zero goal by 2050 aiming to limit the global warming to 1.5°C compared to pre-industrial levels (European Council, 2020). Hence, European cities are adopting sustainable energy systems to reach this objective. Heating and cooling of buildings accounted for 54% of the total GHG emissions in Italy in 2018 (Legambiente, 2021), in Europe decreases to 36% (European Council, 2020), and across the world, it contributes to about 40% of all primary energy use (IRENA, 2023). Ground source/water heat pumps are a renewable solution that many countries are adopting to replace fossil-based heating and cooling techniques (Banks, 2009). Such systems use the ground and/or GW to reject, extract, and/or store thermal energy underground.

1.1.3 Earth's internal energy

Geothermal energy is the thermal energy stored in the Earth's body. It derives from two sources:

- One is driven by the radioactive decay of elements like potassium, uranium, and thorium located in the Earth's interior (crust and mantle);
- The other source is the conduction of heat from the hot core (5,800°C the same temperature as the Sun surface) to the crust generated by the Earth formation process.

For this reason, 99% of the Earth's volume has a temperature higher than 1,000°C, while just 0.1% of it is colder than 100°C. Therefore, the temperature difference between the core and the crust produces a heat flux, which is driven by Fourier's' conduction law, so the terrestrial heat flow is the amount of energy (*J*) transferred through a unit surface area of 1 m^2 per unit time (*s*) and is referred as heat flow density (q) (eq. 1), expressed by Fourier's' equation:

$$q = -\lambda \cdot \nabla T \ \ [J\, s^{-1}\, m^{-2}] \qquad \text{(Eq. 1.1)}$$

Where λ is the thermal conductivity. The average global surface heat flow density of the Earth is about 65 mW/m^2.

The thermal conductivity (λ) controls the supply of thermal energy for a given temperature gradient, in other words controls the ability of materials to transport heat and is specific for different materials. Other aspects that contribute to reducing the thermal conductivity are anisotropies or loose materials (Woodside et al., 1961) (**Table 1.1**).

Once the thermal conductivity is defined, can be introduced the heat capacity (*C*) (eq. 2) which is the amount of heat that can be stored in the sub-surface. In other words, the amount of heat that is taken or released by a rock triggered by a temperature change (*ΔT*) of 1 K, described by the following formula:

$$C = \frac{\Delta Q}{\Delta T} \; [J\ K^{-1}] \qquad \text{(Eq. 1.2)}$$

The heat capacity for unite mass defines the specific heat capacity (*c*) (eq. 3), while if the heat capacity is normalised to a constant volume represents the volumetric heat capacity (*s*) (eq. 4), and both are expressed respectively by the two following equations:

$$c = \frac{\Delta Q}{m \cdot \Delta T} \; [J\ kg^{-1}\ K^{-1}] \qquad \text{(Eq. 1.3)}$$

$$s = \frac{\Delta Q}{V \cdot \Delta T} \; [J\ m^{-3}\ K^{-1}] \qquad \text{(Eq. 1.4)}$$

Using the density (*ρ*) it is possible to pass from one formula to the other (eq. 5), with the following relation:

$$c = \frac{s}{\rho} \qquad \text{(Eq. 1.5)}$$

Table 1.1 - Representative thermal conductivity values and specific heat capacity of different materials. Data for 25°C and 1 bar condition. Kappelmeyer & Haenel (1974).

Rock/fluids	**Thermal conductivity (λ) [J s^{-1} m^{-1} K^{-1}]**	**Specific heat capacity (c) [kJ kg^{-1} K^{-1}]**
Gravel, sand dry	0.3 – 0.8	0.50 – 0.59
Gravel, sand wet	1.7 – 5.0	0.85 – 1.90
Clay, loam moist	0.9 – 2.3	0.80 – 2.30
Limestone	2.5 – 4.0	0.80 – 1.00
Dolomite	1.6 – 5.5	0.92 – 1.06
Marble	1.6 – 4.0	0.86 – 0.92
Sandstone	1.3 – 5.1	0.82 – 1.00
Shale	0.6 – 4.0	0.82 – 1.18
Granite	2.1 – 4.1	0.75 – 1.22
Gneiss	1.9 – 4.0	0.75 – 0.90
Basalt	1.3 – 2.3	0.72 – 1.00
Quartzite	3.6 – 6.6	0.78 – 0.92
Rocksalt	5.4	0.84
Air	0.02	1.0054
Water	0.59	4.12

Rocks and sediments have high values of volumetric heat capacity (*s*), but from low to modest values of thermal conductivity (*λ*). Therefore, the thermal diffusivity is low as well, since this parameter is calculated by the ratio of the other two variables mentioned (*λ/s*). For this reason, the intense solar radiation and the elevated air temperatures in summer heat up the Earth's surface, but the heating effect does not propagate fast or far, only a few meters underground; at lower depths, the sub-surface temperature is remarkably stable, a value close to the long-term mean annual average surface temperature.

Since water has even lower values of thermal conductivity compared to rocks, the thermal signal propagation is slower (Constantz, 1998). **Figure 1.1** shows the propagation of the thermal signal from the air to the water of a river and in the GW. It is visible how the pick value of the river's temperature is close to a one-month delay compared to the spike in the air temperature. The GW shows almost no thermal signal derived from the air temperature.

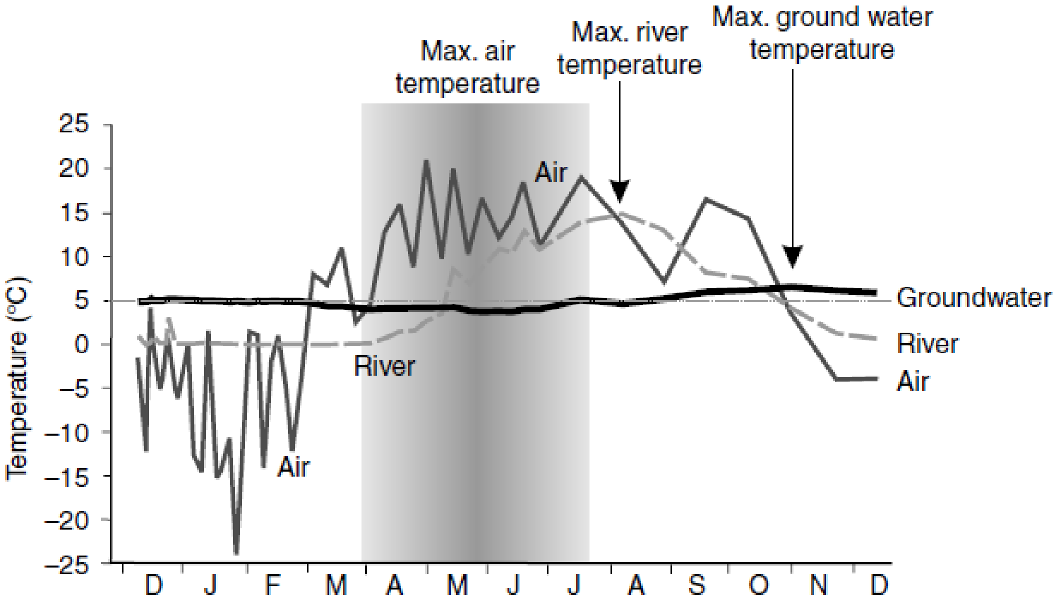

Figure 1.1 - Seasonal temperature variation of air, river, and groundwater (from Ertuğrul et al., 2018).

The annual average air temperature differs slightly from the annual average soil temperature because different factors affect the Earth's surface, such as:

- Amount of solar radiation and heat transfer efficiency between soil and atmosphere;
- Aspect of the terrain (south-sloping or north-sloping);
- Vegetation cover;
- Soil moisture (precipitations) which changes along with the seasons;

- Snow cover, which increases the reflection of incoming solar radiation and decreases the absorption of solar energy.

Anyhow, the seasonal ground temperature variations decrease with depth, and the annual cycle disappears at a depth comprised of between 10 and 20 m. With the gradual increase in depth, the temperature rises as well according to the local geothermal gradient (**Figure 1.2**). Earth's mean geothermal gradient, outside of anomalous or volcanically active areas, is assessed to be 1 - 3°C for every hundred meters (Kolawole & Evenick, 2023), having a geothermal heat flux comprised between 10 and 40 mW/m^2.

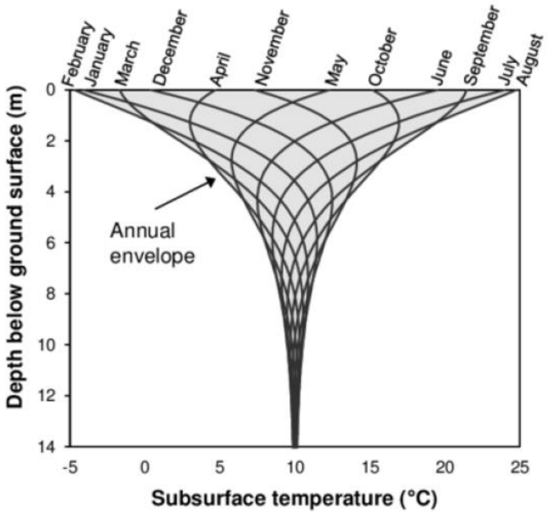

Figure 1.2 - Temperature-depth profile up to 14 m during one year showing the seasonal fluctuation drop with depth (from Kurylyk et al., 2015).

1.1.4 Sub-Urban Heat Island (SUHI) effect

In specific conditions, such as urban environments, the geothermal gradient may be reversed, especially in the shallowest part of the ground, meaning that the surface temperature is higher compared to the one recorded underground (Ferguson & Woodbury, 2004). The main reason for this is due to the Urban Heat Island (UHI) effect, this condition arises when the vegetation in cities is very scarce and most of it has been replaced by roads and buildings (asphalt and concrete), increasing dramatically the air temperature in summer and less in winter (Yang et al., 2016; Gago et al., 2013). The propagation of thermal signals from the atmosphere to the subsurface has led to the definition of the Sub-Urban Heat Island (SUHI) effect. This phenomenon has been extensively documented in various urban settings, including Basel (Epting and Huggenberger, 2013), Cardiff

(Farr et al., 2017), and Paris (Hemmerle et al., 2019). Further studies have explored the SUHI effect in six German cities (Menberg et al., 2013a), Milan (Previati and Crosta, 2021a), and Amsterdam (Visser et al., 2020), highlighting its diverse manifestations and implications across different geographical contexts (Bayer et al., 2019; Zhu et al., 2010). SUHI lead to enhance the temperature of the shallowest underground and GW (**Figure 1.3**). Urbanized cities located at high latitudes, having underground aquifers affected by the SUHI effect can transform this issue into a resource by implementing open-loop geothermal systems for heating/cooling buildings, since the SUHI effect will enhance the temperature of the aquifer, allowing to heat the buildings with a greater efficiency (Bayer et al., 2019). On the other hand, cities located at lower latitudes need to configure their geothermal systems in specific ways to avoid enhancing the already high temperature (caused by the SUHI effect) of the aquifer, due to the energy required for cooling down the buildings being greater compared to the one in winter.

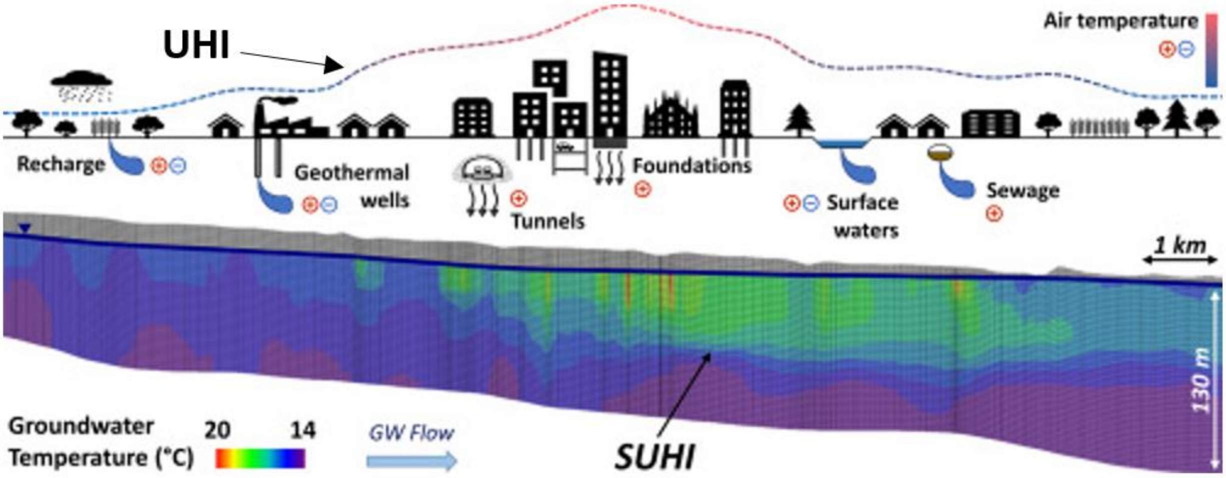

Figure 1.3 - Temperature variations of air (UHI) and groundwater (SUHI) from the outer skirt to the city centre (from Previati et al., 2022).

1.1.5 Geothermal systems

Geothermal systems are classified according to the enthalpy contained in the underground, in other words, according to the amount of thermal energy that a geothermal system can exchange with the underground. High enthalpy geothermal systems are characterized by temperatures greater than

150°C, in mid-enthalpy systems the temperature is comprised of between 150 and 90°C, and finally, low enthalpy systems are characterized by temperatures lower than 90°C.

- High enthalpy geothermal systems are the most productive in terms of electric energy due to the high temperature and pressure of the aquifer system (Scott et al., 2016). These conditions are met for example in areas with an active or crystalized shallow magmatic chamber.
- In geothermal systems characterized by mid-enthalpy, the temperature is comprised between 150 and 90°C and needs to be extracted at a maximum depth of 2 Km. These conditions are obtained using deep drilling techniques, allowing to reach deep parts of the crust, the greater the depth higher the extraction temperature will be (Vardon et al., 2020). The presence of radioactive elements in the underground, which contribute to the generation of positive thermal anomalies through their decay, plays a significant role in increasing subsurface temperatures. This characteristic presents a substantial advantage for deep-drilled geothermal systems.
- Shallow geothermal systems, while less productive compared to the previously described alternatives, are the most widely adopted globally due to their reliance on shallow drilling (maximum depth of 200 m), which significantly reduces drilling costs. To address the challenge of extracting low-temperature groundwater, these systems must be integrated with a heat pump. This tool elevates the fluid temperature for heating during the winter months, whereas in summer, it is generally unnecessary due to the use of free cooling (groundwater is utilized directly at its natural extraction temperature). Additionally, their widespread popularity can be attributed to their versatility, as they can be installed across a broad range of geological conditions (Bayer et al., 2019; Al-Khoury, 2012; Bundschuh et al., 2010; Saner et al., 2010).

1.1.6 Low enthalpy geothermal systems

This project will focus on low-enthalpy geothermal systems since they are the most widespread in cities where aquifers are located underground. Low enthalpy geothermal systems are based on which type of media the energy is exchanged, so open-loop systems, in which the energy is exchanged with the GW (Groundwater Heat Pump) (GWHP), or closed-loop systems where the energy is exchanged with the underground (Ground Source Heat Pump) (GSHP).

Open-loop geothermal systems

Aquifers are the easiest geothermal resource to exploit for extracting thermal energy since they already contain fluids. Open-loop geothermal systems exchange the energy with the GW of aquifers, which are widely spread in many European cities. The pumps immersed in the wells extract water from the underground, which then passes into the heat pump (**Figure 1.4**). Depending on the season, it increases or decreases the water pressure and thus the temperature, allowing it to exchange energy with the building. Once the thermal energy in the extracted water is consumed, it enters again the heat pump, increasing/decreasing its pressure and, as a result, its temperature. Finally, water is re-injected into the aquifer at a different temperature from that at which it was extracted (Self et al., 2013). The following section will analyse the costs and the efficiency of these geothermal systems:

- A deep hydrological planning of the system is mandatory to assess the qualitative and quantitative impact on the aquifer by using numerical models. This leads to an increment in the planning and installation cost compared to closed-loop systems, for which this step is not required;
- The installation costs include the well's drilling (variable price according to the depth intended to reach, usually less compared to closed-loop systems), laying of the pipelines, the submerged pumps (the one for extracting the water and, if necessary also for re-injecting it) and finally, the heat pump.
- Other costs are attributable to the operation of the geothermal plant, mainly to the maintenance of the pumps (both for lifting and injecting the water and the heat pump), the pipelines, and the filters, which could become clogged.
- The power produced is strictly related to the thermal properties of the aquifer (grain size and mineral composition of the grains that characterise the aquifer's horizons) and by the hydraulic properties of the aquifer, such as productivity, transmissivity and thickness, but also to the type of heat pump installed.

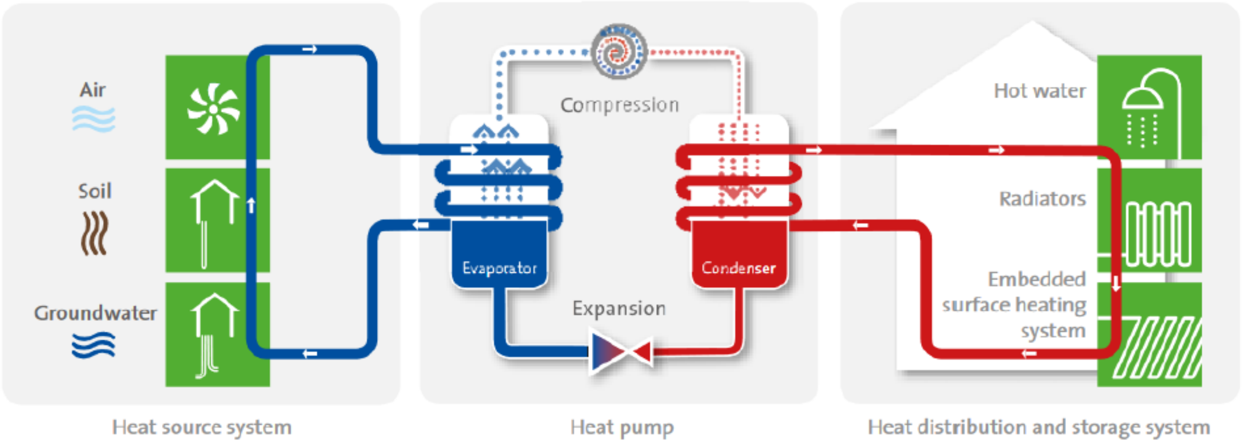

Figure 1.4 - Operational scheme of a commune heat pump. In winter, the energetic element is extracted from the source and enters the compressor in which the element evaporates increasing its heat. Once the energy is collected, the element enters the expansion valve in which the element is condensed decreasing its pressure and consequently its heat, for being re-injected in the source. In summer, the cycle is reversed (from Lyons et al., 2022).

Closed-loop geothermal systems

In closed-loop systems (**Figure 1.5**) there is no fluid exchange with the underground, only thermal energy exchange occurs (Bayer et al., 2012; Blum et al. 2010; Kavanaugh et al., 2014). These systems are usually located in boreholes as probes or poles installed with coil tubes inside them, into which a carrier liquid flows (usually a solution of water and glycol, to prevent freezing in the pipes). In winter the probe absorbs heat transporting it to the surface enters the heat pump, exchanges heat with the building, and then back again into the probe. As in open-loop systems, the process is reversed during the summer season. To facilitate the heat exchange, the fluid is brought at temperatures of 10/15°C lower or higher compared to the sub-surface temperature, depending on whether the thermal energy is being extracted or released. Closed-loop systems can be extremely advantageous as they can be installed also in the piles used to construct the foundations of the buildings (Fadejev et al., 2017). The same is valid also for horizontal closed-loop systems placed in the shallowest part of the sub-surface like small basins, trenches, or tunnels. Piles or diaphragms are considered energy geo-structures as they fulfil two different functions: guarantee the stability of the structure and extract thermal energy from the underground. The costs and the efficiency of these geothermal plants will be analysed in the following section.

- The installation cost comprises drilling the boreholes and the installation of the probes, also in this case it depends on the drilling depth, (if are designed as foundation piles for the building, it is considered only the cost to install the coils in the piles) and the heat pump;
- The maintenance costs are lower compared to open-loop systems because are not expected ordinary operations on the probes, but only on the heat pump;
- The power produced is between 30 and 50 W per meter of drilled probe (VDI 4640/2, 2021), this value is dependent on the type of soil (grain size and composition of the clasts) with which the heat exchange takes place, but also according to the type of heat pump installed.

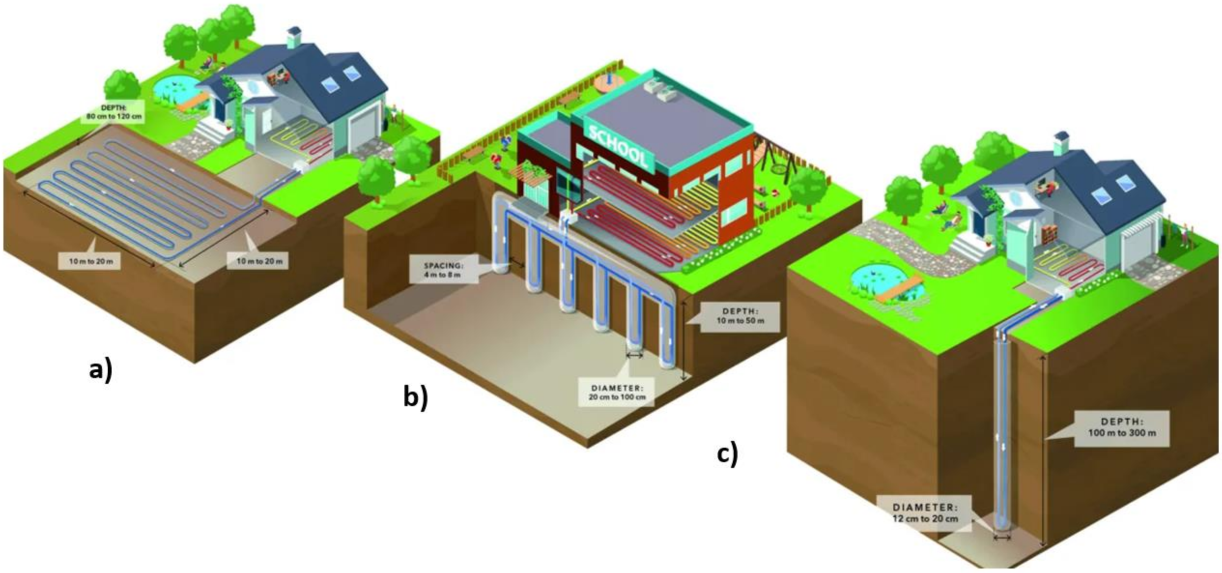

Figure 1.5 - a) Horizontal closed-loop system, b) geo-structure foundation of the building, c) vertical closed-loop system (from Capodaglio et al., 2018)

1.1.7 Different open-loop geothermal systems configurations

Open-loop systems exchange thermal energy with GW to heat/cool buildings. The configuration of the extraction and injection wells can be extremely variable, according mainly to the hydrogeological conditions of the location where the geothermal system is intended to be installed; one of the most important parameters to consider is the GW flow velocity (Bloemendal & Olsthoorn, 2018). The energetic potential of an aquifer, which defines the geothermic efficiency of a geothermal system, depends essentially on the grain size and geochemical composition of the clasts in the underground. Furthermore, by determining the aquifer thickness and by performing pumping tests, it is possible to assess its productivity, the hydraulic conductivity coefficient, the radius of influence and the induced drawdown in the well. By using these parameters, it is possible to assess if the depletion of the resource is taking place (in the case the pumping rate is too high), the maximum extraction rate and the possible hydraulic interference with another geothermal system.

Conventional open-loop systems

When the GW flow velocity is greater than 25 m/y conventional open-loop systems are the most popular (Bloemendal & Olsthoorn, 2018). Strong GW flow velocity conditions can be met in contexts where the grain size of the clasts that characterize the aquifer are composed mainly of sands or gravels (determining high values of hydraulic conductivity coefficient) and by a moderate gradient, which increases the GW flow velocity. The configuration of these systems is based on extracting the GW from an upstream well and injecting it back into a downstream well (**Figure 1.6**). To allow this process the wells are arranged longitudinally to the GW flow direction of the aquifer.

During the winter season, the GW is extracted from the upstream well at a constant temperature (the temperature of GW in the aquifer) entering the circuit to exchange the heat with the building, and is re-injected in the downstream well at a lower temperature. Conversely, during the summer season the GW is again extracted upstream, at a constant temperature, enters the circuit for cooling the building, and finally, is re-injected downstream at a greater temperature.

The sizing of these geothermal systems is strictly related to the storage volume, (amount of water extracted/injected during one season) to avoid hydraulic and thermal interaction between the two wells (Casasso & Sethi, 2017). If the two wells are located too close to each other, can occur that the upstream well extracts the hot/cold water injected by the downstream well. In these conditions is generated an induced gradient, because the water would be pulled from downstream in the upstream well, winning the natural gradient, letting the efficiency of the system drop dramatically (internal short-circuit flow).

One of the main disadvantages of conventional open-loop systems is the propagation of a polluting thermal plume downstream from the injection well, which could lead to enhancing the aquifer temperature, and consequently affect the efficiency of geothermal systems installed or to be installed (external short-circuit flow).

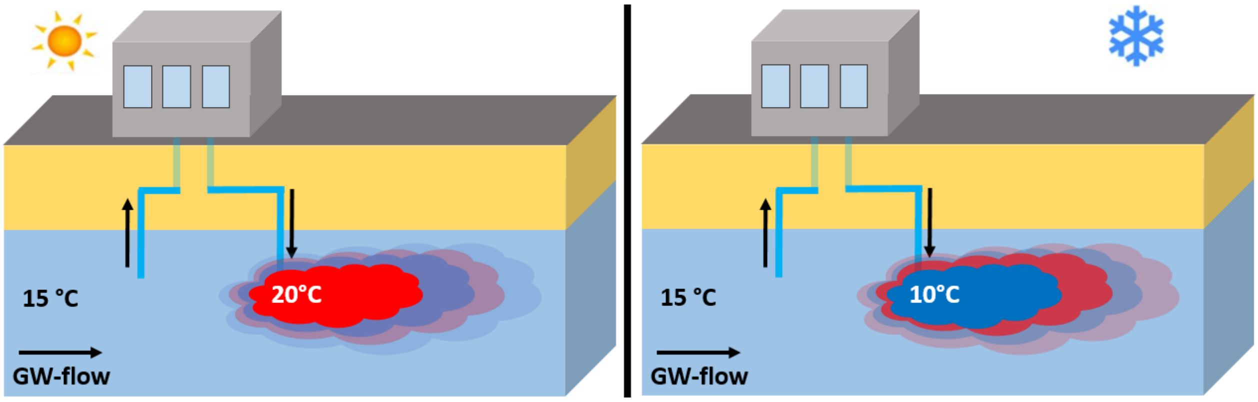

Figure 1.6 - Schematic representation of the operation, both in summer and in winter conditions, of a conventional open-loop system.

Traditional ATES

If the GW flow is less than 25 m/y the most acceptable configuration is traditional ATES (Aquifer Thermal Energy Storage) systems (Bloemendal et al., 2018; Rostampour et al., 2019; Bloemendal & Hartog, 2018; Pellegrini et al., 2019). ATES technology is known to reduce significantly CO_2 emissions for heating and cooling buildings (Fleuchaus et al., 2020). These types of systems are not limited to just extracting the thermal energy from the aquifer but also storing the energy in the aquifer to reuse it when needed (**Figure 1.7**). ATES systems are extremely popular in the Netherlands, but are installed also in Belgium, Germany, and North America, considering the usually low GW flow velocities. These systems consist of at least two wells, a “hot” well and a “cold” well. The “hot” one extracts the water during the winter season to heat the building, in the meanwhile the cold water is injected from the other well. During the summer season, the pumping scheme is reversed; consequently, the cold water injected in the previous season is extracted from the “cold” well to cool down the building, while the water at a higher temperature is re-injected from the “hot” well. These conditions are possible due to the almost or total steady state of the water in the aquiver, with greater GW flow velocities the energy stored in the aquifer would be dissipated downstream. The sizing of traditional ATES, as in the case of conventional open-loop systems, is related exclusively to the volume of water that needs to be stored in the aquifer to avoid hydrothermal interactions between the two wells. In case of low GW flow velocities, the best configuration is to arrange the wells transversally to the GW flow direction, otherwise in a longitudinal configuration would be more probable to observe internal short-circuit flow caused by the normal flow of the GW.

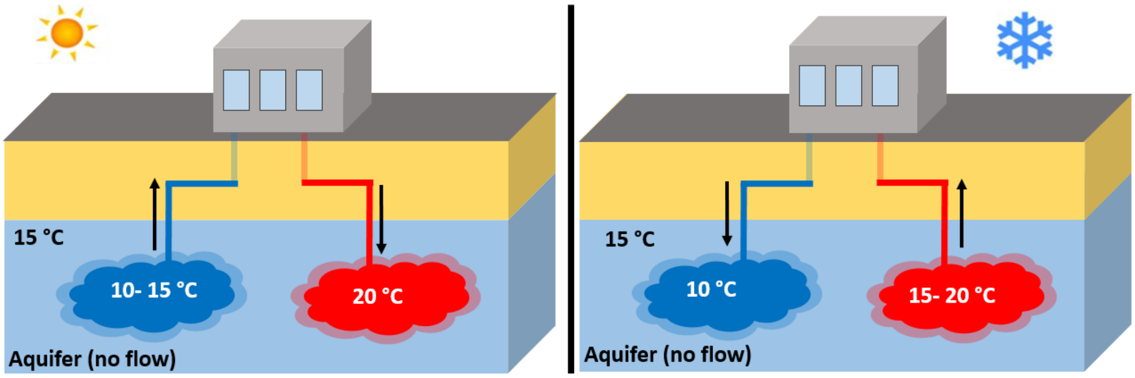

Figure 1.7 - Schematic representation of the operation, both in summer and in winter conditions, of a traditional ATES system.

Multiple Doublets

In high GW flow velocities scenarios, advection losses can significantly diminish the efficiency of ATES systems. This occurs when the injected thermal water is carried away by the natural GW flow before it can be fully recovered. To counteract these losses, multiple doublet systems (**Figure 1.8**) offer a promising solution (Stemmle et al., 2024). These systems involve multiple pairs of wells, strategically placed to optimize thermal energy storage and recovery. In cases of two-doublet systems, the wells are arranged parallel to the direction of GW flow and the heated or cooled water is injected into the upstream wells. In the subsequent season, the displaced thermal water is extracted from the downstream wells. Instead, a three-doublet system involves an upstream injection doublet, a downstream extraction doublet, and a middle doublet that operates alternately as an injection or extraction well, helping to increase the recovery of the stored thermal energy even more.

The spacing between doublets is a critical factor in determining the overall efficiency of the system. Iterative modelling and simulation can help identify the optimal spacing that maximizes thermal energy recovery while minimizing advection losses. However, these systems require at least two well doublets, and the specific placement distance might be difficult to achieve in an urban setting.

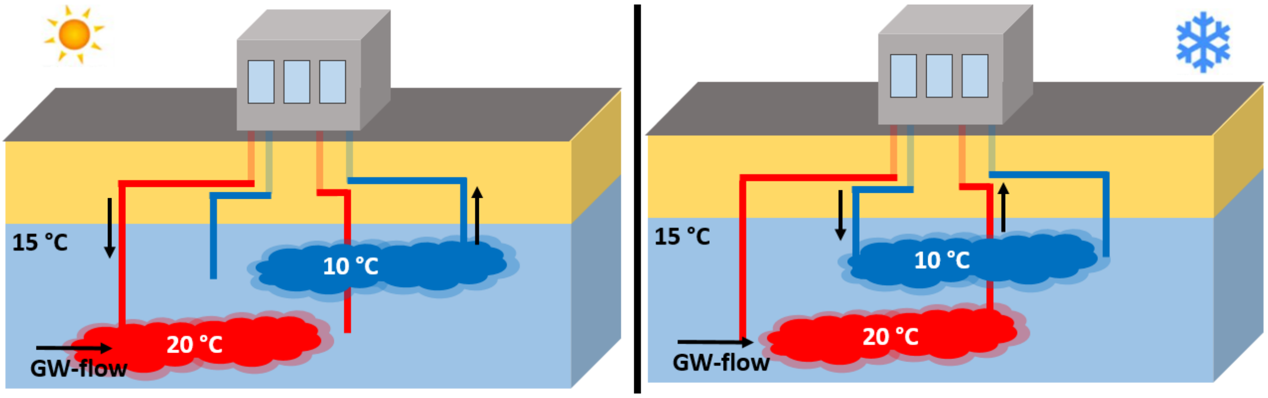

Figure 1.8 - Schematic representation of the operation, both in summer and in winter conditions, of a multiple doublet system.

Uni-directional ATES

In high GW flow velocities conditions, to overcome the problem related to the polluting thermal plume generated by conventional open-loop configurations, it is better to opt for a different configuration based on the combination of the two systems described above. This technique has not been developed as the other more traditional solutions, is being tested just on an experimental basis. It is named uni-directional ATES (**Figure 1.9**) and it is based on reversing the positions of the wells of a conventional open-loop system, allowing it to store the energy in the aquifer. In this case, the injection well is placed upstream, and the production (injection) well is placed downstream. Assuming that the system's operation starts in the winter season, the downstream well extracts the water at a natural temperature (GW temperature), which is used to heat the building and then be re-injected upstream at a lower temperature. Thus, during summer, the thermal plume produced by the injection well moves downstream due to the natural flow of the aquifer and is re-captured by the production well. By extracting the GW at a lower temperature the building is cooled down with greater efficiency, finally, the water is injected back into the aquifer at a greater temperature, ready to be recaptured in the following winter season.

The sizing of these types of systems is crucial to avoid negative thermal short-circuit flow effects, which could lead to a drop in efficiency. In this case, the inter-well distance is not simply dependent on the storage volume, as in the systems described previously, but is also related to the GW flow velocity. In the planning phase, if the GW flow velocity is not assessed correctly, the thermal plume could cross the production well before the beginning of the following season (if the GW flow velocity is greater than what was assessed), otherwise could reach the extraction well too late (if the GW flow velocity is lower that what was assessed). A deep understanding of the aquifer's hydrogeological properties of the areas where is intended to install these types of systems is fundamental. The best way to assess the GW flow velocity is by using heat tracer tests to obtain the real velocity, Lefranc or pumping tests result being imprecise because the GW flow velocity is retrieved indirectly.

Uni-directional ATES help mitigate the production of a polluting thermal plume downstream since most of it is being recaptured from the extraction well, in this way another geothermal system can be installed downstream at a shorter distance. Furthermore, if the inter-well distance is assessed correctly, it is also possible to enhance the efficiency of the system since in winter would be extracted water at a greater temperature, while in summer would be extracted at a lower temperature. Consequently, is needed less pumped water to achieve the same energy production compared to a conventional open-loop system.

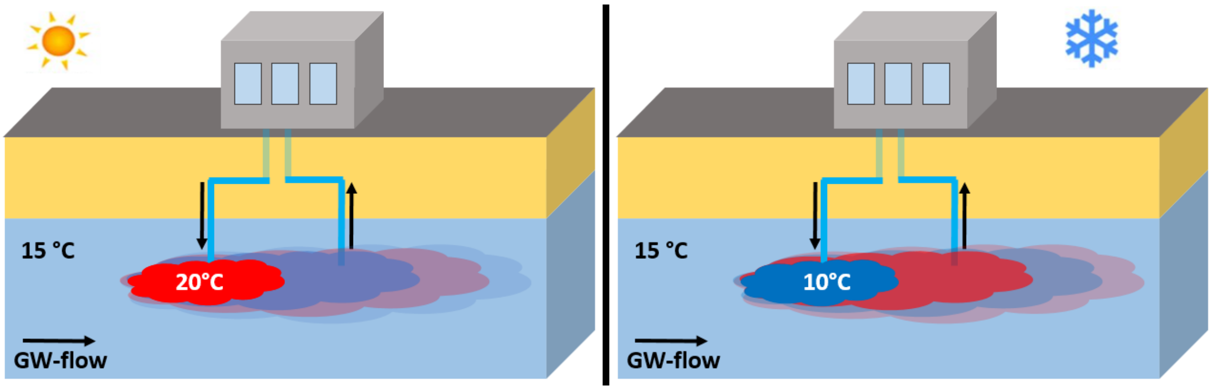

Figure 1.9 - Schematic representation of the operation, both in summer and in winter conditions, of a uni-directional ATES system.

1.2 Aims of the Thesis

The general aim of the project is to assess the potential energy and the feasibility of different geothermal system configurations to improve the management of GW at the metropolitan scale, also reducing the emission of CO_2 through the extraction of geothermal energy.

In particular the specific aims are:

- To compare different approaches for testing thermal conductivity in soils;
- To test different analytical formulae to obtain hydraulic parameters from boreholes logs data, in order to classify the geological units into hydrofacies;
- To evaluate the feasibility of different geothermal systems configurations, in order to assess the most efficient according to the geological conditions;
- To apply the results obtained from the theoretical approach to the real case study of Milan metropolitan area.

1.3 Thesis Outline

In order to reach the aims of the thesis the project has been divided into five milestones.

First will be analysed the geological and hydrogeological context of the Milan Metropolitan area, highlighting its critical significance within the Po Plain, a prominent sedimentary basin in Northern Italy. Subsequently will be presented, the interactions between groundwater and surface water, with particular attention to the influence of the region's hydrographic network, including rivers and canals, and the historical variations in groundwater levels over the past century. In addition, will be illustrated a comprehensive groundwater monitoring program initiated in 2016, which has provided valuable insights into the dynamics of the shallow aquifer. Utilizing advanced instrumentation, this program collects high-resolution data on groundwater levels and temperatures, capturing both seasonal and spatial variations in aquifer behaviour. The recent expansions of the monitoring network aim to enhance the quality and scope of data collection, supporting informed strategies for sustainable water resource management within the Milan Metropolitan area.

Another aspect investigated by this study was the thermal characterization of soils at different saturation levels, a key aspect of geothermal energy applications. It emphasizes thermal conductivity as a fundamental property for quantifying the extractable thermal energy from subsurface materials. The investigation begins with the characterization of soil samples collected from cores at a construction site in Milan. Two distinct instruments were employed for the thermal characterisation, to compare the methodologies and evaluate the consistency of the measurements. One is the Transient Line Source (TLS-100) needle probe, which is capable of measuring thermal conductivity in both intact and reconstructed soil samples. The other is the Heat Flow Meter (HFM) instrument, designed for solid materials. However, it was necessary to adapt this instrument for testing loose soils, which required the creation of a new methodology for its application.

Furthermore, this study conducted a comprehensive investigation into the hydrogeological characterisation of the subsurface environments. In particular, within the context of urban development and groundwater management in Milan and at the scale of the Po plane. This was possible thanks to collaborative efforts between the University of Bicocca and Milan's Metropolitan company, which provided geotechnical and borehole data collected during the tube lines construction and the building projects. Data acquisition involved digitizing 165 borehole logs, spanning 1485 geological horizons, and performing grain size distribution analyses. MATLAB tools interpolated these data to classify horizons into 26 hydrofacies categories, based on a combination of A.G.I. soil classification standards and empirical formulas for hydraulic conductivity (e.g., Hazen, Kozeny, Chapuis).

The application of numerical models enabled a comparative analysis of non-conventional geothermal systems with those installed in northern Italy, with a particular focus on the metropolitan city of Milan. This section will focus on the generation of 3D finite-difference models using MODFLOW's MT3DMS code to simulate groundwater flow and thermal transport. The sensitivity analysis was performed by evaluating the effects of key parameters variations, including inter-well distance, groundwater flow velocity and storage volume. By varying these parameters, the model highlights how the system design can affect its efficiency. The configurations of geothermal systems that were considered in this study focused on conventional open-loop systems, traditional and uni-directional ATES systems. In addition, the aquifer thickness, dispersivity, and energy imbalances were evaluated. Also addressing, operational risks, cost implications, and regulatory considerations.

As a final step, an existing geothermal system database will be incorporated into a regional-scale modelling with the objective of enhancing the efficiency and sustainability of geothermal plants in the Metropolitan City of Milan. Were digitalized 1,069 permits for geothermal installations, creating a geodatabase with key technical and operational parameters. The data was standardized and verified to correct errors, enabling the assessment of potential efficiency gains from converting conventional open-loop systems into traditional or uni-directional ATES systems. Statistical analyses were conducted on the dataset, revealing patterns in geothermal system distribution, energy production, and well configurations. Spatial and temporal trends were visualized through maps and bar plots.

The feasibility of system conversion was evaluated by examining seasonal energy imbalances and groundwater flow velocities in existing geothermal systems in Milan’s municipality.

2. Study Area

The Milan Metropolitan area is situated within the Po Plain, a major sedimentary basin in Northern Italy that spans approximately 1,600 Km^2, with a population of about 3.2 million people (ISTAT, 2023). In this area lies also the Municipality of Milan having a surface of 182 km^2 and a population close to 1.35 million inhabitants (ISTAT, 2023). This plain represents one of the most significant geological features in Europe (Burrato et al., 2003), formed through complex interactions between tectonic activity, climatic changes, and sedimentation processes. Its geological evolution has been shaped over millions of years, with contributions from the uplift of the Alps, glaciation events, and river systems that have deposited vast amounts of sediment across the basin.

2.1 Geological background and setting

The tectonic origins of the Po Plain developed as a foreland basin during the Pliocene (around 5.3 to 2.6 million years ago) in response to the collision between the African and Eurasian tectonic plates, which led to the uplift of the Alps. This tectonic activity created a depression in the earth's crust that formed a sedimentary basin in front of the advancing Alpine orogeny. During the Pliocene, this basin was characterized by deep marine conditions, leading to the accumulation of fine-grained marine sediments such as clays and silts. These early marine deposits form the lowermost layers of the basin serve as a base for the overlying continental deposits.

As the climate cooled and the Alps continued to rise, the Po Basin transitioned from a marine to a continental environment during the Pleistocene epoch (around 2.6 million to 11,700 years ago). The advance of glaciers from the Alps during this period significantly influenced sedimentation patterns in the region. The Pleistocene in this region was marked by a series of glaciation cycles, during which glaciers extended from the Alps to the Po Basin (Muttoni et al., 2003; Garzanti et al., 2011). These glaciations brought large amounts of sediments (ranging from gravels to sands) deposited in the basin as the glaciers advanced and retreated. The glacial outwash plains formed extensive alluvial fans along the mountain-front, creating a landscape of braided river systems that transported sediments further south into the basin.

This process led to the formation of large alluvial fans at the base of the Alpine foothills. These fans coalesced into a continuous apron of sediments that spread across the northern part of the Po Plain. The thick gravelly deposits formed the foundation of what would become the unconfined aquifers of the region. As the glaciers melted and receded during interglacial periods, rivers transported finer sediments like sands, silts, and clays into the central and southern parts of the basin. This process created a layered structure, with coarser gravel deposits near the Alps transitioning to finer sediments further south. The repeated cycles of glacial advance and retreat established a stratigraphy that consists of stacked layers of sands, gravels, silts, and clays, forming a multi-aquifer system with varying permeability and storage capacity.

2.2 Ground and surface water system dynamics

The study area is situated within the Po Plain, delimited north by the peripheral foreland basin of the Alps, west and east by the Tyrrhenian and Adriatic seas respectively, and south by the Apennines. Three primary depositional sequences characterise the Po Plain, each corresponding to distinct aquifer systems (Regione Lombardia & Eni, 2002; Martinis & Mazzarella, 1971):

1. Unconfined Aquifer (Group A): This uppermost unit comprises predominantly gravelly materials with a sandy matrix. The thickness of this layer varies between 20 and 100 meters, with a more consistent clayey-silty aquitard towards the southern parts of the area, which diminishes northwards.
2. Semi-Confined Aquifer (Group B): Overlying the deep aquifer, this system includes sands and sandy gravels, with thicknesses ranging from 50 to 150 meters. It reflects the glacial outwash plains formed during the major Pleistocene glaciations. This aquifer is bounded by clay-rich layers at its base.
3. Deep Confined Aquifer (Group C): This aquifer comprises sandy lenses interbedded with clays and silts, representing the lower Pliocene deposits. These layers originate from meandering river systems that transported sediments from the Alps, forming a complex structure of sandy and silty layers.

The hydrogeological structure is defined by the interaction of these aquifers and aquicludes, influencing groundwater (GW) flow patterns. In particular, the semi-confined and unconfined aquifers are crucial for regional water dynamics, providing significant storage and flow capacity. The hydraulic properties of these aquifers, including conductivity and transmissivity, were determined through well tests and empirical methods, revealing a conductivity gradient from the coarse deposits in the north to finer sediments in the south.

Recent studies and hydrostratigraphic models of the area emphasize the role of the aquifer geometry in managing water resources. These models integrate geological data, including borehole logs, seismic surveys, and stratigraphic analyses, to delineate aquifer boundaries and estimate hydraulic parameters.

The study area features a complex hydrographic network (**Figure 2.1**) comprising rivers, minor streams, and artificial irrigation canals. The primary rivers are the Ticino (350 m^3/s) and the Adda (190 m^3/s), which originate from Lake Maggiore and Lake Como, respectively, and flow into the Po River (1,550 m^3/s). The Ticino and Adda have carved valleys 5 to 80 meters below the surrounding ground level due to head-ward erosion, making them predominantly gaining rivers (water level below or near the GW level), as they are closely connected to the GW (Previati, 2022).

Other rivers in the region, such as the Lambro, Olona, Seveso, and Lura, originate in the alpine foothills and converge in the Milan metropolitan area. Here, some are partially culverted, except for the Lambro River. These rivers have relatively shallow riverbeds, lying 1 to 5 meters below the local ground elevation. Their interaction with GW varies: in the northern area, they are losing rivers (the river water level is above the GW level), while in the southern area, they transition to gaining conditions, depending on the water table elevation (Castiglioni et al., 2015; Gambini et al., 2024).

Milan’s canal network, known as the “Navigli” system, was developed starting in the 12th century to facilitate commercial and irrigation activities. This system connects Milan to the nearby Adda and Ticino Rivers. The Naviglio Grande flows from the Ticino to Milan and feeds into the Naviglio Pavese, which extends from Milan to Pavia. The Naviglio Martesana runs from the Adda to Milan, connecting the eastern metropolitan area to the city centre, and supplying numerous secondary irrigation canals. The flow within the Navigli is periodically regulated for maintenance, allowing partial or complete reduction of flow. To the north, the Villoresi irrigation canal, originating from the Ticino River, extends to the Adda River, supporting a gravity-driven network of secondary and tertiary canals spanning approximately 3,000 km (De Caro, 2018).

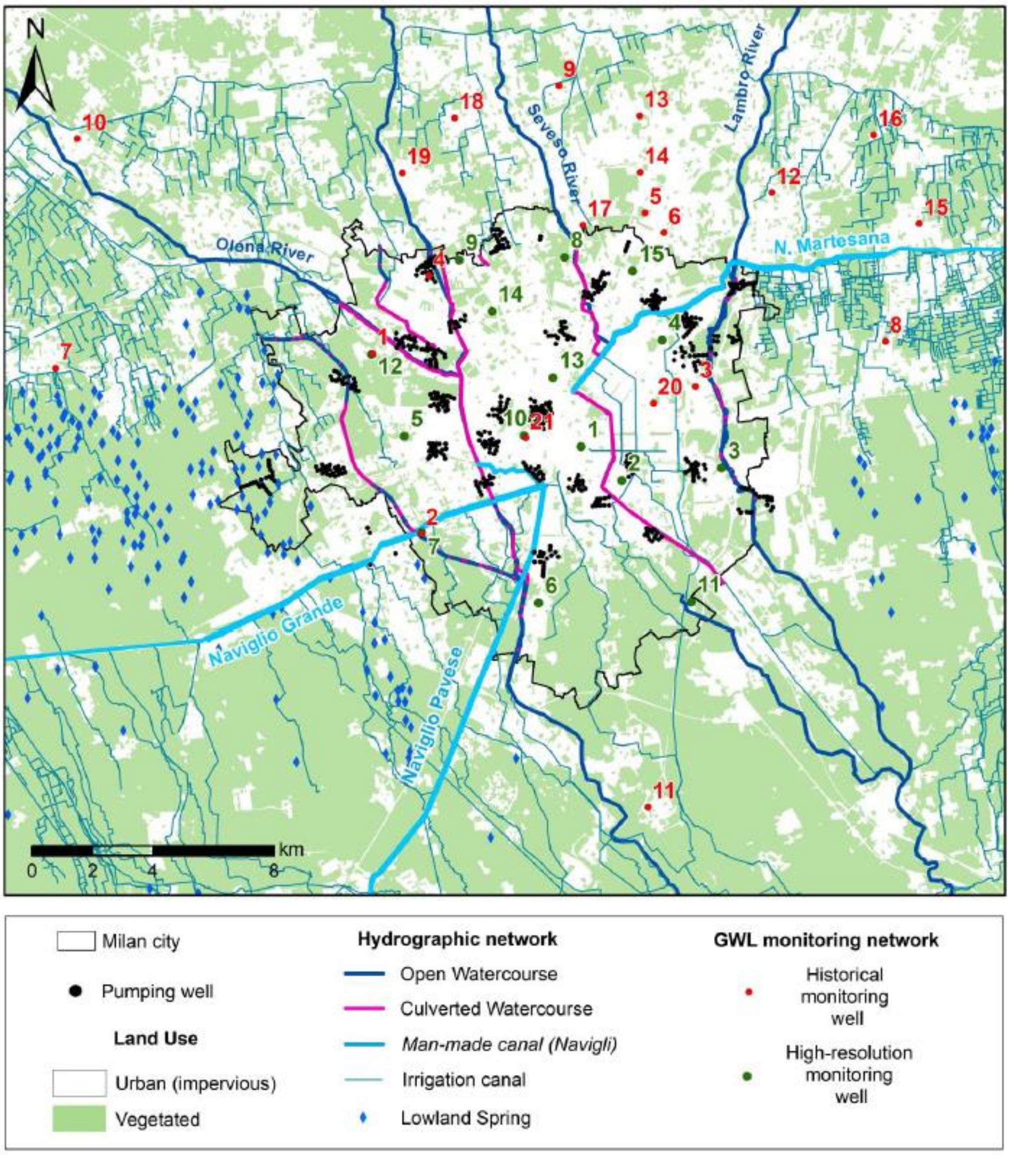

Figure 2.1 - Map of the Milan metropolitan area illustrating the hydrographic network (i.e. rivers, lowland springs, the Navigli canal system, and irrigation canals) alongside the spatial distribution of groundwater monitoring wells. High-resolution monitoring wells. High-resolution monitoring wells are marked with green dots, while historical monitoring wells are indicated by red dots.

The GW dynamics in the Milan area illustrate a close relationship between socio-economic events and GW management practices (**Figure 2.2**). Here will be described the main trends of the last century's water level.

The economic boom started in the middle of the past century, the post-Second World War industrial growth spurred increased water demand, leading to extensive GW pumping. This period saw the highest abstraction rates, peaking at approximately 700 million m^3 per year.

This resulted in significant GW level declines in the unconfined aquifer, with water tables dropping by 10–15 meters.

From 1975, with the oil crisis, the economic challenges reduced industrial activity, which directly affected water demand, leading to a quick reduction in pumping rates. GW levels rebounded by 7 - 8 meters as a result of the reduced abstraction.

Until 1985 was registered as a stationary period, in which the area experienced a stabilization both in pumping and GW levels.

At the beginning of the ‘90s, a second wave of economic downturns, due to the European monetary system crisis, led to a reduction in water use, resulting in a gradual GW level rise.

More recently, the abstraction rates declined to 220 million m^3 per year in the 2010s, resulting in a rapid recovery of the shallow aquifer’s GW level, and raised up to 1 meter per year in the period 2008 – 2014.

The spatial variation of water oscillations in the Milan Metropolitan area was not homogenous. In the northern parts of the city, the largest fluctuations were observed (up to 5 – 10 meters) since in this area the GW responded dynamically to changes in abstraction rates. On the contrary, in the southern parts of the city, the GW level showed limited variations, generally below 4 meters. Here, the hydrographic network (rivers and canals) likely exerts a strong influence, keeping water levels shallow and stable due to natural recharge and interaction with surface water.

This section explains the strong consistency between Milan’s socio-economic changes, particularly industrial demand and economic crises, and the management of GW resources. As GW demand decreased with changing economic conditions, GW levels have shown substantial recovery, especially in urbanized and industrial zones, while remaining relatively stable in areas with significant agricultural or hydrographic influences.

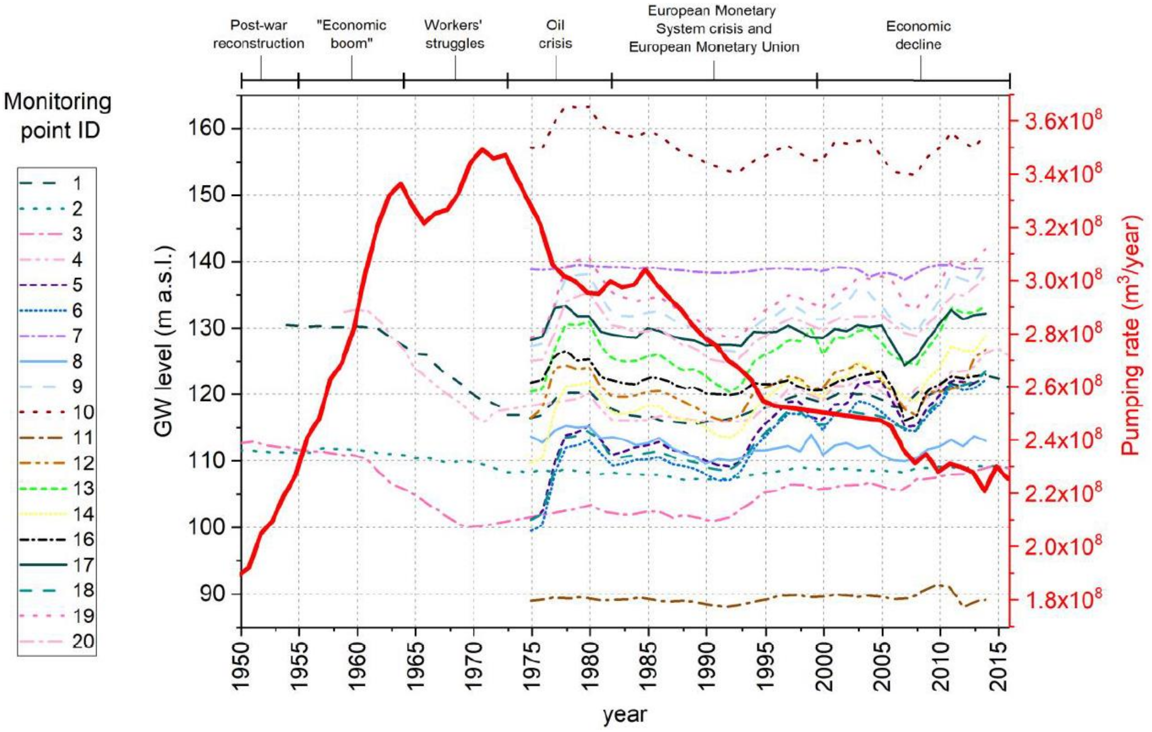

Figure 2.2 - Historical monitoring data (1950–2016) showing groundwater levels for the unconfined aquifer (red dots, as indicated in Figure 2.1) alongside the total groundwater abstraction rate (red line) for wells located within the Milan area (black dots, as shown in Figure 2.1) (From De Caro et al, 2017).

2.3 Shallow aquifer monitoring

During this project the GW monitoring of the shallow aquifer was carried out by the University of Milan Bicocca research group, following up an activity that has been ongoing already since 2016, when 22 open-pipe piezometers were equipped with automatic sensors. This activity was possible thanks to the collaboration started in 2016 between Bicocca University and MM (Metropolitans of Milan) which is the owner of the piezometers. The main parameters collected are GW level and temperature, with a temporal resolution of three months (four campaigns per year). These data were acquired by using three different instruments (**Figure 2.3**); a pressure transducer *(Diver®, VanEssen Instruments)*, which is inserted in the piezometer hanging to a metallic cable for the whole monitoring period, located around three meters below the water table. This instrument was used to collect information on GW temperature (± 0.1 °C) and pressure (± 0.1 cmH_2O) with an automatic acquisition every 15 minutes. A multi-parameter probe *(Aqua troll 500)* was used to perform manual measures of the temperature profile of the monitored piezometers (the instrument records simultaneously also pH, electric conductivity and dissolved oxygen); the probe is dropped at the bottom of the piezometer and pulled back to collect a measure every meter along the whole water column. Finally, was also used a phreatimeter to collect manual measures of the water table level in every piezometer for each monitoring campaign. The Diver collects a pressure measurement while is immersed in water and for this reason, the data acquired need to be compensated using the barometric pressure, by subtracting the atmospheric pressure from the water pressure. Once the manual measure of the water level is collected using the phreatimeter, the water level variation is known due to its pressure changes.

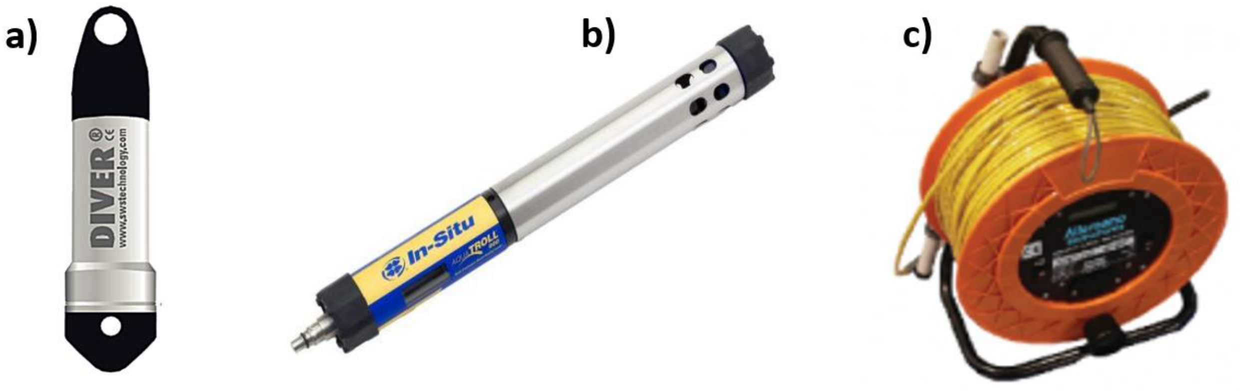

Figure 2.3 - a) Pressure transducer (Diver®, VanEssen Instruments), b) multi-parameter probe (Aqua troll 500), and c) phreatimeter.

The number of monitored piezometers during the years changed several times, according to problems detected in specific piezometers or related to instrument failures (**Figure 2.4**). Recently, the monitoring network was extended to obtain more consistent data, but the outcomes of this extension will be evaluated in the next years.

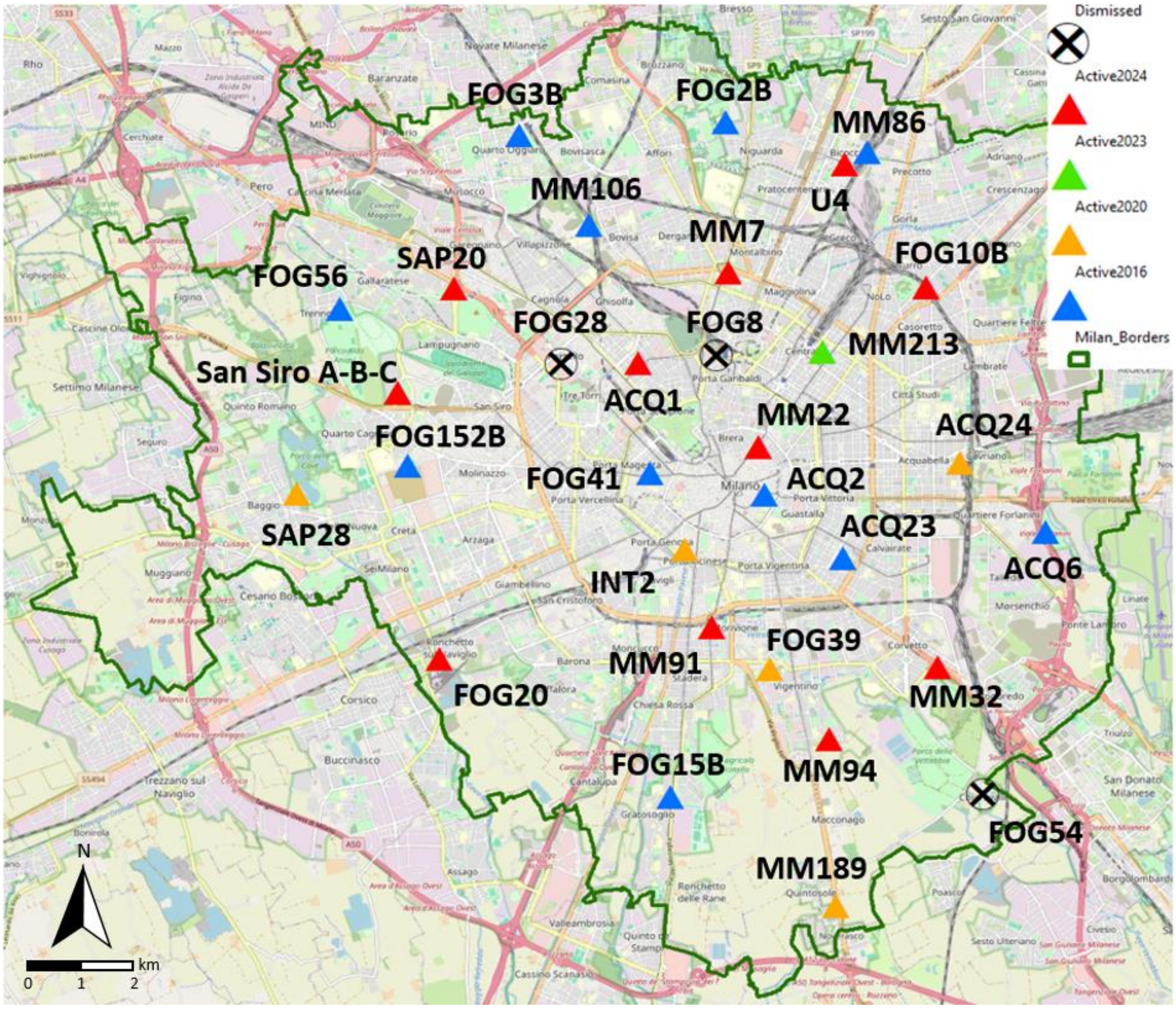

Figure 2.4 - Map showing the location of the monitored piezometers in the Milan Municipality. The blue triangles represent the piezometers monitored since 2016, in orange since 2020, in green since 2023, in red since 2024, and the black cross represents the dismissed piezometers.

Figure 2.5 illustrates the variation in piezometric levels recorded by the piezometers throughout the monitoring campaign. The log of the data spans from the beginning of the monitoring period until the most recent campaign. Over the past two years, the hydrological impact of extreme climatic events is observable. The severe drought that persisted throughout 2023 is appreciable, as is the substantial recharge driven by the frequent precipitation events of 2024. These trends are most pronounced in areas where the piezometric level is below 10 meters.

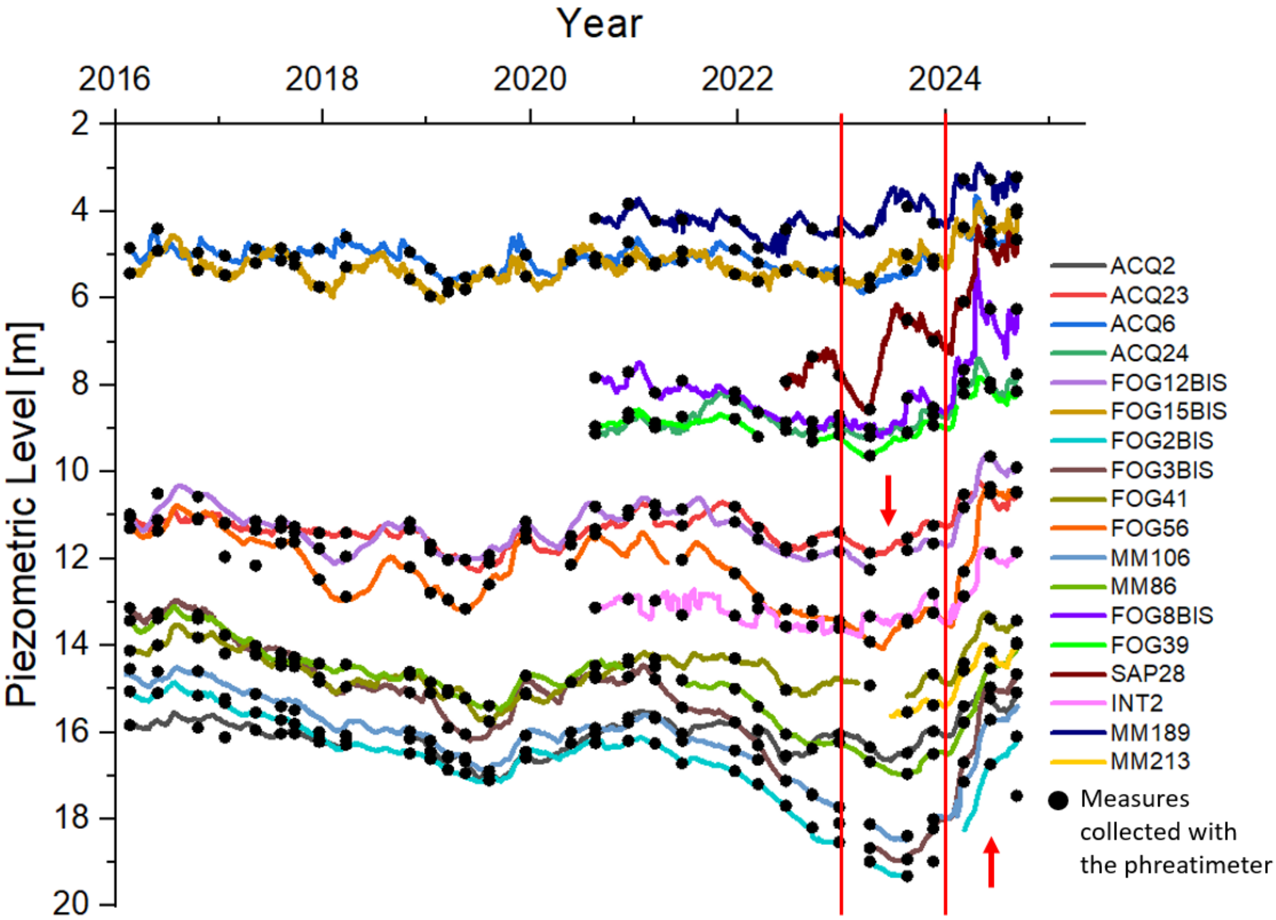

Figure 2.5 - Piezometric level variations recorded by the monitored piezometers from 2016 to the most recent campaign. The black dots indicate measurements obtained using the phreatimeter, employed to verify the consistency of the data collected by the pressure transducer sensors. The arrows indicate the trend exhibited by the aquifer over a specific time spans.

The data collected during the last campaign (October 2024) were interpolated using the water head, which takes into account the absolute elevation of each measurement, as shown in **Figure 2.6**. The resulting interpolated raster does not cover the entire surface of Milan's municipality in order to avoid the uncertainties associated with extrapolation.

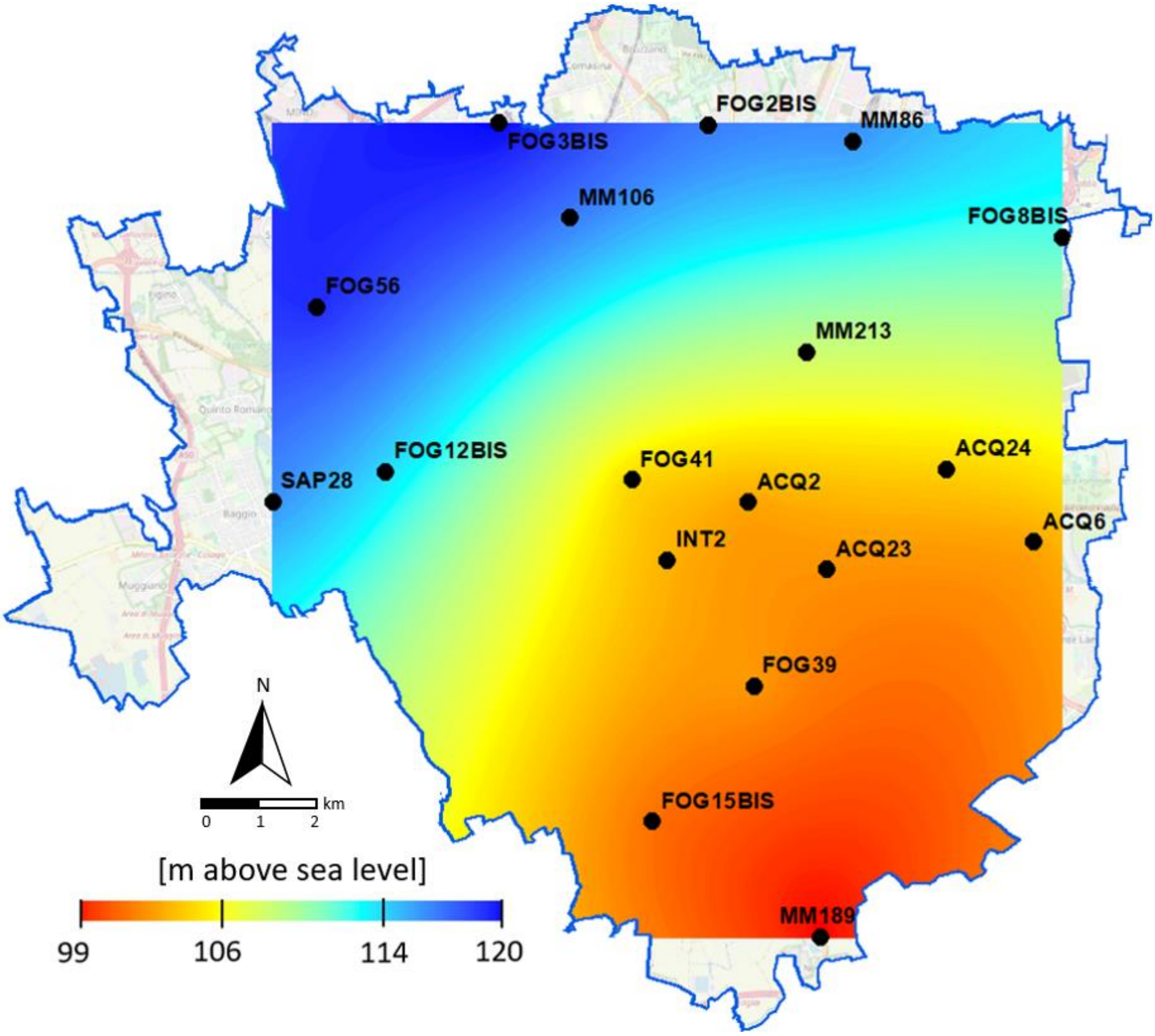

Figure 2.6 – Map displaying the interpolated water head derived from the measurements collected from the considered piezometers during the most recent campaign (October 2024). In order to minimize uncertainties associated with the extrapolation, the raster does not cover the entire extent of the municipality of Milan.

In **Figure 2.7** are shown the temperature variation with depth across all the conducted monitoring campaign, for all the active piezometers.

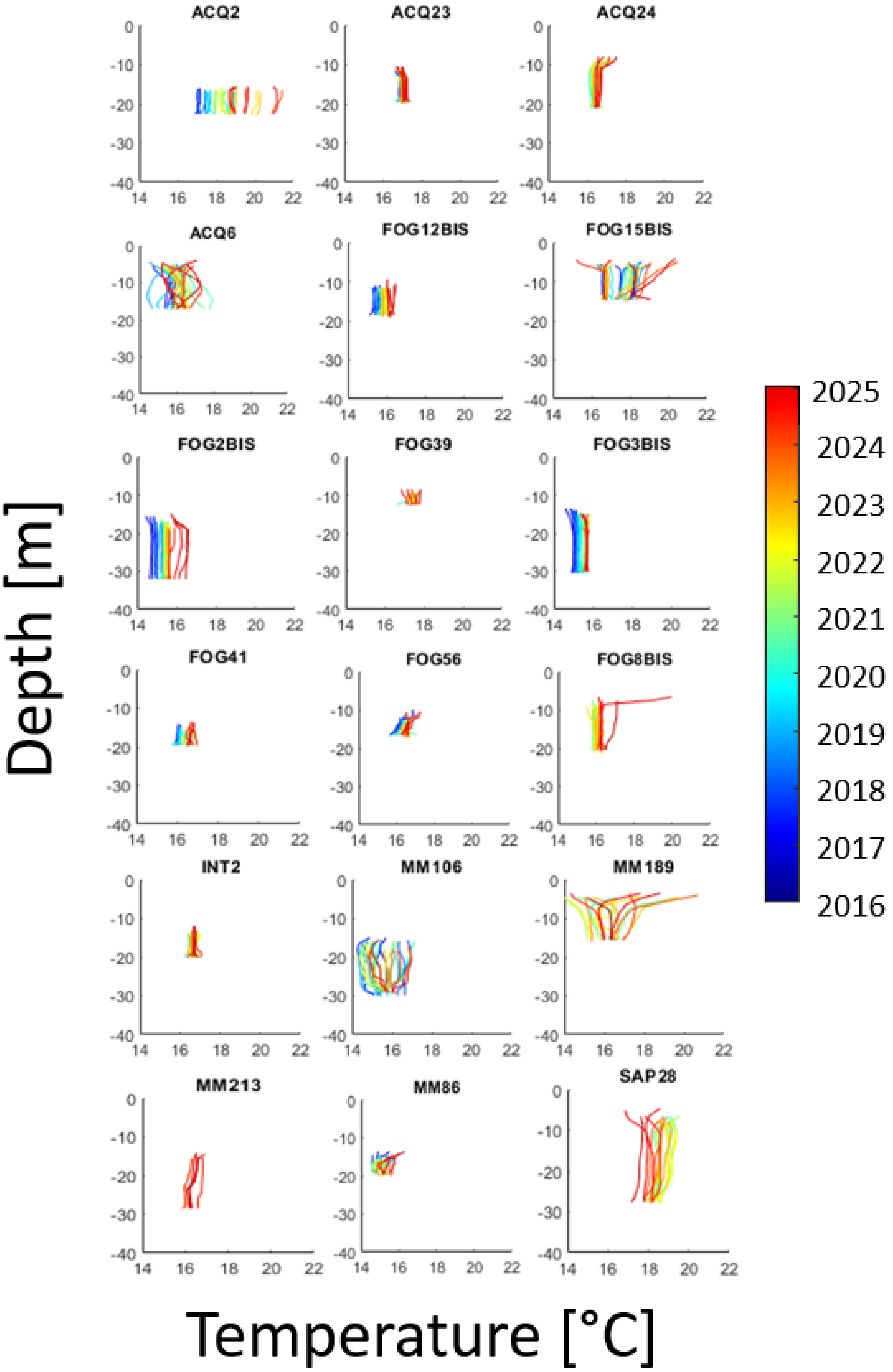

Figure 2.7 - Temperature variation with depth throughout the entire monitoring campaign for all the piezometers considered.

3. Thermal characterization of soils

Thermal conductivity represents a fundamental parameter in quantifying the potential thermal energy extractable from the subsurface environment or groundwater (GW) for geothermal applications. The assessment of thermal conductivity is conducted using a range of specialized instruments and methodologies, encompassing both in situ and laboratory-based testing approaches, to evaluate the thermal properties of specific soil horizons.

3.1 Introduction to the methodology

This study aimed to identify an effective methodology for testing loose materials’ thermal conductivity in laboratory using a steady-state heat flow instrument, the Heat Flow Meter (HFM) by ThermTest, which is specifically designed for solid blocks. Additionally, the robustness of the results was enhanced by comparing them with measurements obtained from a transient heat flow instrument, in our case was opted for the Transient Line Source (TLS-100 Portable Meter) also by ThermTest. A similar approach was employed by Barry-Macaulay et al. (2013); however, their study did not include testing loose materials with a steady-state instrument. To address this limitation, the methodology proposed by Alrtimi et al. (2016) was also considered, as it involved testing the thermal conductivity of loose materials with a steady-state instrument. Even though, their approach did not incorporate a comparison with results obtained from a transient heat flow instrument.

3.2 Sample characterisation

In December 2021, as part of the infrastructural works associated with the extension of the tube lines at the Cadorna site in Milan, a series of cores were drilled. One of these cores, covering the stratigraphic horizons from 0 to 30 meters below the surface, was subsequently subjected to detailed analysis (**Figure 3.1**). The initial phase of this investigation involved examining specific sections of the core using the grain size distribution (GSD) technique to assess the heterogeneity of the retrieved material.

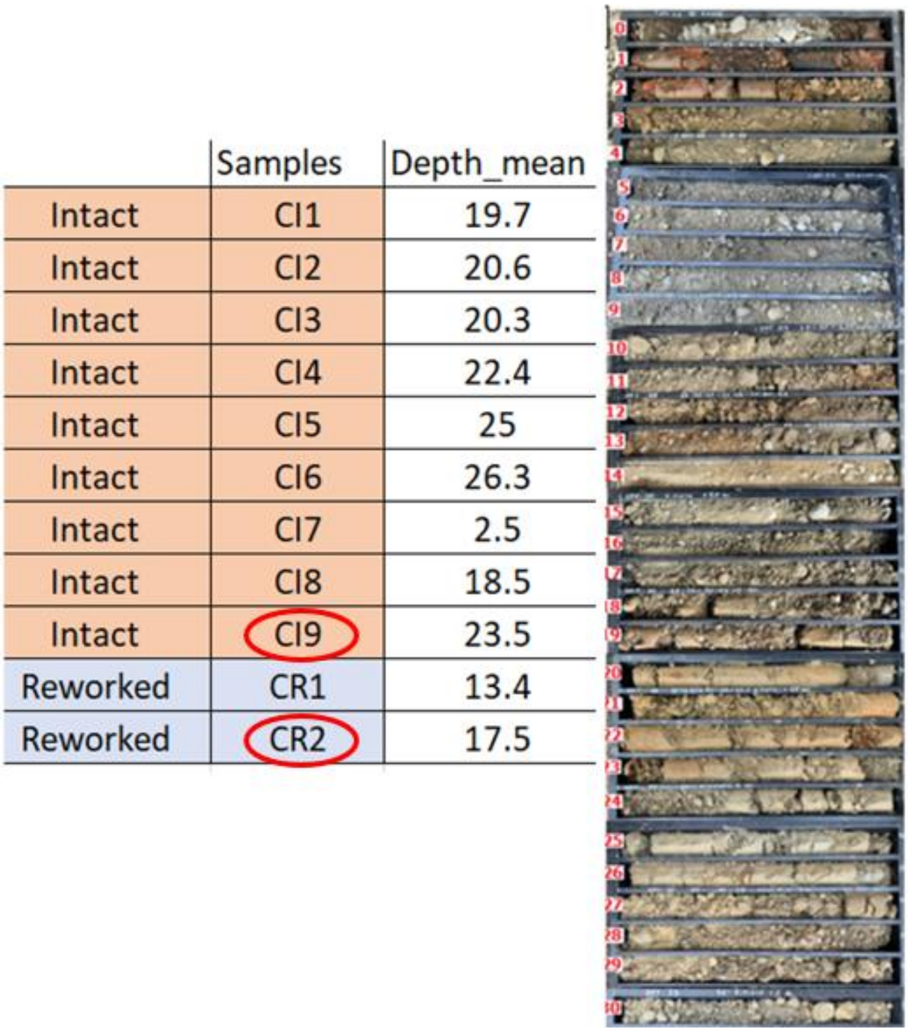

	Samples	Depth_mean
Intact	CI1	19.7
Intact	CI2	20.6
Intact	CI3	20.3
Intact	CI4	22.4
Intact	CI5	25
Intact	CI6	26.3
Intact	CI7	2.5
Intact	CI8	18.5
Intact	CI9	23.5
Reworked	CR1	13.4
Reworked	CR2	17.5

Figure 3.1 - The left image presents the sample names alongside their respective depths, indicating the points at which they were extracted from the core. On the right is shown a generalized representation of the lithologies encountered during the drilling process. The two red circles highlight the samples selected for further investigation of the loose material.

3.3 Needle probe instrument

One of the most widely employed instruments for assessing the thermal conductivity of materials is the TLS-100 Portable Meter (**Figure 3.2**) (ASTM, 2022). This device operates by generating a linear heat source and utilizing thermistors to measure temperature variations (Low et al., 2014; Bristow et al., 2001). The apparatus is a portable thermal meter, consisting of a data logger connected to a needle probe via a wire. Before commencing the test, the needle probe is coated with thermal paste to enhance coupling between the probe and the sample, thereby ensuring more accurate conduction of the thermal signal.

The instrument works by applying transient heat and conducts the test in two distinct phases. In the first phase, the needle probe emits a thermal signal that propagates through the sample. In the second phase, the thermal signal ceases, enabling the logger to measure the time required for the sample to heat up, in the first phase, and subsequently cool down, in the second one. This process facilitates the determination of thermal conductivity and resistivity. The instrument is versatile, allowing tests to be conducted in situ, on cores or reworked samples.

Figure 3.2 - ThermTest's TLS-100 needle probe. On the right are depicted the two probe configurations utilised during its operation.

3.3.1 Needle probe test method

Initially, thermal conductivity tests were performed on the least disturbed sections of the cores, selected at representative intervals. Measurements were taken by inserting the probe into the intact portions of the core in both axial and transverse orientations, where possible. However, the presence of coarse material within the core occasionally obstructed the insertion of the testing probe (**Figure 3.3**).

Figure 3.3 - ThermTest's TLS-100 needle probe while operating a measurement on an intact sample.

Additionally, the core sections considered representative were weighed to calculate the material's density, thus determining the core's volume based on its radius. After drying the core portions in an oven at 60°C for 48 hours, a second weighing (w_s) was performed to calculate the water content at the time of the test. It is important to note that this measurement does not reflect the in situ water content, as the core had been stored in the laboratory for over a month, resulting in a moisture content lower than its initial value.

The dried samples were then used as remoulded specimens, with the dried cores being broken to obtain loose sand, silt, and gravel. The maximum and minimum void index (e_{max} and e_{min}) were determined during sample preparation using the vibrating table method (Kaufman et al., 1979; ASTM, 2006).

The loose material was subsequently dispersed into a mould with the assistance of a funnel. This procedure allowed for the attainment of the lowest possible density value of the sample (ρ_s, density of the solid) (Eq. 3.1), while simultaneously achieving the highest possible porosity, thereby obtaining the e_{max}. Once the volume occupied by the loose material (V_s) was defined, its ρ_s was calculated using the following formula:

$$\rho_S = \frac{W_S}{V_S} \qquad \text{(Eq. 3.1)}$$

Thermal conductivity analyses were performed by inserting the needle probe into the sample within the mould. Additionally, thermal tests were conducted at five distinct saturation levels (0%, 25%, 50%, 75%, and 100%). Water was incrementally added from the top of the mould, with the quantity estimated based on the void volume of the sample (V_v).

Subsequently, the vibrating table was activated for 12 minutes at a frequency of 50 Hz, with a weight at the top and a vertical amplitude of 0.4 mm. As the machine was activated, the loose material gradually compacted within the mould until it reached the minimum void index (e_{min}) and its maximum density (**Figure 3.4**). The thermal conductivity was then measured using the same method outlined in the previous step, with tests conducted at the five different saturation levels.

Figure 3.4 – ThermTest's TLS-100 needle probe while operating a measurement on a remoulded sample in e_{min} *conditions.*

The application of this technique revealed that the thermal conductivity remained largely consistent across the various saturation levels. This phenomenon may be attributed to the fact that the water was poured from above into the mould, preventing its homogeneous distribution and drainage throughout the entire sample. The application of this technique revealed that the thermal conductivity remained largely consistent across the different saturation levels. This observation may be attributed to the method of water addition, where the water was poured from above into the mould, which prevented its homogeneous distribution and drainage throughout the entire sample. As a result, the needle probe measured the oversaturated portion of the sample, rather than providing a representative average value. To address this issue, the sample was subsequently dried and then placed into a tray in which was added a specific volume of water, sufficient to achieve the required saturation level. By combining the two components, a homogeneous saturated sample was obtained, allowing the test to be repeated once more.

Following this, the thermal conductivity was assessed under even more controlled conditions on the reconstructed samples. The material was sieved to a particle size of 2.63 mm, thereby isolating the fine fraction for analysis. **Figure 3.5** illustrates the use of smaller plastic cylindrical containers as moulds. Each mould underwent a distinct saturation process (ranging from 0% to 100% with 10% increments) and contained an identical weight of material. The samples were moderately compacted to ensure they occupied the same volume within each mould, thereby achieving uniform density and medium void index (e_{med}).

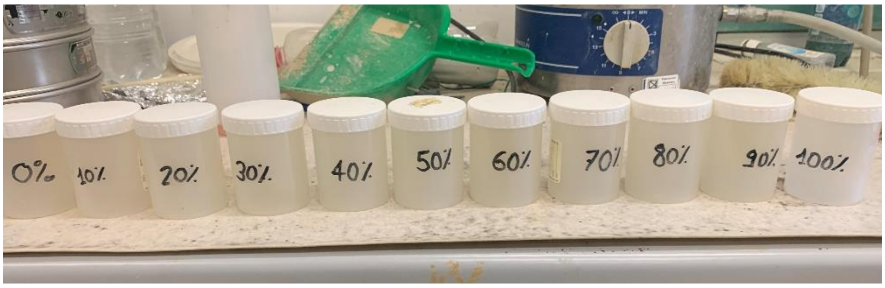

Figure 3.5 - Containers selected as a mould for operating the tests in more controlled conditions. Each container was assigned to a specific saturation level.

3.3.2 Needle probe test results

As detailed in the sample preparation section, the initial tests were conducted on the intact portions of the cores. **Figure 3.6a** shows that no tests were performed between 3 and 18 meters in depth, as no intact core portions were available. A notable correlation was observed between thermal conductivity and grain size percentage. At approximately 20 meters depth, an increment in thermal conductivity was recorded, with a positive correlation evident between the percentage of sand, as illustrated in **Figure 3.6b**. This phenomenon can be attributed to the significant prevalence of quartz in the sand, which is known to enhance the bulk thermal conductivity (Clauser & Huenges, 1995). It should be noted that the intact portions of the core did not reflect the in situ saturation level, as the core had been stored in university buildings for a period of three months prior to the commencement of testing.

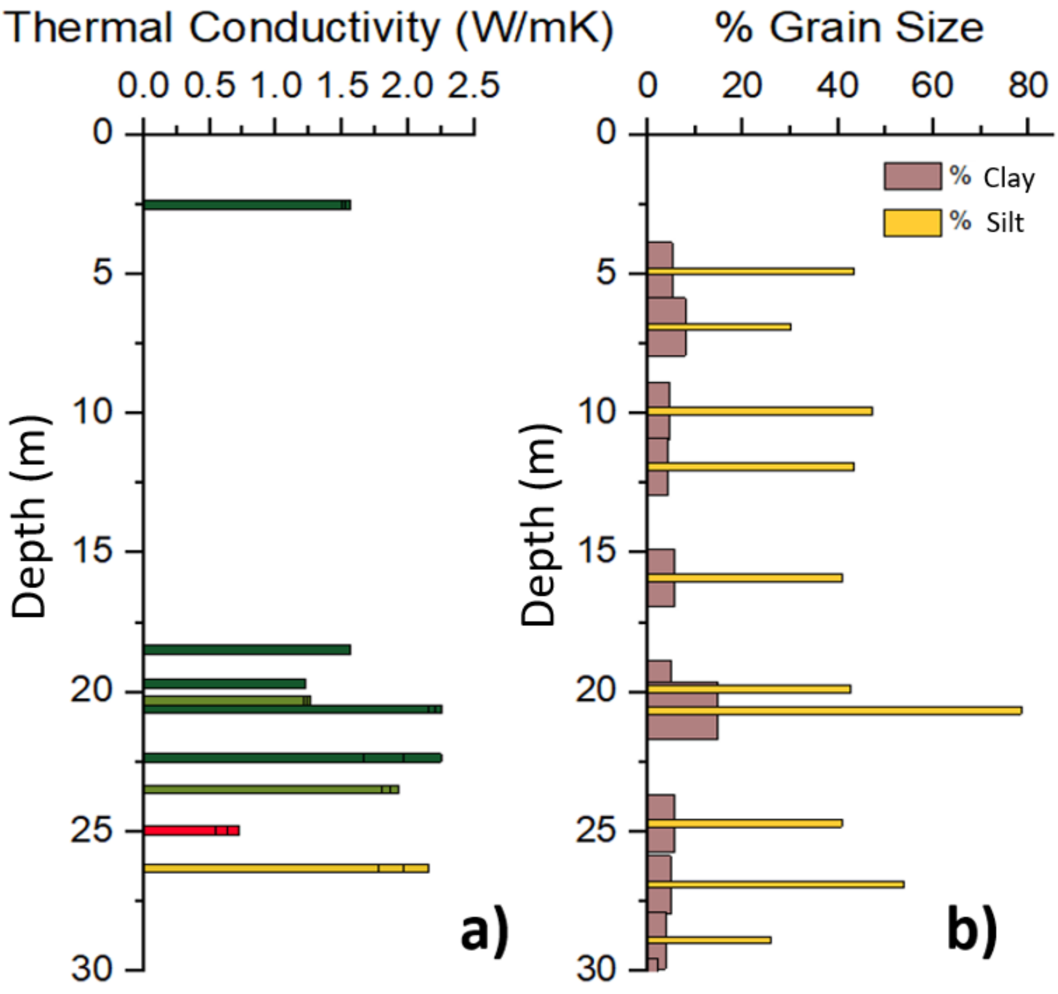

Figure 3.6 - a) Thermal conductivity values for the intact samples tested at specific depths. b) Grain size distribution (GSD) of the selected samples at representative depth, in which are shown the abundance of clay and silt.

Before conducting the thermal conductivity tests, the reworked samples were subjected to oven drying. These analyses were performed on a representative specimen, CR2. As previously described, the loose material was prepared in the mould to assess the maximum void index (e_{max}) at various saturation levels. This was achieved by gradually increasing the volume of water poured into the top of the mould. The same procedure was used to evaluate the thermal conductivity at the minimum void index (e_{min}).

Figure 3.7 illustrates the thermal conductivity values under e_{max} and e_{min} conditions, both of which exhibit a rapid increase, particularly during the initial saturation phase (25%). As the saturation level rises, the thermal conductivity continues to increase gradually, reaching its maximum value at 100% saturation. The two conditions represented by the coloured lines are compared with the arithmetic, geometric, and harmonic averages (indicated by the dashed lines), for both e_{max} and e_{min} conditions. These three averages demonstrate the proportional increase in thermal conductivity as the sample's saturation level rises.

A comparison of the empirical data with the theoretical lines reveals that thermal conductivity increases at an accelerated rate, even during the initial stages of saturation. This behaviour can be attributed to the inability of the water poured onto the top of the mould to drain to the deeper layers, which would otherwise facilitate homogeneous saturation throughout the entire sample. This effect is particularly pronounced under the e_{min} conditions.

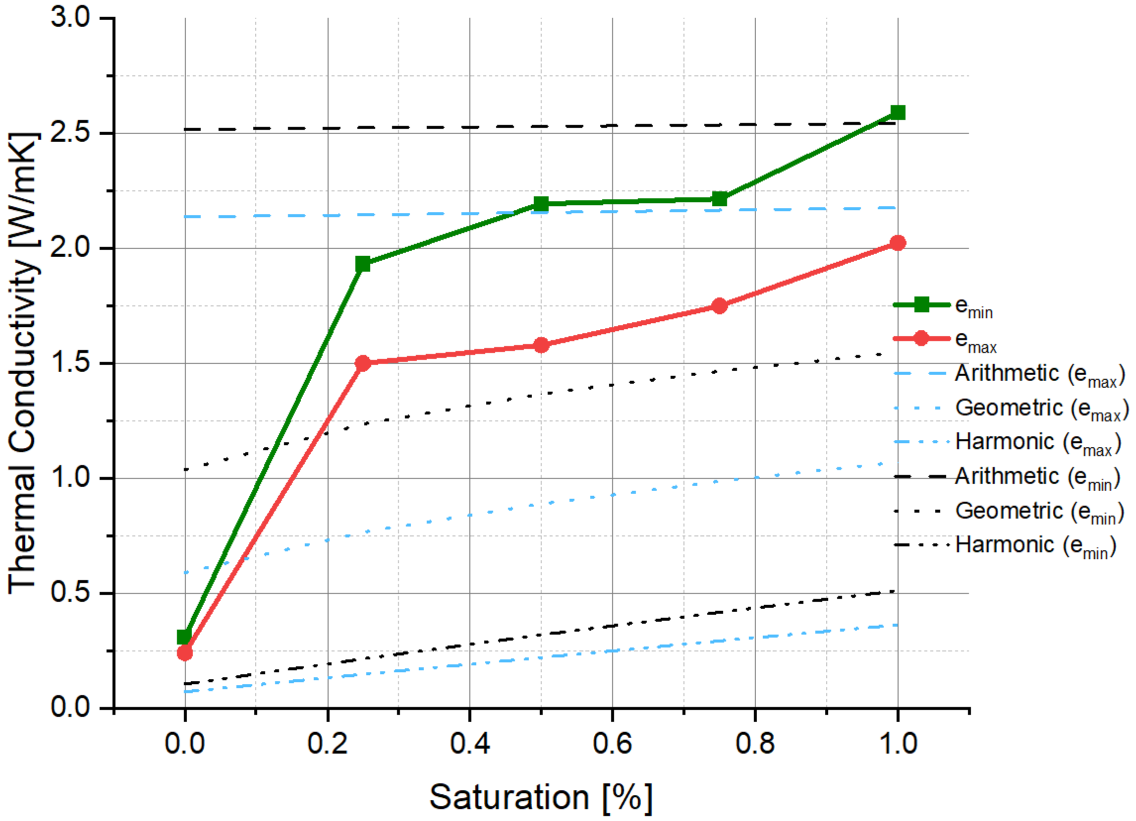

Figure 3.7 - Thermal conductivity variability in conditions of both minimum and maximum void index (e_{min} and e_{max} respectively) at different saturation levels. It is also depicted the arithmetic, geometric, and harmonic means for both the e_{min} and e_{max} conditions.

To prevent heterogeneities in the saturation of the sample, an alternative method was employed to achieve homogeneous saturation. The soil was placed into a container, and the appropriate amount of water was added to reach the required saturation percentage for the test (here considered the mixing methodology).

A second series of analyses were conducted to assess the variations observed compared to the previous method, with particular emphasis on the e_{max} and e_{min} conditions. The results were again compared to theoretical equations representing the arithmetic, geometric, and harmonic means of thermal conductivity at each specific saturation level, as proposed by Clauser and Huenges (1995).

The initial step involved calculating the function that represents the variation in thermal conductivity in air and water at different saturation levels in a solid (Eq. 3.2). This was achieved using the following formula:

$$\lambda_f = S \cdot \lambda_{H_2O} + (1 - S) \cdot \lambda_{air} \qquad \text{(Eq. 3.2)}$$

Where λ_f is the thermal conductivity of air and water combined, S is the saturation percentage, λ_{H_2O} is the thermal conductivity of water (0.59 W/mK) and λ_{air} is the thermal conductivity of air (0.026 W/mK) at laboratory temperature conditions. The equation allows for the calculation of the arithmetic (Eq. 3.3), geometric (Eq. 3.4), and harmonic mean (Eq. 3.5). To calculate these means, it is also necessary to determine the solid grain's thermal conductivity (λ_s) and porosity (ϕ).

$$k_{Arit.} = (\lambda_s \cdot (1 - \Phi)) + (\lambda_f \cdot \Phi) \qquad \text{(Eq. 3.3)}$$

$$k_{Geom.} = \lambda_s^{(1-\Phi)} \cdot \lambda_f^{\Phi} \qquad \text{(Eq. 3.4)}$$

$$k_{Harm.} = \frac{1}{\frac{(1-\Phi)}{\lambda_s} + \frac{\Phi}{\lambda_f}} \qquad \text{(Eq. 3.5)}$$

The calculated ϕ for the e_{max} was 0.32, while for the e_{min} it was 0.22. λ_s was assumed to be 3.3 W/mK.

Given the uncertainty surrounding the results presented in **Figure 3.8**, particularly in the context of e_{max} conditions where, at 75% saturation, the thermal conductivity is lower than at 50%, an alternative method was developed for testing the soil's thermal conductivity. The challenges encountered with the previously described methodology may have been due to the presence of coarse grains, which could have compromised the reliability of the results by interfering with the needle probe.

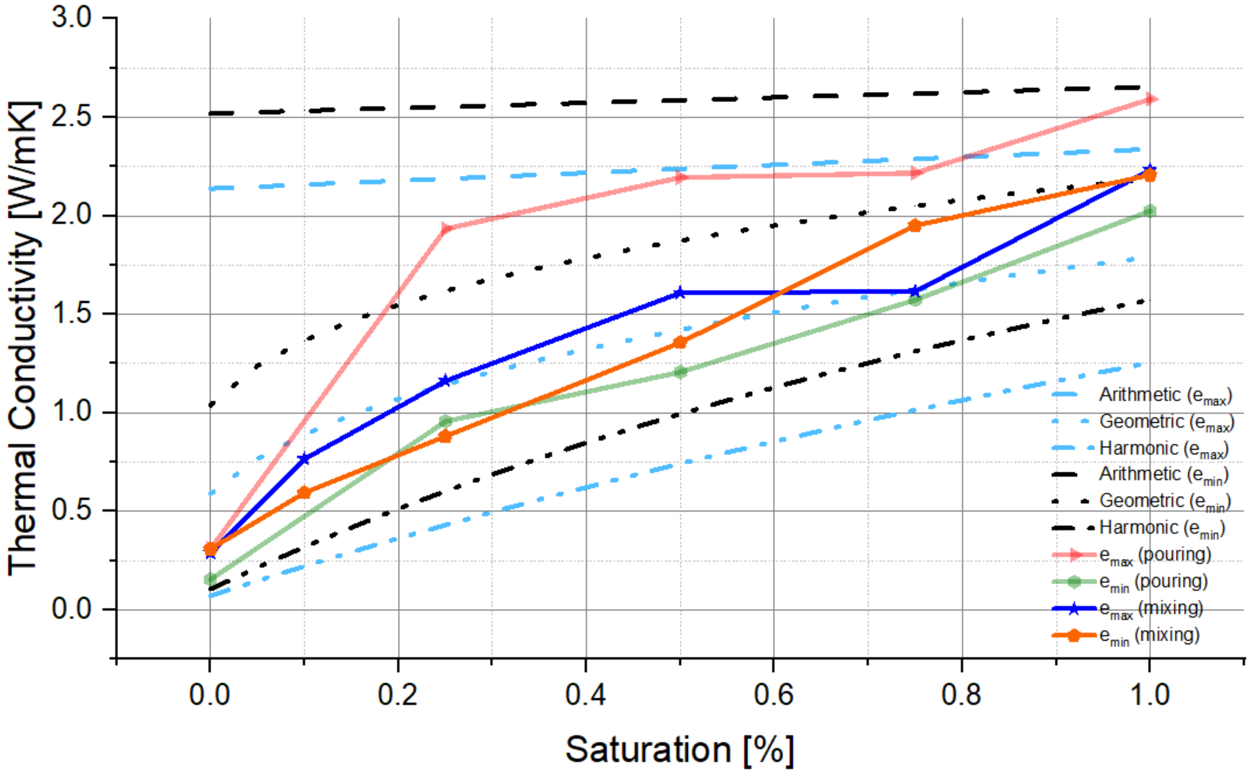

Figure 3.8 - Variability of thermal conductivity under both minimum and maximum void index conditions (e_{min} and e_{max}, respectively) at different saturation levels, for the two methods described (pouring water on top of the mould versus mixing the water with the soil before placing it in the mould). It also depicts the arithmetic, geometric, and harmonic means for both the e_{min} and e_{max} conditions.

Due to all the difficulties encountered in the previous methodologies, a further sample (CI9) was selected and subjected to a 2.63 mm sieving process to achieve a uniform grading and a finer grain size. This approach led to the development of an alternative method for testing soil samples. Smaller cylindrical containers were employed as moulds to facilitate more controlled testing conditions.

The resulting data were then compared to other theoretical equations proposed by various authors who have studied the thermal conductivity in porous unconsolidated materials (Woodside & Hessmer, 1961). Maxwell's equation (Eq. 3.6) is based on the assumption that the grains are representative of solid spheres. Consequently, the formula is only applicable when ϕ is such that the spheres are sufficiently spaced to avoid mutual interaction.

$$k_{Maxwell} = \lambda_f \cdot \left[\frac{2 \cdot \Phi \cdot \lambda_f + (3 - 2 \cdot \Phi) \cdot \lambda_s}{(3 - \Phi) \cdot \lambda_f + \Phi \cdot \lambda_s}\right] \quad \text{(Eq. 3.6)}$$

This formula was extended to ellipsoidal particles from De Vries (Eq. 3.7) for calculating the thermal conductivity of unconsolidated soil. This equation for a two-phase medium is expressed as:

$$k_{De\ Vries} = \frac{\Phi \cdot \lambda_f + (1-\Phi) \cdot F_1 \cdot \lambda_s}{\Phi + (1-\Phi) \cdot F_1} \qquad \text{(Eq. 3.7)}$$

Where F_1 (Eq. 3.8) is given by:

$$F_1 = \frac{1}{3} \cdot \sum_{i=1}^{3} [1 + (\frac{\lambda_s}{\lambda_f} - 1) \cdot g_i]^{-1} \qquad \text{(Eq. 3.8)}$$

In this equation, g_i represents the particle shape factors. For spherical grains $g_1 = g_2 = g_3$, reducing the equation to Maxwell's form. However, since De Vries assumes the particles are ellipsoidal, $g_1 = g_2 = 1/8$ and $g_3 = ¾$.

A final theoretical approach considered in this study was that of Kunii and Smith (Eq. 3.9), who proposed an equation for the conductivity of unconsolidated granular materials, neglecting radiation and heat conduction through the grain contacts:

$$k_{Kunii\ \&\ Smith} = [\Phi + \left(\frac{1-\Phi}{e + \frac{2}{3} \cdot \frac{\lambda_f}{\lambda_s}} \right) \cdot \lambda_f] \qquad \text{(Eq. 3.9)}$$

Where e (Eq. 3.10) is calculated as follows:

$$e = \frac{e_2 + (\Phi - 0.259) \cdot (e_1 - e_2)}{0.217} \qquad \text{(Eq. 3.10)}$$

The values of e_1 and e_2 are plotted as a function of λ_s/λ_f. In this context, e_1 represents a cubic packing of uniform spheres ($\phi = 0.476$), while e_2 symbolises a tetrahedral packing of uniform spheres ($\phi = 0.259$). In the event that the porosity is lower than 0.259, $e = e_2$; if it is greater than 0.476, $e = e_1$. For this study, ϕ was assessed to be 0.346, which represents an intermediate value. This assumption is valid, as it is based on a linear interpolation between e_1 and e_2.

To obtain a reliable λ_s, an X-ray diffraction (XRD) technique was employed to identify the presence of different mineralogical phases. This resulted in a conductivity value of 5 W/mK. **Figure 3.9** illustrates a more gradual increment in thermal conductivity with the rising saturation levels of the sample, compared to previous methodologies. The graph shows a clear consistency between the theoretical curve proposed by De Vries and the experimental data obtained from the sample.

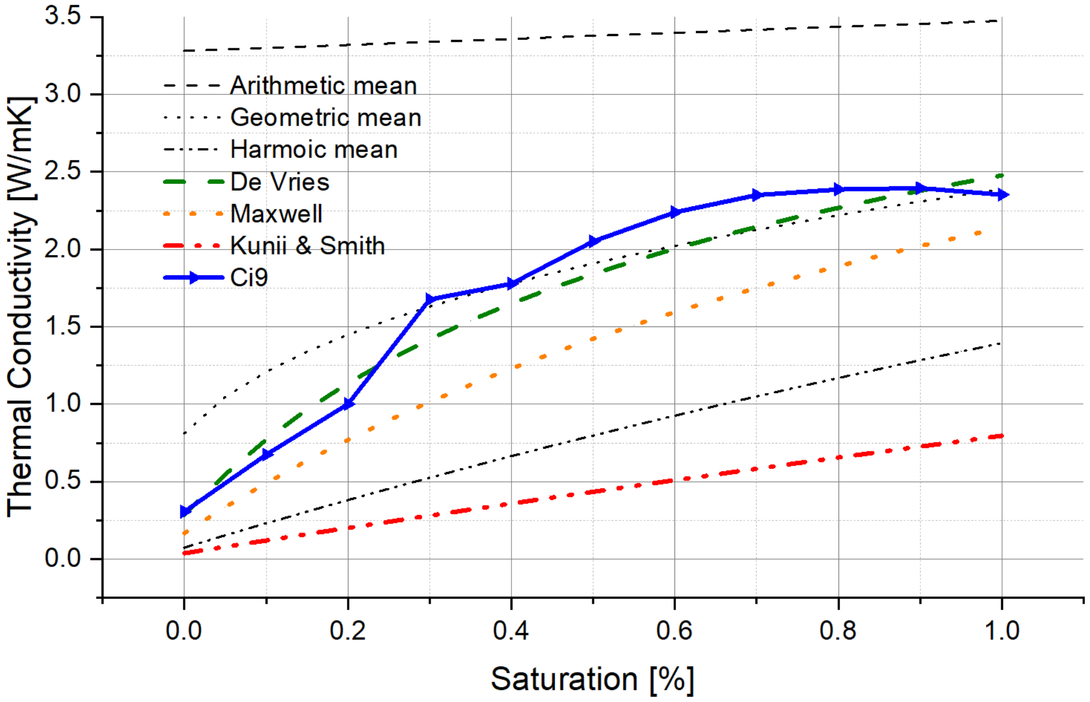

Figure 3.9 – Variability of thermal conductivity for sample Ci9 at different saturation levels. The figure also includes the arithmetic, geometric and harmonic means, and the theoretical functions of De Vries, Maxwell and Kunii & Smith.

3.4 Heat Flow Meter (HFM) instrument

Another instrument used for testing the thermal conductivity of soils is the HFM (ASTM, 2013) (**Figure 3.10**). This instrument requires a longer measurement period to yield reliable results. The apparatus consists of a box in which the sample is placed. Two thermal plates, equipped with thermistors, are positioned at the upper and lower extremes of the box. These plates are heated to different temperatures, ensuring that a steady thermal signal propagates through the sample. Prior to testing, it is essential to calibrate the instrument. Calibration involves using two standard specimens: one with a high thermal conductivity (Pyrex glass board) and the other with a low thermal conductivity (fibrous glass board). Once the sample is placed in the device, the upper plate is lowered until it makes contact with the sample's upper surface, ensuring a secure adhesion. The test follows the steady-state heat method, in which one plate is heated to a predetermined temperature and maintained at that level for the duration of the test. Meanwhile, the other plate measures the time taken for the thermal signal to pass through the sample, allowing for the calculation of the thermal conductivity and resistivity values.

Figure 3.10 – Heat Flow Meter (HFM) instrument.

3.4.1 HFM methods

This instrument has been designed for testing insulation products or construction materials, and therefore, exclusively solid objects. Since it was employed to test loose material, it was first necessary to evaluate the suitability of different containers in which the sample would be placed during the test. The objective was to identify a material that exhibited both high vertical thermal conductivity (to not reduce the propagation of the thermal signal) and high horizontal resistivity (to prevent the propagation of the signal out of the container), thereby ensuring the reliability of the measurement obtained from the instrument. As a base of both the containers considered, aluminium foil was employed, while the edges in the first case were composed of polystyrene (**Figure 3.11a**), and in the second case, some hard rubber was utilised (**Figure 3.11b**).

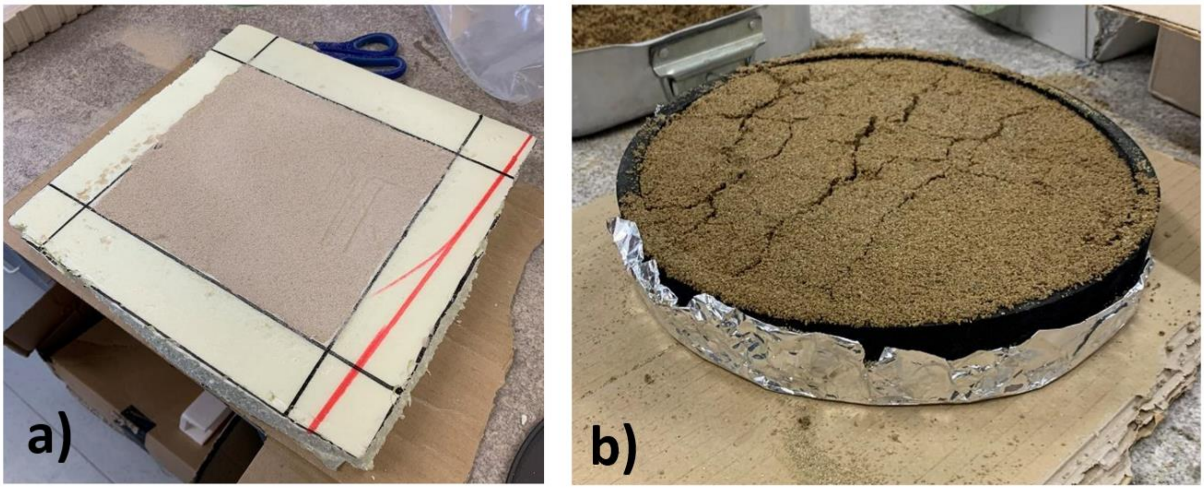

Figure 3.11 – Two of the containers selected for the test, each with a different shape and composition.

The two containers tested were found to lack the necessary rigidity to maintain the sample's position during deployment. Upon movement of the container within the instrument, fractures were generated on the sample's surface, resulting in misleading thermal conductivity values. As a definitive solution, a silicone cake pan with a more rigid structure than the aluminium foil was tested (**Figure 3.12**). The instrument calibration was set for testing materials with high thermal conductivity (Pyrex glass board).

Figure 3.12 - Container selected for conducting the thermal conductivity test.

3.5 Comparison of the outcomes

The thermal conductivity results obtained from the CI9 specimen utilising the HFM were compared with those from the needle probe tests. The HFM instrument was unable to achieve saturation levels beyond 60%. This limitation arose because, at higher saturation levels, the pressure exerted by the two platens on the sample, increased the risk of water escaping from the silicone cake pan and potentially damaging the instrument. As mentioned earlier, the HFM was specifically designed for testing solid, water-free materials. Nevertheless, despite the challenges in developing a reliable method for testing the sample using both instruments, **Figure 3.13** illustrates a notable consistency in the variation of thermal conductivity with increasing saturation levels across the two methods.

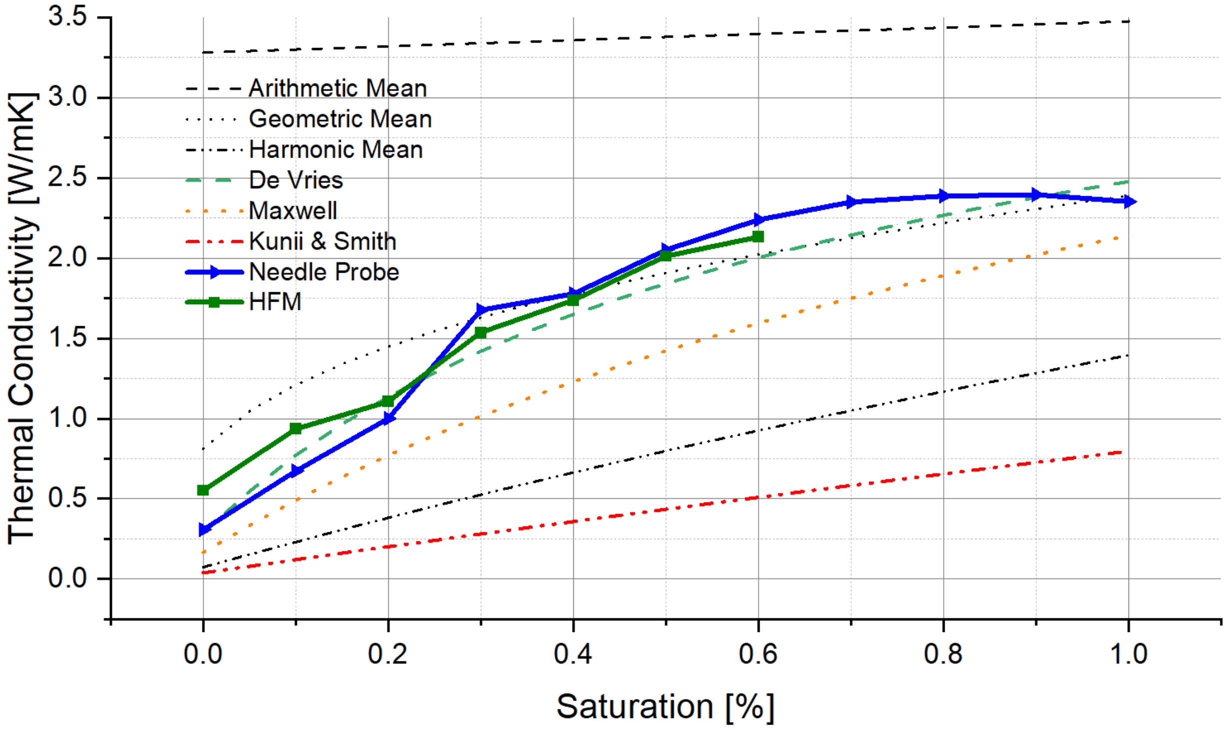

Figure 3.13 – Thermal conductivity variation of the Ci9 sample tested with both instruments across different saturation levels. The figure also includes representations of the arithmetic, geometric and harmonic mean, alongside the theoretical model proposed by De Vries, Maxwell and Kunii & Smith.

3.6 Summary

This section outlines the thermal characterization of soils for geothermal applications, emphasising the measurement of thermal conductivity, a critical parameter for determining the potential thermal energy extraction from underground environments. It also details the methodologies employed, including the collection and preparation of soil samples.

Two primary devices were utilized to assess thermal conductivity: the TLS-100 needle probe and the HFM.

The TLS-100 needle probe operates by generating and monitoring heat within the sample. Initial tests focused on intact core portions, followed by evaluations on reconstructed samples at varying saturation levels. Water was gradually added to the sample in a mould to analyse the relationship between saturation and thermal conductivity. Early findings revealed that uneven water distribution caused oversaturation in the upper portions of the sample, affecting the results. To address this, new preparation methods ensured uniform saturation by mixing soil with precise water volume before testing.

The HFM, while primarily designed for solid materials, was adapted to test loose soils by evaluating different container materials to control heat propagation. However, attaining high saturation levels posed significant challenges due to the risk of water leakage, a limitation tied to the instrument's design specifically for solid objects.

Results from both instruments showed consistent trends in thermal conductivity with varying saturation levels. A comparison of empirical data with theoretical models from established authors demonstrates strong agreement, validating the observed conductivity trends despite methodological challenges.

4. Hydrogeological parameterisation

In the context of the ongoing collaboration between the University of Bicocca and the Milan Metropolitans (MM) company, besides the monitoring activity of the aquifer through the use of its piezometer, a series of tests carried out on different boreholes drilled due to the extension of the various tube lines of Milan's Metropolitan City (MCM) were shared. The aim was to analyse the geotechnical data, in particular, the grain size distribution (GSD) and the AGI soil description classification. By obtaining this information, the hydraulic conductivity (K) was estimated using several theoretical formulas. In other words, for each GSD describing a particular horizon, a hydrofacies was assigned, but also a range of hydraulic conductivity values was calculated representing a particular layer.

4.1 Data acquisition

The data were sheared from MM in PDF format and included 69 borehole logs for the entire length of the Metropolitan Line 4 (M4), 50 boreholes for the north-eastern extension of the M5 line, and 20 borehole logs for both the north-eastern and south-western extensions of the M1 line. Additionally, six borehole logs were obtained from ongoing construction activities at three distinct buildings within the University of Bicocca campus. Historical data contributed another 20 borehole logs, which were sourced from the University archives and pre-processed in prior research (De Caro et al., 2020). In total, 1485 horizons were described by GSD curves, from which the relative percentages of gravel (G), sand (S) and clay together with silt (C+S) were calculated.

Figure 4.1 shows the spatial distribution of the borehole logs information shared from MM used to evaluate the hydraulic conductivity in the city of Milan.

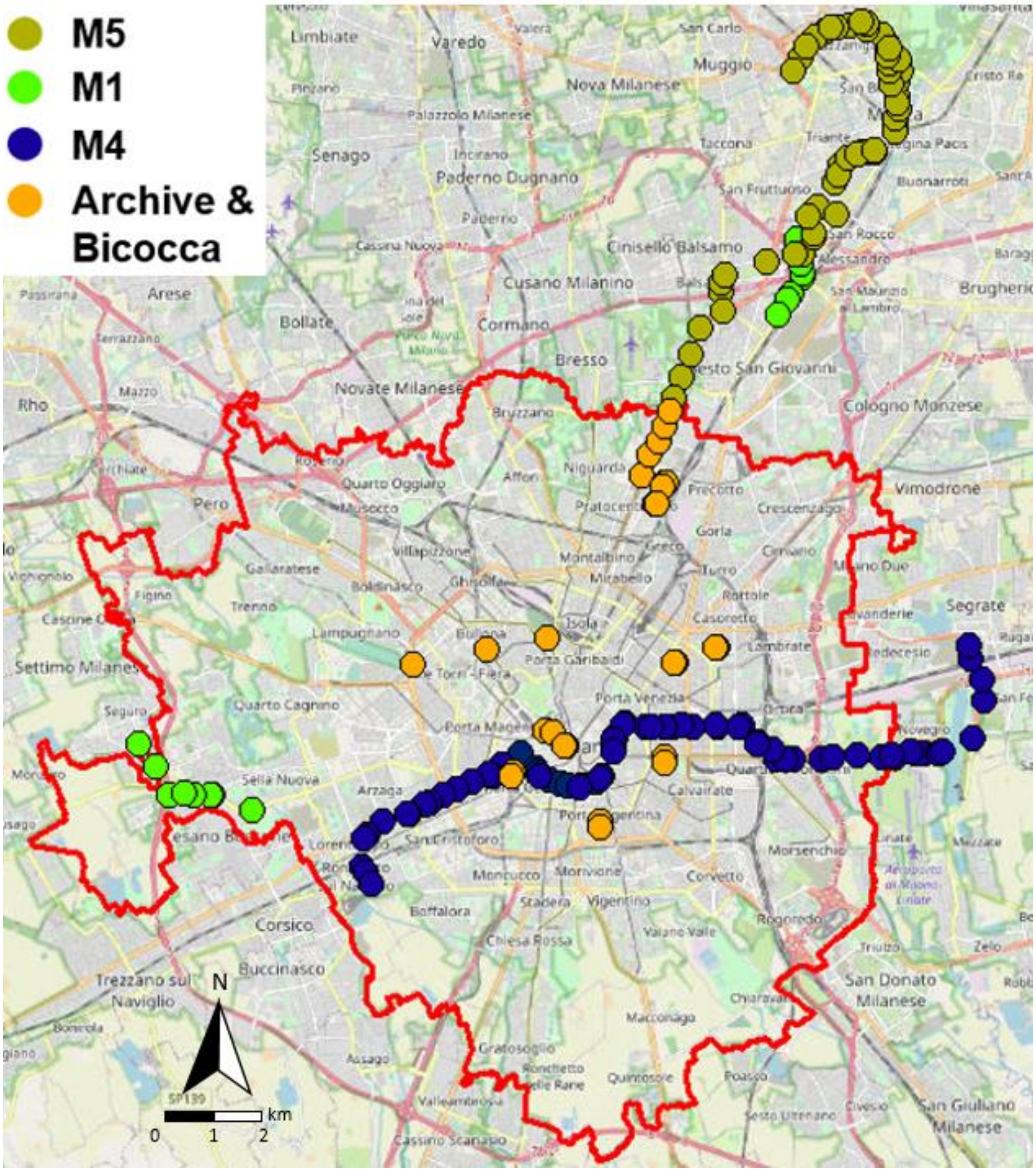

Figure 4.1 - Distribution of the borehole logs considered in the Metropolitan City of Milan shared by MM.

All PDFs and documents from the university archives were digitised and integrated into a database containing the borehole and layer identification code, site coordinates, depth and absolute elevation at which the test was carried out, including the relative GSDs curves. Given that the tests were conducted by various geological companies, discrepancies were observed in the spacing of sieve diameters across the GSD data. To address this, a MATLAB script was developed to standardize the data by performing linear interpolation across the diverse sieve intervals, thereby creating a consistent sieve spacing for all tests. Another MATLAB code was then used to interpolate linearly all the percentiles of the material passing through the sieves (d_{10} - d_{20} - d_{30} - d_{40} - etc.), useful for calculating the uniformity (C_u) and the consolidation coefficient (C_c). From the GSDs data, the relative proportions of gravel (G), sand (S) and clay together with silt (C+S) were calculated for each test. Separations were based on the minimum class diameter (i.e., 2 mm for gravel-sand, 0.06 mm for sand–clay, and 0.002 mm for clay-silt). These proportions were used to assign a specific soil name to each horizon tested for its GSD. The dataset was condensed following the Italian geotechnical association (A.G.I., 1963) guidelines, classifying the lithotypes into four primary grain size classes (gravel, sand, silt and clay) and three rock/cemented deposit classes (generic rock, sandstone and conglomerate), while the abundances were simplified into 4 unique values (>50, 50-25, 25-10 and <10%), as shown in **Table 4.1**.

Table 4.1 - Examples of qualitative soil descriptions according to the Italian geotechnical association (A.G.I., 1963) and the relative percentage intervals for each grain size class. For the same demonstrative units, it is shown the classification by the regional geological database of Lombardia and the corresponding hydrofacies class as proposed by this study. G = gravel, S = sand, L = silt, and C = clay.

	% of grain size class				*Classification in Lombardia*					
Description	**G** (%)	**S** (%)	**L** (%)	**C** (%)	L1	L2	P2	L3	P3	**Class**
Gravel with sand	>50	50-25	-	-	**G**	**S**	50-25			**GS**
Gravelly silt with sand	25-10	50-25	>50	-	**L**	**S**	50-25	**G**	25-10	**LSG**
Sand poorly silty	-	>50	<10	-	**S**	**L**	<10			**S**
Clayey, poorly gravelly silt with sand	10-5	50-25	>50	25-10	**L**	**S**	50-25	**C**	25-10	**LSC**

The nomenclature was carried out based on the A.G.I. regulation, for which specific letters (up to three) were assigned according to the abundance of the grain size class percentages. The hierarchical classification by the Lombardia region was aggregated into single terms of up to three single letters (G, S, L or C) obtaining a total of 26 hydrofacies classes (23 for unconsolidated deposits in **Table 4.2**, and 3 for cemented deposits or rocks), as defined by De Caro et al. (2020).

Table 4.2 - Hydrofacies classes used in this study from the work of De Caro et al. (2020) with the associated mean values of porosity and hydraulic conductivity (K), and average abundances of grain size classes. G = gravel, S = sand, L = silt and C = clay. Method reference for the attribution of the hydraulic conductivity: (1) Hazen (1982); (2) Kozeny (1953); (3) Breyer (1964); (4) Slichter (1899); (5) Alyamani and Sen (1993); (6) Chapuis (2004); (7) Harleman (1963).

Hydrofacies	Porosity	K (m/s)	Methods	% Gravel	% Sand	% Silt	% Clay
G	0.26	9.0E-02	(15) (17) (11)	100			
GS	0.29	2.4E-03	(5) (7) (1)	70	30		
GL	0.34	6.1E-04	(6) (3) (7)	70		30	
GC	0.38	6.7E-04	(6) (3) (7)	70			30
GSL	0.30	1.5E-05	(5) (7) (1)	60	25	15	
GSC	0.30	1.2E-05	(5) (7) (1)	60	25		15
S	0.34	5.8E-05	(6) (7) (2)		100		
SG	0.31	5.5E-04	(6) (7) (1) (2)	30	70		
SGL	0.30	9.8E-06	(6) (3) (7) (1) (2)	25	60	15	
SGC	0.30	2.8E-04	(6) (3) (7) (1) (2)	25	60		15
SL	0.34	2.2E-05	(6) (3) (7) (1) (2)		70	30	
SLC	0.27	4.3E-06	(6) (3) (7) (1) (2)		60	25	15
SLG	0.33	5.9E-06	(6) (3) (7) (1) (2)	15	60	25	
SC	0.32	1.1E-05	(7)		70		30
SCG	0.33	1.6E-05	(7)	15	60		25
L	0.44	9.5E-06	(7)			100	
LG	0.35	6.9E-06	(7)	30		70	
LS	0.30	5.6E-06	(7)		30	70	
LC	0.40	8.2E-06	(7)			70	30
C	0.50	3.2E-08	(7)				100
CG	0.46	3.4E-06	(7)	30			70
CS	0.43	5.5E-06	(7)		30		70
CL	0.45	1.2E-07	(7)			30	70

4.2 Theoretical equations

Different empirical equations were proposed to derive a range of K_h values from the GSD data (Odong, 2007; Hussain & Nabi, 2016; Feng et al., 2019; Kasenow, 2002), which consider the relation between several grain size parameters to estimate *K*.

Hazen was one of the first to develop a formula to correlate grain size parameters with *K* in 1892. It was originally created to determine *K* for uniformly graded sands, but it can also be used for fine sands to gravel as long as the C_u is less than 5 and the effective grain size is between 0.1 and 3 mm. Hazen (Eq. 4.1) proposed the following equation:

$$K = \frac{g}{v} \cdot 6 \cdot 10^{-4} \cdot [1 + 10 \cdot (n - 0.26)] \cdot d_{10}^2 \qquad \textit{(Eq. 4.1)}$$

Where *g* = gravity acceleration; *v* = kinematic viscosity; *C* = sorting coefficient; *n* = porosity.

The Kozeny equation (1953) is used to calculate *K* in the case of coarse sands (Eq. 4.2). The proposed equation is the following:

$$K = \frac{g}{v} \cdot 8.3 \cdot 10^{-4} \cdot [\frac{n^3}{(1-n)^2}] \cdot d_{10}^2 \qquad \textit{(Eq. 4.2)}$$

Breyer formula was proposed in 1964 (Eq. 4.3) and does not account for porosity, therefore, the function of this parameter is assumed to have a value of 1. It applies mostly to materials with heterogeneous distributions and poorly sorted grains. It is best used when the uniformity coefficient ranges between 1 and 20, and the effective grain size lies between 0.06 mm and 0.6 mm. Here is presented his equation:

$$K = \frac{g}{v} \cdot 6 \cdot 10^{-4} \cdot log \frac{500}{U} \cdot d_{10}^2 \qquad \textit{(Eq. 4.3)}$$

Slichter equation (Eq. 4.4) was suggested in 1899 and is mostly applicable to grain size between 0.01 mm and 5 mm.

$$K = \frac{g}{v} \cdot 10^{-2} \cdot n^{3.287} \cdot d_{10}^2 \qquad \textit{(Eq. 4.4)}$$

The formula proposed by Alyamani & Sen in 1993 takes into account the sorting characteristics and both the d_{10} and the d_{50} (Eq. 4.5). Here is presented his equation:

$$K = 1300 \cdot [I_0 + 0.025 \cdot (d_{50} - d_{10})]^2 \qquad \textit{(Eq. 4.5)}$$

Where I_0 is the intercept (in mm) of the line formed by connecting d_{50} and d_{10} with the grain size axis.

Chapuis (2004) developed a predictive equation (Eq. 4.6) that incorporates the term $\frac{e^3}{1+e}$ into the Kozeny equation, along with d_{10}^2 from Hazen's formulation. This formula can be used for non-plastic materials, but may not be accurate enough when applied to crushed samples. It is expressed as:

$$K = 2.4622 \cdot [\frac{d_{10}^2 \cdot e^3}{1+e}]^{0.7825} \qquad \textit{(Eq. 4.6)}$$

Furthermore, Harleman in 1963 (Eq. 4.7) converts the *K* with the permeability *(k)*, which is a property that depends exclusively on the characteristics of the skeletal grains within the porous medium. k is typically measured in cm^2. For water at a temperature of 20°C, the following conversion applies to relate k and *K*:

$$K = 1\frac{cm}{s} \equiv k = 1.02 \cdot 10^{-5} cm^2 \qquad \textit{(Eq. 4.7)}$$

The equation (Eq. 4.8) according to Harleman et al. (1963) is:

$$k = 6.54 \cdot 10^{-4} \cdot d_{10}^2 \qquad \textit{(Eq. 4.8)}$$

As shown in Table 4.2 each formula considered is used for specific grain sizes and grading, so according to each horizon analysed for its grain size distribution a specific equation was used.

4.3 Grain size analysis and hydrofacies definition

Complete GSD were performed following ASTM D6913 and ASTM D7928 standards for sieve and sedimentation analysis respectively on all the 1485 horizons identified in the 165 boreholes considered. The GSD curves obtained from the analysis were classified according to hydrofacies, based on the corresponding borehole and sample depth. Following the methodology outlined by De Caro et al. (2020), characteristic grain size diameters were extracted from the GSD curves. These parameters were then used to estimate K and porosity using various empirical equations from the literature, as summarised in Table 4.2.

Figure 4.2 presents, on the left, the GSD curves used for parameterization, illustrating the variability in grain size distributions across hydrofacies; and, on the right, the variability in estimated K values among hydrofacies.

This approach provides insights into the hydraulic properties and porosity characteristics of the different hydrofacies within the study area.

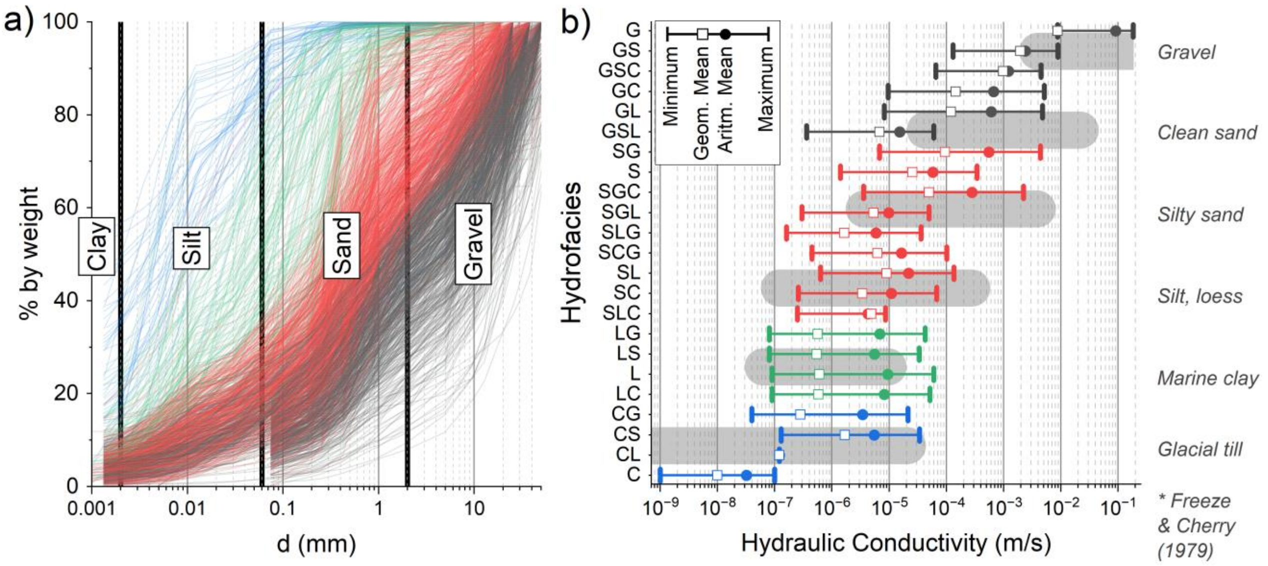

Figure 4.2 - (a) Grain size distributions analysed in this study, comprising a total of 1,485 samples. (b) Estimated hydraulic conductivity (K) values derived from empirical correlations for each hydrofacies class, compared with reference values proposed by Freeze and Cherry (1979). The hydrofacies classes include Gravel (G), Sand (S), Silt (L), and Clay (C).

Laboratory analysis revealed that the three sediment classes with very high to absolute clay content (C: 'clay', CL: 'clay and silt', and CS: 'clay and sand') consistently contained more silt than clay. This discrepancy is likely due to a human bias in visually analysing very fine sediments, where these materials are often labelled as clay rather than silt because distinguishing between the two quantitatively is challenging. This interpretation aligns with established classification systems like the ASTM D2488 standard, which collectively refers to both silt and clay as fines.

4.5 Use of data

The data collected by digitalising the documents containing the GSD tests were implemented in an already existing database. The data set was originally created by De Caro et al. (2020) for his previous studies. In the following years, the project was carried on by Alberto Previati, a researcher of the geothermal team at the University of Milan Bicocca. He managed to gather several types of information in the database, as well as increase its spatial distribution, including the whole Po plane (some parts of Veneto, Emilia-Romagna and Piedmont regions). The study area includes various depositional systems such as alluvial fans, plains, and nearshore environments, contributing to significant subsurface heterogeneity. The information gathered includes stratigraphic logs (collected from both regional and national datasets), GSD analysis, Lefranc and well tests, but also groundwater (GW) head. The information included in the database are summarised in **Table 4.3**.

Table 4.3 - Main data used in this study. The sources are given in the bottom line of the table for the regional (from 1 to 4) and national (5) geological datasets. (*) Grain size data from the Piedmont regional dataset is given as an abundance of the four main grain size classes. (**) GSD and Lefranc data for the Lombardy region are retrieved from geological reports from private projects available to the authors. Groundwater head data are available as point measurements (P) or contour lines (Cont.).

Region	Area (km^2)	**Stratigraphic Logs**		**Direct Tests**			**Groundwater head**	
		Regional	*National (5)*	*GSD*	*Lefranc*	*Well tests (5)*	*Type*	*Year*
Piedmont(1)	9,733	8,675	2,069	3,093*	554	1,902	Cont.	2002
Lombardy(2)	13,229	18,020	3,465	1,485**	343**	3,100	P (840)	2014
Veneto(3)	11,205	N.A.	4,173	N.A.	N.A.	2,999	P (279)	2014
Emilia-Romagna(4)	11,523	N.A.	2,863	N.A.	N.A.	2,400	P (458)	2017

(1) https://geoportale.arpa.piemonte.it/ (2) https://www.geoportale.regione.lombardia.it/ (3) https://www.arpa.veneto.it/
(4) https://dati.arpae.it/tl/dataset/acque-sotterranee-2017 (5) https://www.isprambiente.gov.it/it/banche-dati

By the application of an advanced Long Short-Term Memory (LSTM) neural network were classified geological descriptions of 39,265 boreholes into hydrofacies based on grain size. The primary goal was to create a semi-quantitative dataset for hydrogeological modelling, addressing the region's GW management challenges. **Figure 4.3** shows the location of the boreholes considered in this study, the training and validation sets included 9,316 boreholes marked in red, while the rest comprised the prediction sets (29,949). The piezometric level of the shallow aquifer was obtained by combining linear (i.e., GW head isolines) and pointwise (i.e., GW head from well measurements) data from four different sources spanning about 15 years (**Table 4.3**).

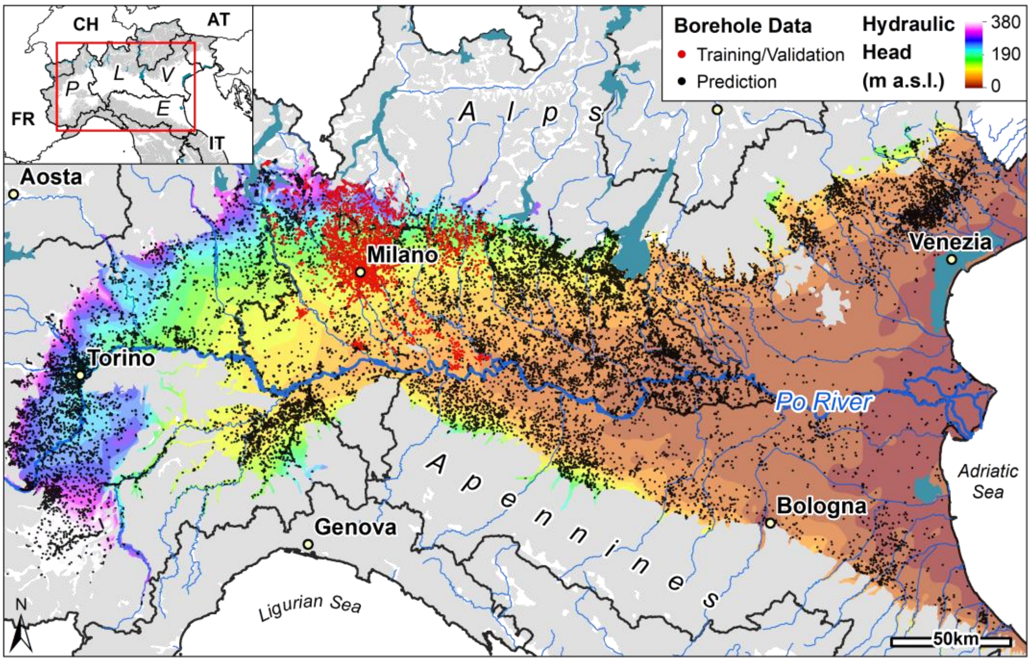

Figure 4.3 - Map of the study area (Po Plain) illustrating the spatial distribution of stratigraphic logs used in the research. Logs marked in red represent those used for training and validation, while logs marked in black were used for prediction. Additionally, the map shows the hydraulic head of the shallow aquifer during the period 2002–2017. An inset highlights the four Italian regions included in the study: Piedmont (P), Lombardy (L), Veneto (V), and Emilia-Romagna (E). The map also highlights differences in data density: regions P and L benefit from regional geological databases in digital format, while regions V and E rely solely on the national geological database, resulting in lower spatial data density.

The developed classification system standardizes borehole descriptions into 26 hydrofacies categories, incorporating advanced Natural Language Processing (NLP) and word embedding techniques for precise text analysis. This method enhances classification accuracy to approximately 97% and facilitates spatial reconstruction of hydrofacies. Furthermore, the study validates its model by comparing its predictions with high-resolution borehole data and independent GSD analyses, highlighting robust alignment with established geological features.

The findings were validated against a historical hydrogeological map (**Figure 4.4a**) available from the National Geological Service. **Figure 4.4b** shows the spatial distribution of the deposit's grain size variation. Spatially, the northern plain features gravelly deposits transitioning to sandy and finer units southward, reflecting diminishing depositional energy. In contrast, the southern Apennine sector exhibits fine sediments due to the dominance of mudrocks in the source area. Using the k-means clustering of grain size variables (method #1) and Kriging interpolation (method #2), the study delineates hydrogeological domains characterized by hydraulic conductivity variations, shown in **Figure 4.4c**. The comparison against the historical maps yielded a promising classification accuracy.

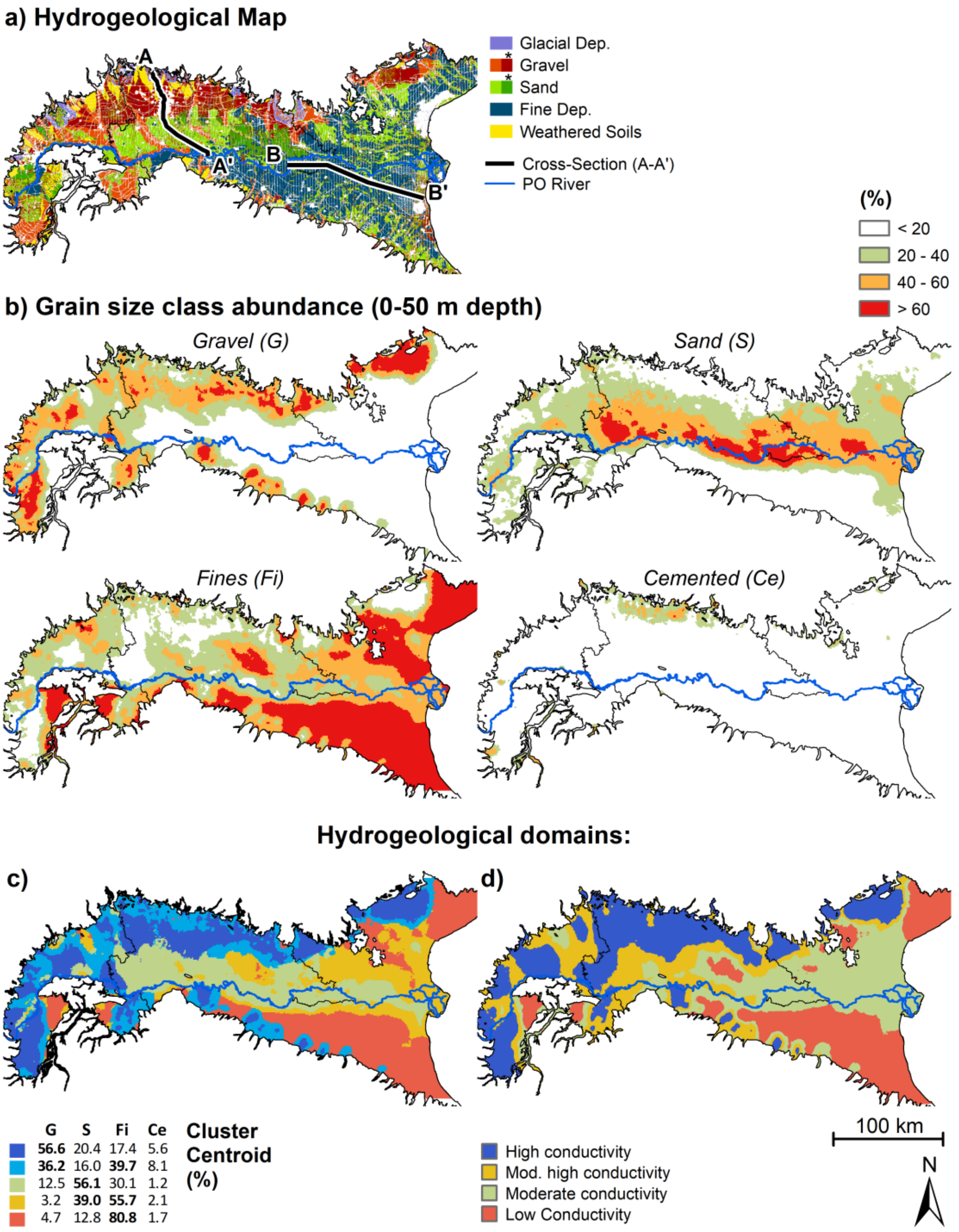

Figure 4.4 - (a) Hydrogeological map, produced by Servizio Geologico Nazionale (1998), depicts the characteristics of shallow deposits. This map is compared with (b) the predicted maps showing the percentages of gravel (G), sand (S), fines (silt + clay, Fi), and cemented (Ce) deposits in the shallow subsurface (up to 50 meters depth). (c-d) Hydrogeological domains derived by two distinct methods: clustering grain size class abundances, with the legend indicating the centroids of each cluster and the most significant class

highlighted in bold (method 1#). Spatialisation and classification based on Kriging interpolation of the hydraulic conductivity (K_{eq}).

Furthermore, the research also incorporates detailed cross-sectional and three-dimensional models.

Two regional cross-sections illustrate the transition from coarse-grained alluvial fans to finer, distal deposits, and the variability of aquifer connectivity. These models highlight hydrogeological boundaries, such as aquitard and highly permeable layers, enhancing the understanding of GW flow and storage dynamics. However, limitations persist in regions with sparse data or complex stratigraphy, such as the San Colombano structure.

Figure 4.5b shows a north-south cross-section (AA') (see **Figure 4.4a** for the trace of the section) visible in the upper Po Plain, north of the Po River, which transitions from proximal Alpine depositional facies (coarse alluvial fan deposits) to distal facies (sandy plains and post-glacial sediments). A reference hydrogeological cross-section from Regione Lombardia (2016) delineates permeable units (shallow and deep aquifers) and low-permeability layers (**Figure 4.5a**). The section is bounded by the topographic surface above and the base of the intermediate aquifer unit below, as defined by prior studies and GW management plans. The most accurate method is the clustering method (Method #1) (**Figure 4.5d**), achieving a classification accuracy of 0.72. An alternative approach based on hydraulic conductivity (Method #2) (**Figure 4.5e**) achieves slightly lower accuracy (0.66). The results highlight a transition from highly permeable to less permeable domains in the phreatic aquifer, consistent with the presence of natural springs. Both methods identify a low-conductivity horizon (aquitard) separating the shallow and intermediate aquifers, though connectivity varies by method. However, the models face limitations in the San Colombano area, where sparse data and complex stratigraphy hinder reliable predictions. To avoid inaccuracies, this area is excluded from the modelling domain.

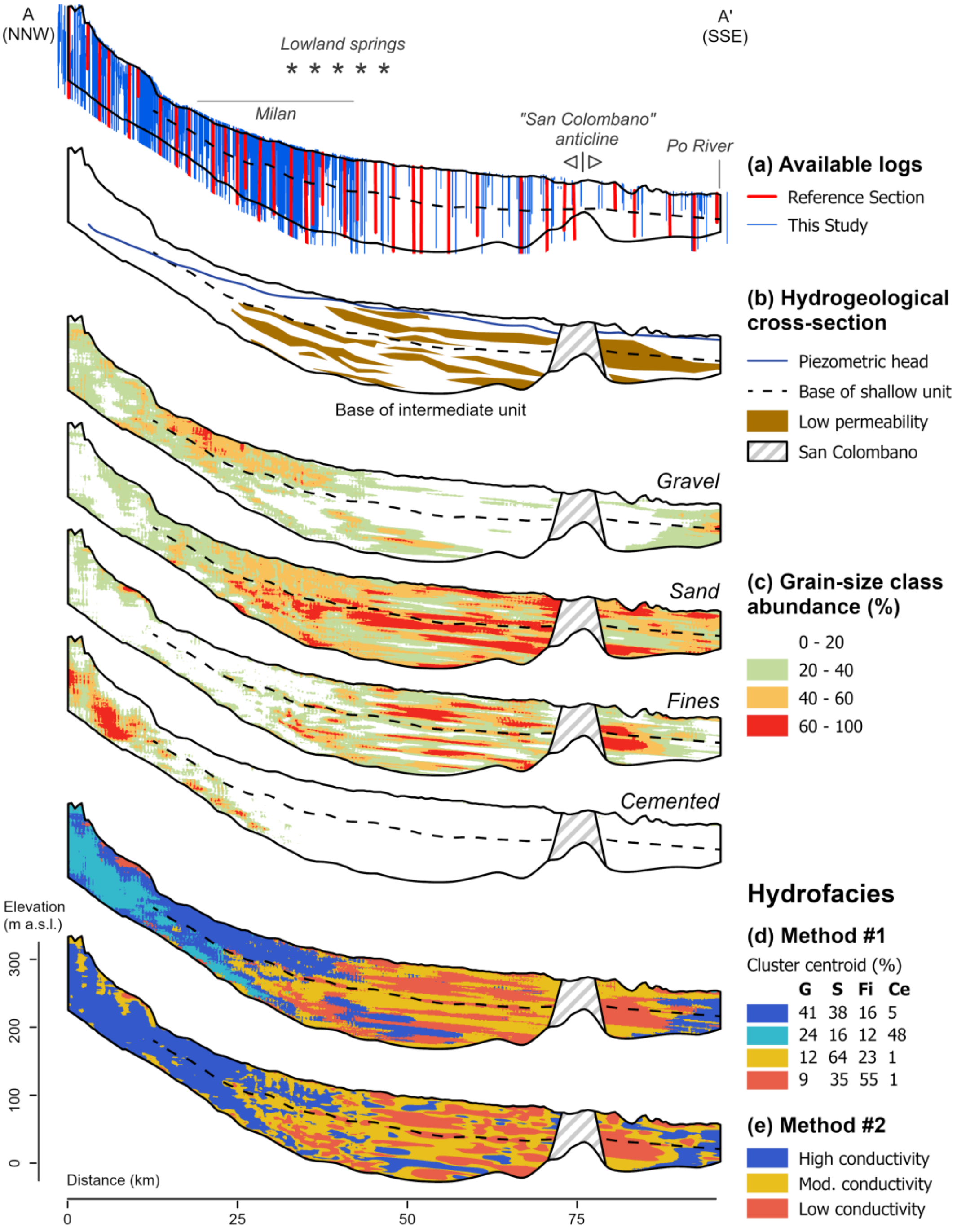

Figure 4.5 - Hydrogeological cross-section, adapted from Regione Lombardia (2016). This cross-section displays (a) available borehole logs and (b) the characteristics of subsurface deposits. The lowland springs ("Fontanili") belt is indicated by asterisks, while the isolated San Colombano relief is highlighted with oblique hatching. The figure includes (c) cross-sections illustrating the predicted percentages of gravel (G), sand (S), fines (silt + clay, Fi), and cemented deposits (Ce) as determined by classification and interpolation models. The spatial distribution of homogeneous hydrofacies is presented through two methods: (d) method #1, which clusters grain size class abundances (the legend shows cluster centroids with the most relevant class in bold), and (e) method #2, which involves specialization and classification of hydraulic conductivity.

Please note that the vertical scale is exaggerated 100 times for clarity.

Overall, this study demonstrates the potential of artificial intelligence-driven geological classification in generating high-resolution hydrogeological data from qualitative inputs. It emphasizes the importance of integrating automated tools with expert geological knowledge to overcome challenges in data standardization and spatial representation. By enriching subsurface models with detailed hydrofacies information, the methodology significantly advances regional GW research and management strategies in heterogeneous settings.

4.6 Summary

This study focuses on integrating artificial intelligence (AI) and geological expertise to enhance hydrogeological modelling in the Po Plain, northern Italy. The research uses an LSTM neural network to classify geological data into hydrofacies based on grain size. By processing descriptions from over 39,000 boreholes, the study transforms qualitative data into semi-quantitative hydrogeological insights. The study area encompasses 45,700 km² of heterogeneous subsurface conditions, shaped by Alpine and Apennine depositional systems. Data used include stratigraphic logs, grain size analyses, hydraulic conductivity tests, and GW head measurements. The dataset gathers borehole records into 26 hydrofacies categories, integrating regional and national databases. MATLAB tools facilitated the digitalisation of the GSD analysis, and empirical formulas were used to estimate hydraulic conductivity k-values.

The LSTM model achieved approximately 97% classification accuracy and was validated against laboratory analyses and high-resolution borehole logs. Spatial variability in deposits was analysed using clustering and interpolation methods. Gravel-rich deposits dominate the northern plain, transitioning to sandy and fine-grained sediments southward. Hydrofacies maps and cross-sections reveal transitions in hydraulic conductivity and aquifer connectivity.

A north-south cross-section (AA’) illustrates depositional transitions from coarse Alpine alluvial fans to finer distal deposits, consistent with the presence of natural springs. Two methodologies were employed for hydrofacies spatialisation: by k-means clustering of grain size variables (Method #1) and classifying hydraulic conductivity (Method #2). Both approaches captured the transition from highly permeable to low-permeability domains but faced limitations in regions with sparse data or complex geology.

The study's approach enhances data density from 0.34 to 8.7 data points per km² and offers detailed 3D hydrogeological representations. Key findings include a low-permeability aquitard separating shallow and intermediate aquifers and the identification of cemented conglomeratic formations. However, challenges remain in areas like the San Colombano structure due to sparse data and complex stratigraphy.

Overall, this research highlights the transformative potential of AI-driven geological classification in hydrogeological studies. By standardizing qualitative data and integrating spatial modelling techniques, the methodology provides valuable tools for regional GW management and subsurface characterization.

5. Numerical model generation

This chapter is largely based on the following paper:

→ Silvestri, V., Crosta, G., Previati, A., Frattini, P., & Bloemendal, M. (2025). Uni-directional ATES in high groundwater flow aquifers. Geothermics, 125, 103152.

https://doi.org/10.1016/j.geothermics.2024.103152

5.1 Methods

A sensitivity analysis based on a hydrothermal dynamic model is proposed to assess the feasibility by varying a wide range of relevant geothermal systems and aquifer characteristics.

5.1.1 Model description

To take into consideration all the physical properties governing the groundwater (GW) heat flow, such as thermal conduction and advection, flopy package (Bakker et al, 2016) for running MODFLOW (Harbaugh et al., 2000) MT3DMS transport code (Zheng & Wang, 1999) have been used. This 3D Finite Difference numerical Model (FDM) solves the GW flow and heat transport equations, allowing the simulation of the extraction and injection of the GW from wells, the hydrodynamic regime, and the thermal transport, like in other previous studies conducted on Aquifer Thermal Energy Storage (ATES) systems (Bloemendal & Hartog, 2017; Rostampour et al., 2019; Bloemendal & Olsthoorn, 2018).

5.1.2 Setting model's parameters

A synthetic box model was generated with the following characteristics:

- Model layers: the thickness of the main aquifer is 20 m (horizontal hydraulic conductivity [K_h] is 10 m/d), and it is confined by two clay horizons (K_h = 0.05 m/d) with the same thickness. The vertical hydraulic conductivity is considered 1/5 of the horizontal hydraulic conductivity and the porosity for all the layers is 0.3. Each layer is divided into four simulation layers, obtaining 12 slices of 5 m for the whole vertical discretization of the model (**Figure 5.1a**).

- Boundary conditions: the model boundaries are constant head and temperature of 15°C. The head boundaries are varied during the sensitivity analysis chosen such that the gradient together with the hydraulic conductivity result in different GW flow velocities, ranging from 3 m/y up to 1000 m/y. Fluid sink and source terms are applied at well locations (extraction and injection well, respectively) to simulate the operative configuration of the system. An additional temperature differential is applied to the reinjected water to the temperature of the extracted water using a Dirichlet-type boundary condition.
- Spatial discretization: the horizontal grid is 10 x 10 m in size around the wells, gradually increasing up to 100 x 100 m at the edges of the model (**Figure 5.1b**). The element size of the central part of the grid was chosen to obtain good accuracy minimizing the computation time for each model. This parameter was evaluated for squares of 3, 5, 10, 20, 50 and 70 m displaying an incremental error according to the efficiency outcome (the baseline considered is for 3x3 m square grid). With a grid of 10x10 m, the error is kept below 5% and only with cells greater than 20x20, the error increases up to 10% (***Figure 5.1*****c**).
- Temporal discretization: a seven-day time step was chosen to preserve the seasonal operation pattern, but also to ensure a smooth computation. All the models were run for 5 years allowing to reach the stabilization of the seasonal recovery efficiency, but also avoiding the interferences that can be generated in the first years of operation of the system.
- Aquifer thermo-hydraulic parameters: a typical sandy aquifer has been simulated with parameters obtained from Beernink et al. 2024 (**Table 5.1**).

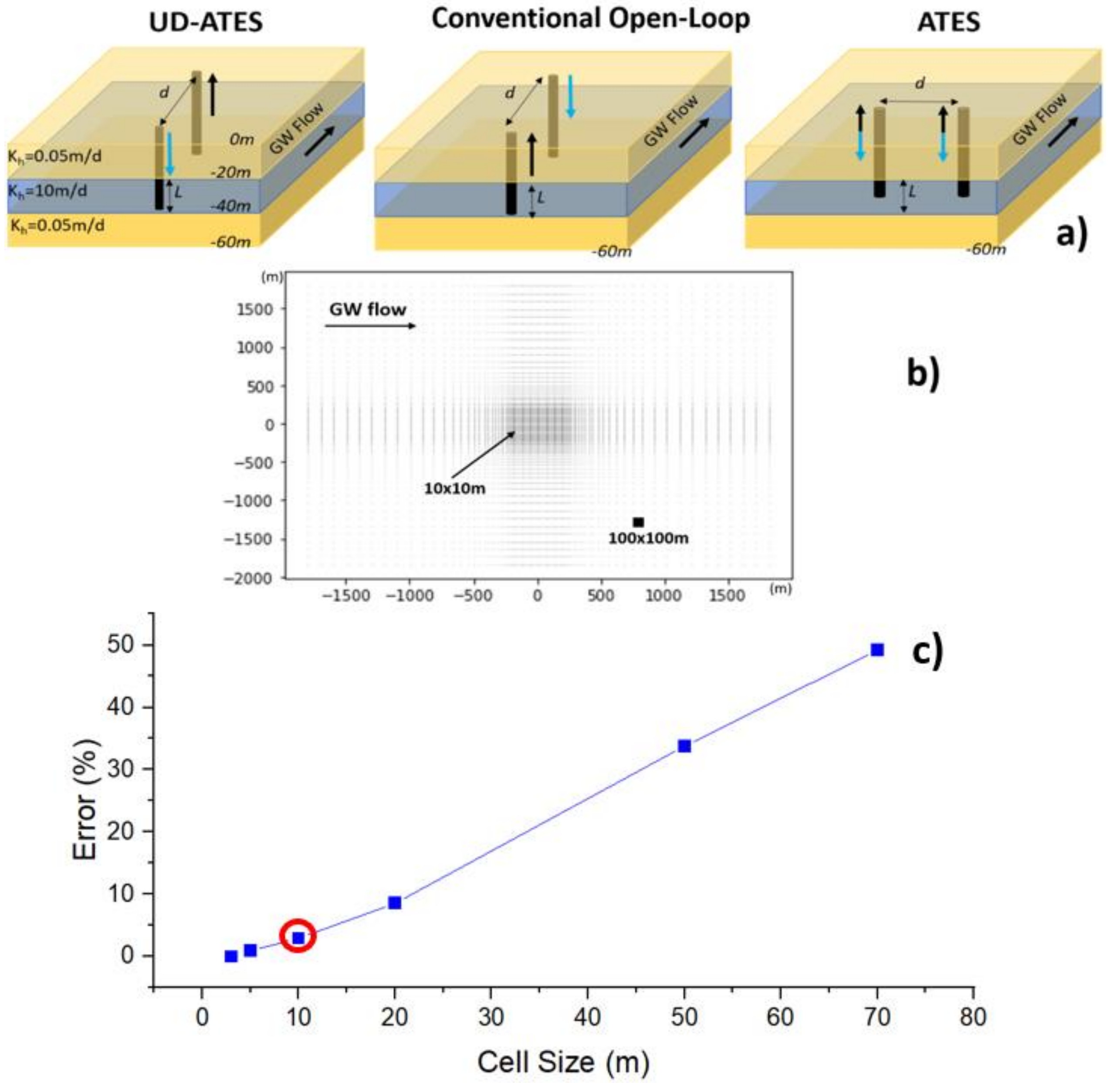

Figure 5.1 - Schematic representation of: a) the layers in the synthetic model of the three geothermal systems considered and b) the grid size in plan view. c) Increment of the output error for different cell sizes (the number is indicating the cell side), the red circle indicates the size selected for the model settings.

Table 5.1 - MODFLOW simulation parameters values (Beernink et al. 2024.).

Parameter	**Symbol**	**Value**
Aquifers' horizontal conductivity	K_h	10 m/d
Aquitards' horizontal conductivity	K_h^{aqt}	0.05 m/d
Porosity	n	0.3
Longitudinal dispersivity	α_l	0.5 m
Transversal dispersivity	α_t	0.05 m
Density of solid	ρ_s	2,640 Kg/m^3
Density of fluid	ρ_f	1,000 Kg/m^3
Bulk density	ρ	2148 Kg/m^3
Solid heat capacity	w_s	710 J/Kg °C
Fluid heat capacity	w_f	4183 J/Kg °C
Thermal conductivity of sand	k_s	2 W/m °C
Thermal conductivity of clay	k_c	1.7 W/m °C
Thermal conductivity of fluid	k_f	0.58 W/m °C
Thermal conductivity of the aquifer	k	1.57 W/m °C
Thermal conductivity of the aquitard	k^{aqt}	1.36 W/m °C
Effective molecular diffusion	α	$1.4 \cdot 10^{-11}$ m^2/day
Thermal distribution coefficient	λ	$1.7 \cdot 10^{-4}$ m^3/Kg

5.2 Simulation

5.2.1 Sensitivity analysis

A sensitivity analysis of the three parameters that greatly affect the efficiency of ATES systems was done, keeping the hydraulic conductivity, porosity and dispersivity constant for all the scenarios. In particular, the chosen parameters are the inter-well distance (*d*), the GW flow velocity (*u*), and the total storage volume (*V,* i.e. the total withdrawn or injected GW volume per season).

- The *d* was varied from 50 m to 350 m, an appropriate distance in an urban context or district scale (with steps of 25 m).
- For each *d*, different *u*, varying from 3 m/y up to 1,000 m/y, were simulated, similarly to Chae et al. 2020. Smaller steps were used at lower velocities and greater at higher velocities, resulting in the following range: 3-25-30-50-75-100-150-200-250-300-400-500-750-1,000 m/y. These values were obtained by changing the hydraulic gradient of the model since the hydraulic conductivity was kept constant in all the scenarios.
- The different *u* and *d* cases were simulated using three different scenarios of *V*: 100,000, 250,000 and 500,000 m^3/season, being representative of ATES sizes (Bloemendal and

Hartog, 2018). The storage volume (*V*) was distributed over time using a cosine function as shown in ***Figure 5.2***.

The wide variability of these parameters is representative of several ATES conditions making this model applicable to all the sites that present any GW flow velocity.

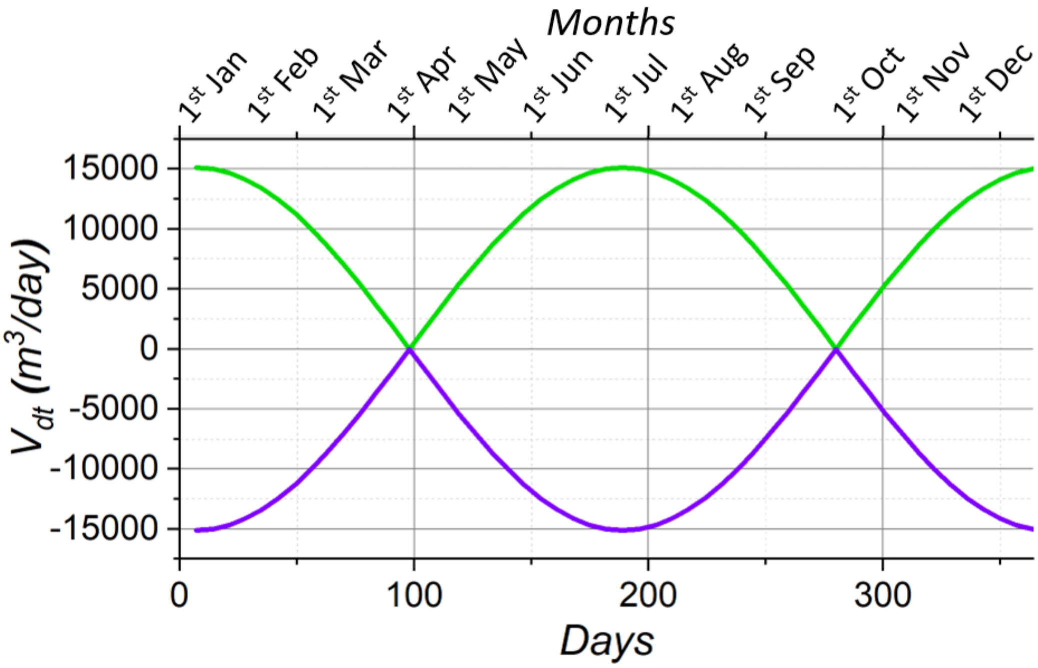

Figure 5.2 - Cosine distribution of the pumping rate (V_{dt}) for the upstream well (W0, injection) and the downstream well (W1, withdrawal) case, respectively.

The model configuration started by selecting appropriate values for *d*. By setting a *V* value of 250,000 m^3/season and no *u*. The inter-well distances (*d*) values from 25 to 500 m, with 25 m steps were used. First, the energy at each time step was obtained (**Figure 5.3**), and secondly, all energy values related to one of the two seasons of the fifth year were summed up.

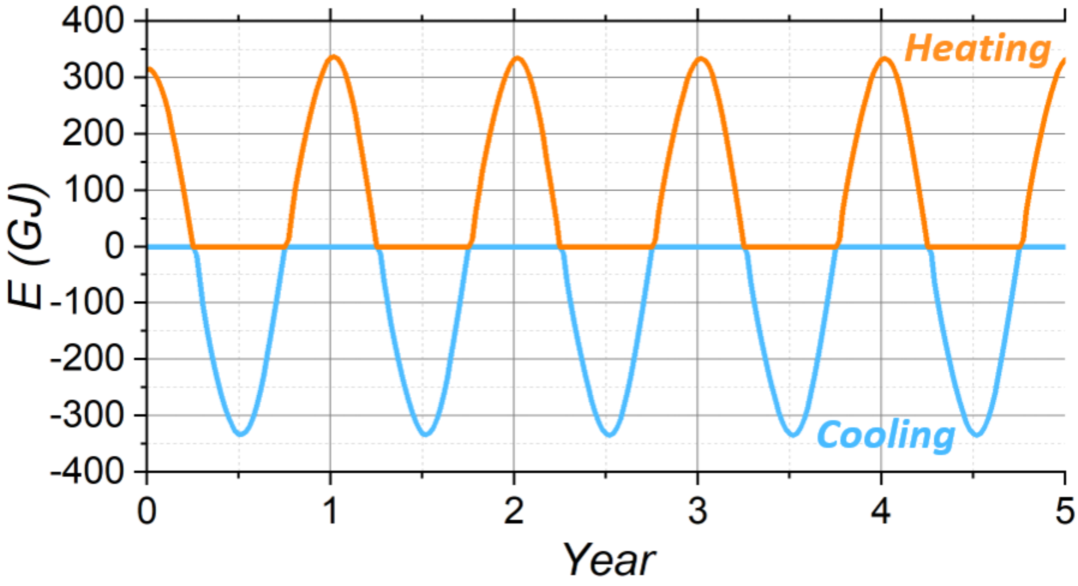

Figure 5.3 - Winter and summer distribution of energy during five years (example for a d of 150m).

5.2.2 UD-ATES, O-L and traditional ATES scenarios

The hydro-thermal solution results were generated for different scenarios (**Table 5.2**), including the uni-directional ATES (UD-ATES) system, where the pumping well lies downstream of the injection well, the conventional open-loop (O-L) scheme, in which the directions of pumping and injection directions of the two wells, was reversed, and the traditional ATES configuration, where the two wells were disposed transversely to the GW flow direction to avoid short circuit flows between the two wells at larger *u*.

Another difference in the model settings is represented by d. The efficiency for a given d depends on u and V parameters and was modified during the sensitivity analysis. Instead, for the traditional ATES and the O-L configurations *d* was set as the minimum value to avoid the short-circuiting effects between the two wells for all *u* considered, and it is just related to *V*.

Table 5.2 - Variability of the d according to V considered (minimum d to avoid the short circuiting effect).

	Inter-well distance ATES	**Inter-well distance O-L**	**Inter-well distance UD-ATES**
100,000 m^3/season	200 m	150 m	Variable according to *u*
250,000 m^3/season	250 m	200 m	Variable according to *u*
500,000 m^3/season	300 m	250 m	Variable according to *u*

5.3 Assessment framework

5.3.1 Thermal recovery efficiency

The energy extracted from the GW by the system was calculated for each time step by multiplying *V* by the specific heat capacity of water (c_w), by its density (ρ_w) and by the difference between the extraction (T_{ext}) and injection (T_{inj}) temperatures. Then, the seasonal energy (eq. 5.1) was obtained by integrating over the different seasons:

$$E_{season} = \int_{season\_start}^{season\_end} V_{dt} \cdot (T_{ext} - T_{in}) \cdot \rho_w \cdot c_w \cdot dt \qquad \text{(Eq. 5.1)}$$

Where V_{dt} is the volume extracted or injected for each time step, *T* is the injection/extraction temperature, *dt* is the time step, and c_w is the heat capacity of water.

Within the model, the total energy (E_{season}) was retrieved by summing up all the energy values for each time step (7 days), separately for the two different seasons (summer and winter). From this value, the thermal recovery efficiency percentage (η_{th}) (eq. 5.2) was computed by comparison with the maximum potential seasonal energy (E_{max}) that could be collected in one season for a fixed ΔT of 10°C. All the results will be evaluated in terms of η_{th}.

Both E_{season} and η_{th} were retrieved starting from the 5th year of simulation, assuming the average annual temperature downstream of the injection point to reach stationarity with only seasonal oscillations. This condition has been verified for all the scenarios evaluated in this work.

$$\eta_{th} = \frac{E_{season} \cdot 100}{E_{max}} \ [\%] \qquad \text{(Eq. 5.2)}$$

The results were then assessed based on *d* as a function of the theoretical thermal radius (R_{th}). The inter-well distance (*d*) divided by the thermal radius (d/R_{th}) parameter is a dimensionless ratio representing η_{th} for a defined thermal volume (the thermal energy volume stored in the aquifer by the system) in ATES configurations. The R_{th} (eq. 5.5) is also related to the hydraulic radius (R_h) which is defined (eq. 5.4) as the infiltrated volume discretized as a cylinder (Bloemendal & Hartog, 2017), and depends on the injected volume (V_{in}), the porosity (*n*), the water and aquifer heat capacity (c_w and c_{aq}) and their density (ρ_w and ρ_{aq})(eq. 5.3).

$$\rho_{aq} \cdot c_{aq} = n \cdot c_w \cdot \rho_w + (1-n) \cdot c_s \cdot \rho_s \qquad \text{(Eq. 5.3)}$$

$$R_h = \sqrt{\frac{V_{in}}{n \cdot \pi \cdot H}} \tag{Eq. 5.4}$$

$$R_{th} = \sqrt{\frac{c_w \cdot \rho_w \cdot V_{in}}{c_{aq} \cdot \rho_{aq} \cdot \pi \cdot H}} = \sqrt{\frac{n \cdot c_w \cdot \rho_w}{c_{aq} \cdot \rho_{aq}}} \cdot R_h \approx 0.66\, R_h \tag{Eq. 5.5}$$

Where c_s is the heat capacity of the solid, n is the porosity, and H is the aquifer screen length.

5.3.2 Downstream thermal pollution

The thermal downstream plume was estimated in representative scenarios for the three different geothermal systems considered. The temperature data were collected for each time step in each cell located along the axis of the two wells (for the traditional ATES case the temperature was evaluated on the axis of just one well).

5.4 Results

5.4.1 General analysis

In the following section, the results obtained from the uni-directional ATES (UD-ATES) simulations will be presented.

Figure 5.4 shows the recovered thermal energy, expressed as a ratio to the maximum total energy (i.e., η_{th}), for both winter and summer seasons across various inter-well distances (*d)* scenarios in the case with no and 500 m/y GW flow velocity (*u*).

- For the no GW flow simulation, when d/R_{th} is low, the thermal recovery efficiency (η_{th}) is low due to the thermal short-circuit occurring between the two wells. As *d* gradually increases, the energy output also grows due to the less short-circuit effect, peaking at approximately 125 m ($d/R_{th} = 1.62$). This peak can be attributed to the absence of short-circuit flows and the presence of warm/cold water injections from the preceding season. As *d* further increases, the energy diminishes once again. This drop results from a mismatch between the extraction temperature and the required temperature for heating or cooling the building until a stable value across greater distances is reached. The second minor peak (at $d/R_{th} = 2.3$) is caused by a favourable alignment between the extraction temperature and the system's required temperature, occurring after two season cycles. Beyond this value of d/R_{th}, the energy experiences a slight decrease, stabilizing at greater values of d/R_{th}. This stabilization occurs due to the absence of any remaining thermal interaction between the two wells. The reason why it stabilizes at 50% efficiency results from the ambient aquifer temperature, which is exactly between the warm and cold temperatures. Hence, η_{th} of 50% means that ambient GW is extracted, while η_{th} lower than 50% means that GW with unfavourable temperatures at a specific time is extracted, for example, if short-circuiting occurs.

- The results for the 500 m/y *u* scenario show that the peak is shifted to 175 m ($d/R_{th} = 2.27$) since the thermal plume is brought to further distances due to GW advection.

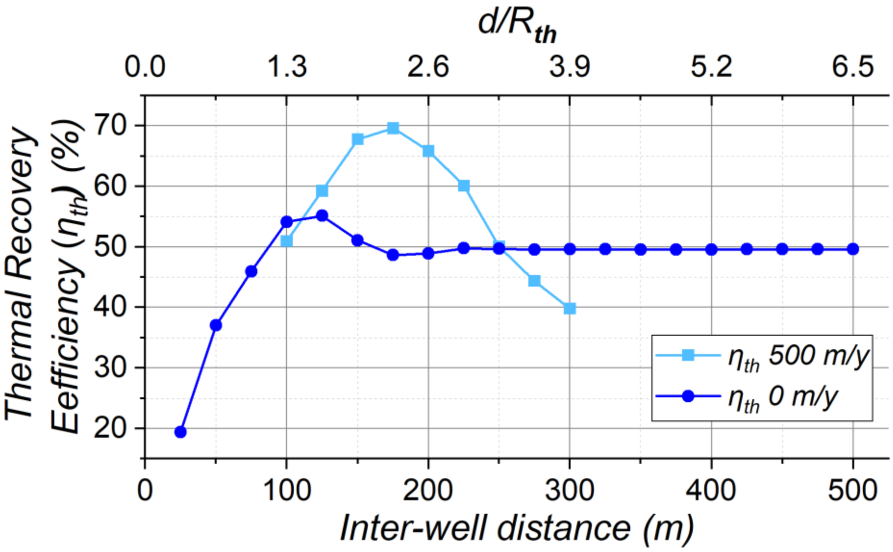

Figure 5.4 - Thermal recovery efficiency (η_{th}) curves for different d of the uni-directional ATES (UD-ATES) configuration for 0 m/y and 500 m/y of GW flow velocity (u) and a storage volume (V) of 250,000 m3/season in winter.

Figure 5.5 shows η_{th} as a function of *d* under different *u* for 100,000 m^3/season (Figure 6a), 250,000 m^3/season (Figure 6b), and 500,000 m^3/season (Figure 6c) *V*, respectively. All the scenarios were run up to *d* that is needed to obtain an optimum of efficiency.

The following observations can be made:

- Higher *V* directly correlates with higher energy recovery. This observation aligns with traditional ATES behaviour, where a larger volume corresponds to improved performance and minimized energy losses.
- Higher *u* requires a larger *d* to obtain optimal recovery rates. This is explained by the fact that the plume is transported at further distances throughout each seasonal cycle. On the

other hand, at lower *d*, η_{th} is lower for greater *u*, since as the velocity increases the short circuit flow between the two wells gets stronger.

- At 100,000 m^3/season *V* (Figure 6a), the optimal values remain relatively constant (almost 70%) for *u* larger than 400 m/y. However, at 250,000 m^3/season and 500,000 m^3/season *V* the efficiency exhibits an upward trend (65% to 75% in both cases) for higher *u*, meaning that even higher efficiency may be reached at greater *u*. This variation according to the different *V* depends on the fact that the energy is dispersed more rapidly by high *u* with low *V* compared to scenarios with greater volumes; for this reason, in the case of 100,000 m^3/season, the efficiency does not exceed 70%.
- Since the maximum efficiency is not close to 100%, it seems impossible to capture all the thermal energy injected from the upstream well. This is caused by the intermitted warming-up and cooling down of the confining layers. Therefore, in every cycle, there are relatively large losses to the layers above and below. Also, dispersion and mixing of warm and cold injected water, as well as the mixing with the GW at natural ambient temperature, results in losses.
- All the scenarios located under the 50% line are representative of a negative short-circuitation effect between the two wells, which results in a strong reduction of η_{th}.
- Furthermore, the optimal distances corresponding to each *u* in the three *V* considered showed that are not located at the same value of d/R_{th}, but they are shifted towards lower values of d/R_{th} and higher values of *d* for increasing *V*.

The general concept of recapturing a major part of the injected heat with a downstream well proves to be feasible from these simulation results.

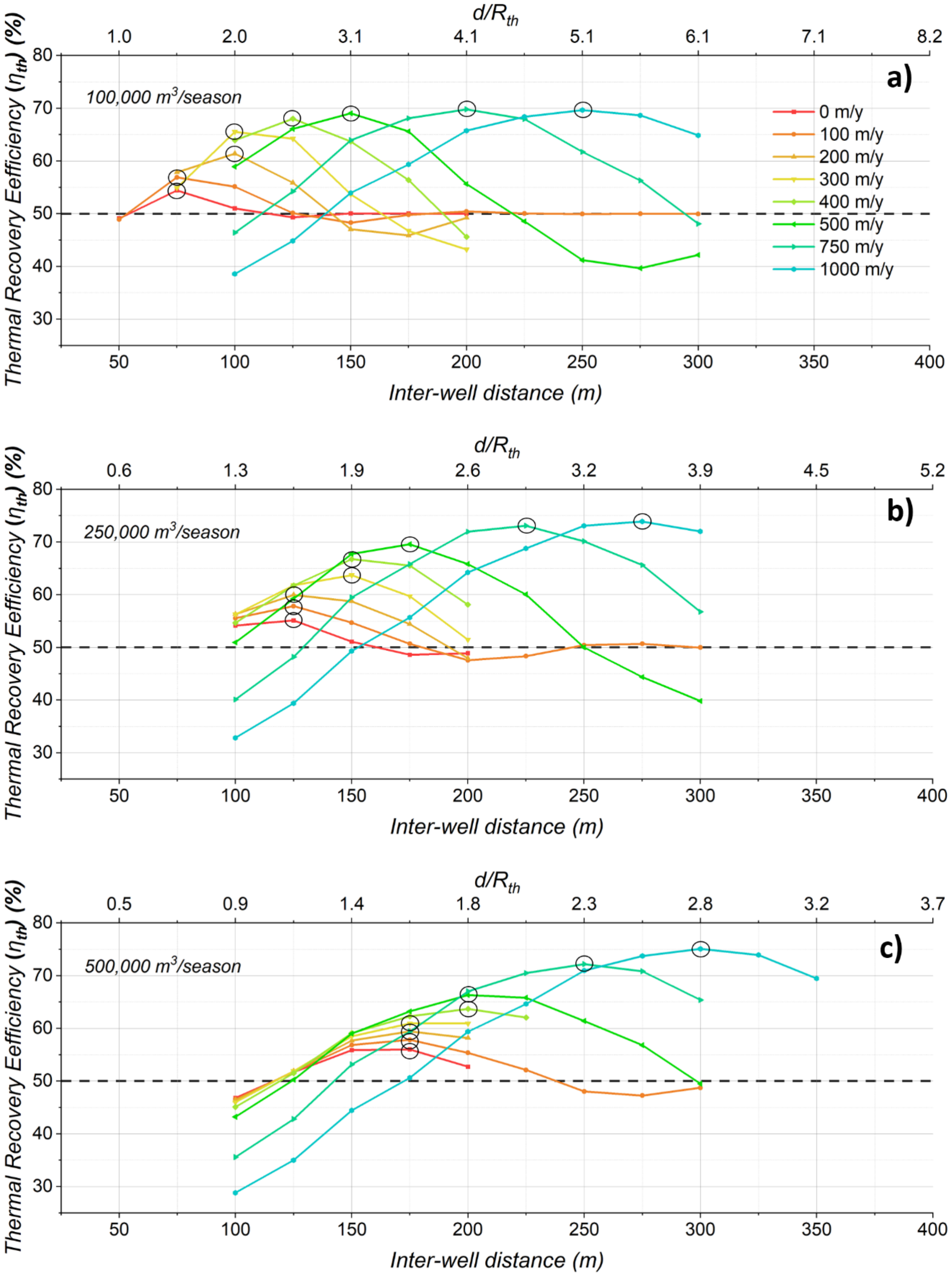

Figure 5.5 - Thermal recovery efficiency (η_{th}) as a function of the inter-well distance (d) for different GW flow velocities (u) and different scenarios of storage volumes (V): a) 100,000 m3/season, b) 250,000 m3/season, c) 500,000 m3/season. The upper axes report the ratio between the inter-well distance and the thermal radius (d/R_{th}) and changes for the three plots since R_{th} is a function of the storage volume (V). The optimum are depicted with a black circle. The dashed line represents the thermal recovery efficiency (η_{th}) of a conventional open-loop (O-L) system.

5.4.2 Comparison between ATES and conventional open-loop systems

The model results of the UD-ATES system were compared to the other systems by extracting the optimum η_{th} at the different u and V. For the traditional ATES and the O-L configuration, the d was varied according to the different V considered, but was kept constant for all the u, since d does not affect η_{th} (**Table 5.2**).

Figure 5.6 shows the most efficient system at different u. The O-L system has a constant η_{th} (50%) in all the scenarios since there are no variations between the extraction and injection temperatures. The η_{th} of both the ATES systems considered, increases at greater V. At small u, the traditional ATES systems perform better, but as the GW flow velocities increase the UD-ATES outperforms the traditional ATES system. The threshold value between the UD-ATES and the traditional ATES shifts towards higher u with increasing V, passing from 220 m/y for the smallest V, to 320 m/y for 250,000 m^3/season, up to 400 m/y for the greatest V. This might be explained by the fact that the higher the V, the greater the chances that the traditional ATES extracts back the thermal plume injected in the previous season.

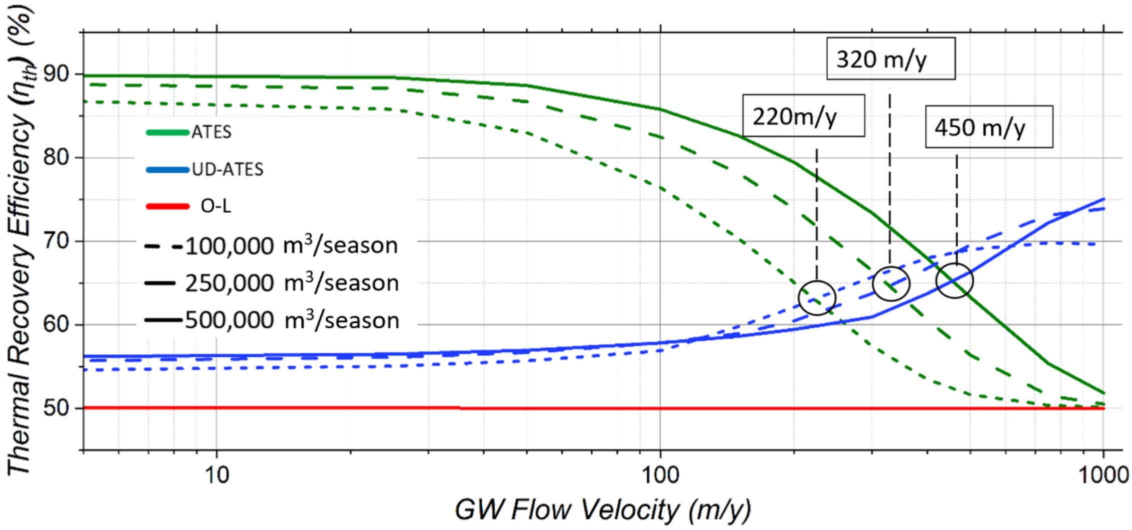

Figure 5.6 - Comparison of the thermal recovery efficiency (η_{th}) versus the GW flow velocity (u) for the three different geothermal systems considered for the three storage volume (V) scenarios. The efficiency remains constant for the conventional open-loop (O-L) system, but it shows a variation in the other systems with increased GW flow velocity (u). The black circles identify the trade-off values for which the uni-directional (UD-ATES) becomes more convenient than the traditional ATES.

5.4.3 Downstream thermal pollution

The thermal plume generated by the three systems considered was analysed, for the specific case of 100,000 m^3/season storage volume, and for a GW velocity of 500m/y, to understand how and at which distance GW users located downstream could be affected.

Figure 5.7 shows the temperature variation along the flow direction for all the time steps modelled in the fifth year of operation when the temperature is stabilized. The lines going from blue to red indicate the increasing number of weeks from the 1st of January to the 31st of December.

For the O-L (Figure 8a) the inter-well distance considered was 150 meters. The temperature (ΔT) is ± 0.5°C at 80 m from the downstream (injection) well, and ± 0.25°C at 130 m. For the UD-ATES system (Figure 8b) the inter-well distance was kept at 150 meters. The ΔT at the downstream (extraction) well is lower than ± 0.5°C and decreases to ± 0.25°C at 15 m from it. For the traditional ATES scenario (Figure 8c) the inter-well distance was set at 200 meters, in this case, the distance was calculated downstream of the cold well (because the two wells were not disposed on the longitudinal direction of the GW flow, but transversely).

The temperature variation in this case indicates that the ΔT is ± 0.5°C at 345 m, and decreases to ± 0.25°C at 375 m. Even though the injected volume is half compared to the other two cases (since the cold well was considered, only), such a long thermal plume can be explained by the lack of thermal counterbalance during the injection of hot water from the same well. Needs to be noted that the inter-well distance considered for the conventional O-L and the traditional ATES configurations was set to avoid the short-circuit flow between the two wells, while for the UD-ATES was set to maximise the thermal recovery efficiency according to the GW flow velocity (as stated in **Table 5.2**).

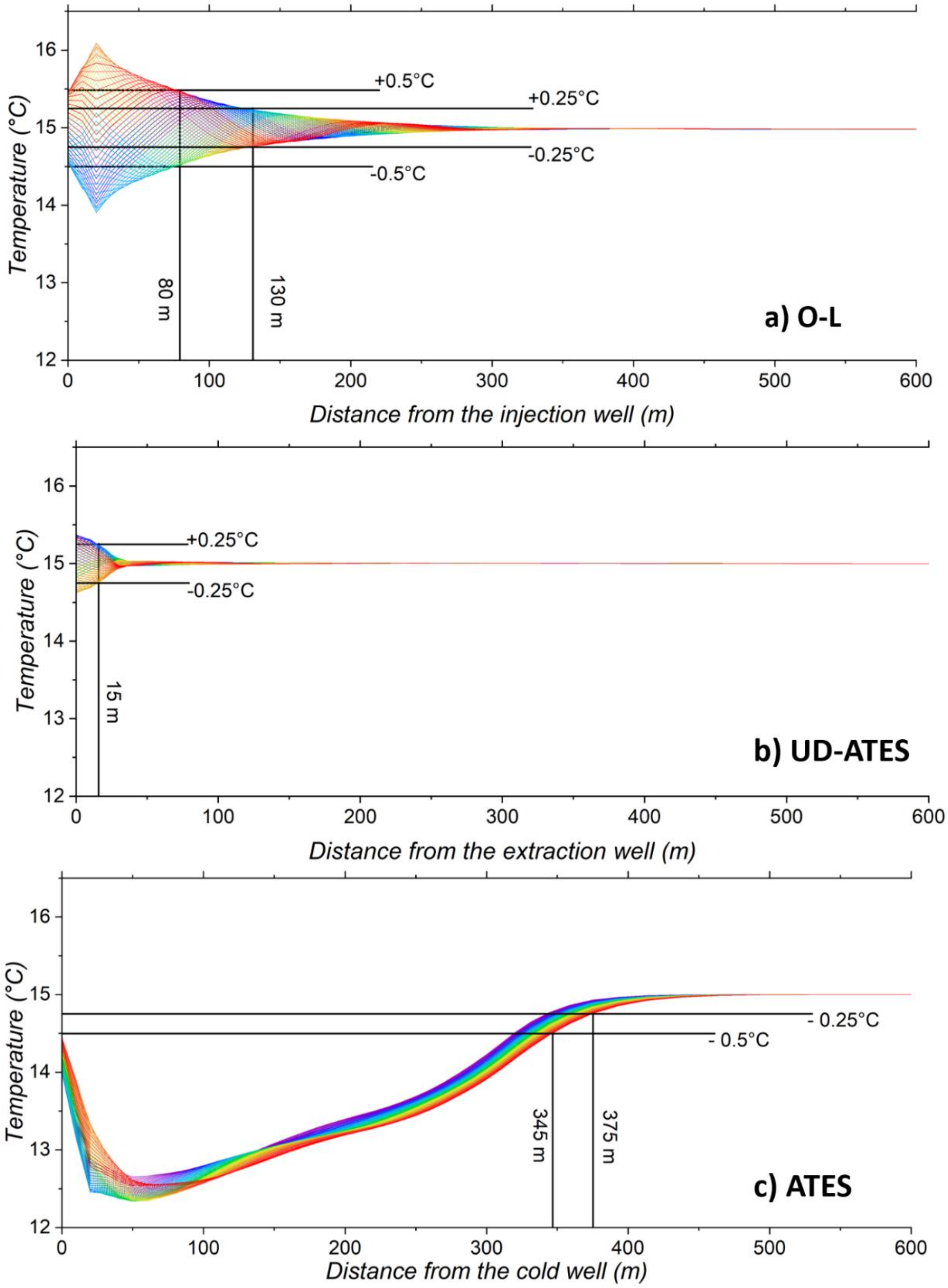

Figure 5.7 - Temperature variation downstream of the system, during the fifth year of operation, for a GW flow velocity (u) of 300 m/y and a storage volume (V) of 100,000 m^3/season: a) conventional open-loop (O-L) system with inter-well distance (d) of 150 m; b) UD-ATES system with inter-well distance (d) of 110 m; c) traditional ATES system with inter-well distance (d) of 200 m. For the traditional ATES, the temperature downstream is reported for the cold well, and would be specular for the warm well. Each coloured line represents a time step of the analysis (1 week) increasing from blue to red. The distances at the isotherm lines of ±0.5°C and ± 0.25°C are marked with black vertical lines.

Another visualisation of the thermal plume generated by the three different geothermal systems configurations considered in this study is shown in **Figure 5.8**. The illustration depicts the temperature distribution within the aquifer for the entire domain at selected time intervals. The time steps were chosen to provide representative insights; the first is at half of the first simulated year (coinciding with the seasonal transition) and followed by intervals of one and a half years, extending to the final simulated time step.

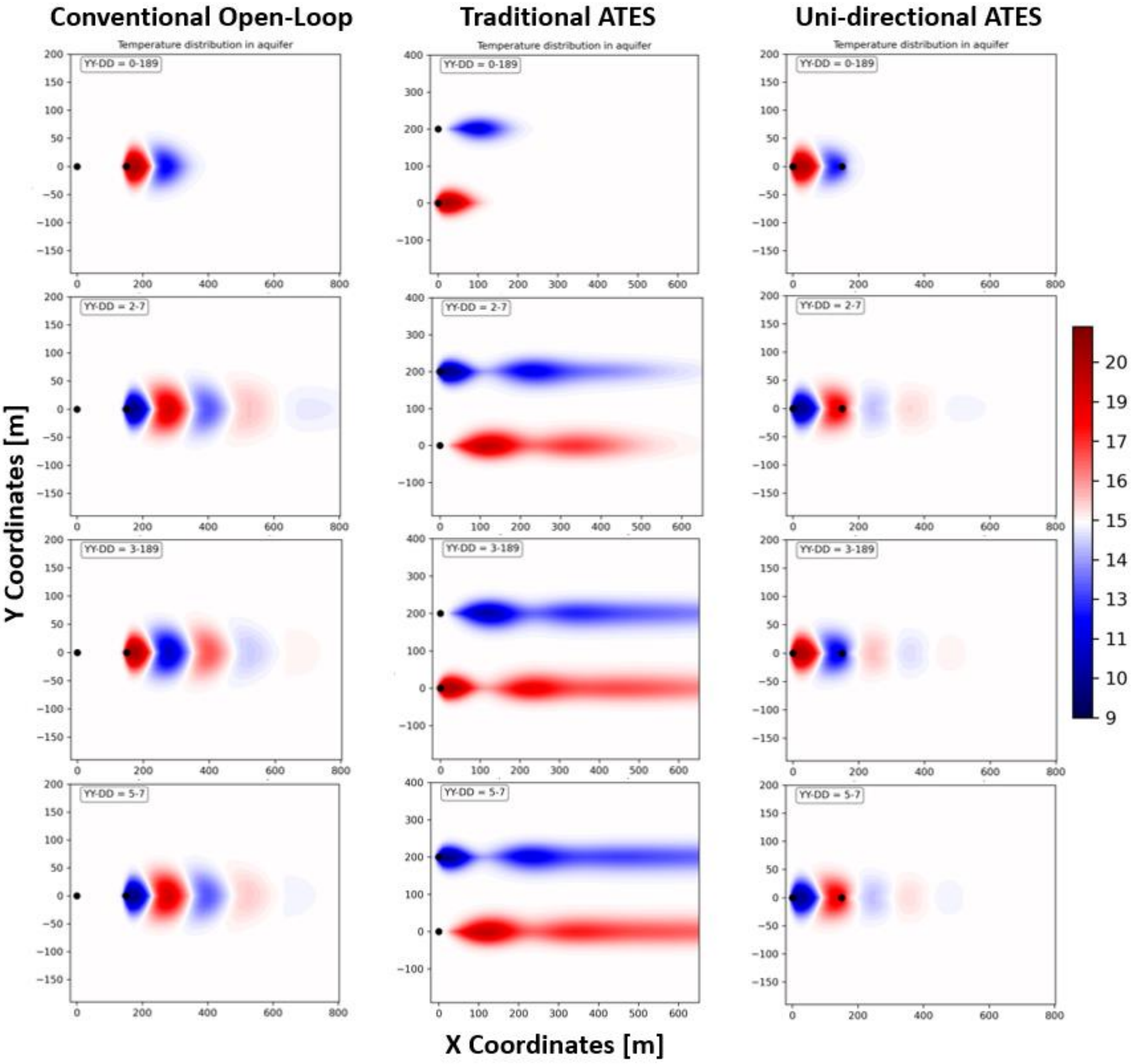

Figure 5.8 – Temperature distribution in the aquifer's domain for the three geothermal systems configurations considered at specific time steps. The annotation "YY-DD" in the top left corner of each illustration indicates the corresponding year and day of the simulation. The outputs were generated from the specific storage volume of 100,000 m3/season and a groundwater velocity of 500 m/y. For the uni-directional and traditional ATES scenarios, the inter-well distance was set at 150 meters, whereas for the open-loop system, it was 200 meters.

5.5 Discussions

The thermal recovery efficiency (η_{th}) of traditional ATES systems is known to be reduced with increasing the GW flow velocity (*u*). The heat loss due to dispersion is larger at high velocities since the heat is being transported away from the production well, thus reducing the stored heat available for the following season (Bloemendal & Olsthoorn, 2018). In the worst case of a very fast GW flow velocity (> 750 m/y), the efficiency of the ATES systems is reduced to 50%, equal to a conventional O-L system (**Figure 5.6**). This research demonstrates that, above a certain *u*, a uni-directional ATES (UD-ATES) configuration can be a worthwhile alternative able to reuse part of the energy extracted or injected into the aquifer during the previous season. In the ideal case of symmetrical heating and cooling demand, the UD-ATES can reach a η_{th} as high as 75%, much larger than the O-L systems.

The *u* threshold above which the UD-ATES system outperforms the traditional ATES systems shows a dependence on the storage volume (*V)*, which in turn depends on the annual pumping rate: the larger the *V*, the higher the *u* thresholds. This is due to the following reasons: firstly, the larger the *V*, the more efficient the traditional ATES systems will be, where a larger *V* corresponds to improved performance and minimised energy losses; on the contrary, the UD-ATES, at lower *u,* suffers from large values of *V* due to the higher degree of possible interference caused by a large extension of the thermal plume. Meanwhile, greater values of *V* result in higher values of well discharge, causing higher interference between the wells.

This research also demonstrates that the extent and intensity of the thermal plume is extremely reduced by using UD-ATES in optimal inter-well distance (*d)* conditions and assuming a symmetrical heating and cooling demand. In the example shown in **Figure 5.7**, the thermal plume length is reduced by approximately one order of magnitude compared to the other systems. This positive effect of UD-ATES on the thermal plume has been observed also for the other *u* and *V* values.

The main lack of this study is the assumption of equal heating and cooling loads for summer and winter seasons, in order to maximize η_{th} of the system. However, the actual heating and cooling load of an end-user would vary throughout the year, with possible imbalances between the energy demand in summer and winter, resulting in lower η_{th}. Moreover, this imbalance could also affect the long-term sustainability of these systems. Therefore, further study is needed to assess the feasibility of UD-ATES systems compared to other configurations under different energy demand scenarios, e.g., in different climatic zones.

In the following paragraphs will be discussed relevant aspects related to the operability of UD-ATES.

5.5.1 Effects of aquifer thickness and thermal diffusivity

The aquifer thickness (*H*) and the mechanical dispersivity (α_l) were not formally included in the sensitivity analysis. However, the effect of the variation of these two parameters on *d* and η_{th} was analysed for a specific *V* (100,000 m^3/season) and moderately low and high *u* (100 and 500 m/y).

Different scenarios with 10-20-30-40-50 m thick aquifers were tested. Generally, it was observed that independent of *u*, the optimal *d* decreases with greater values of *H* (**Figure 5.9a**), while minimal variations in η_{th} are observed (**Figure 5.9b**). This could be related to the different horizontal/vertical shape ratio of the thermal plume, e.g., expressed by the thermal radius of Equation 5. Additionally, there is slight evidence that for different *u*, there is an optimal aquifer thickness giving a maximal value of η_{th}.

The longitudinal dispersivity, α_l, tested in the different scenarios run was 0.1-0.5-1-5-10-50 m, whereas the transversal dispersivity was always set at one order of magnitude less than the longitudinal one. Different values of dispersivity cause variations in the extent and the temperature field inside the thermal plume. This leads to losses in η_{th} for higher values of α_l, with a stronger effect for greater flow velocity (**Figure 5.9d**). Due to the thinning of the temperature profile along with the thermal plume, for higher values of α_l, *d* tends to a common value for different values of *u* (**Figure 5.9c**).

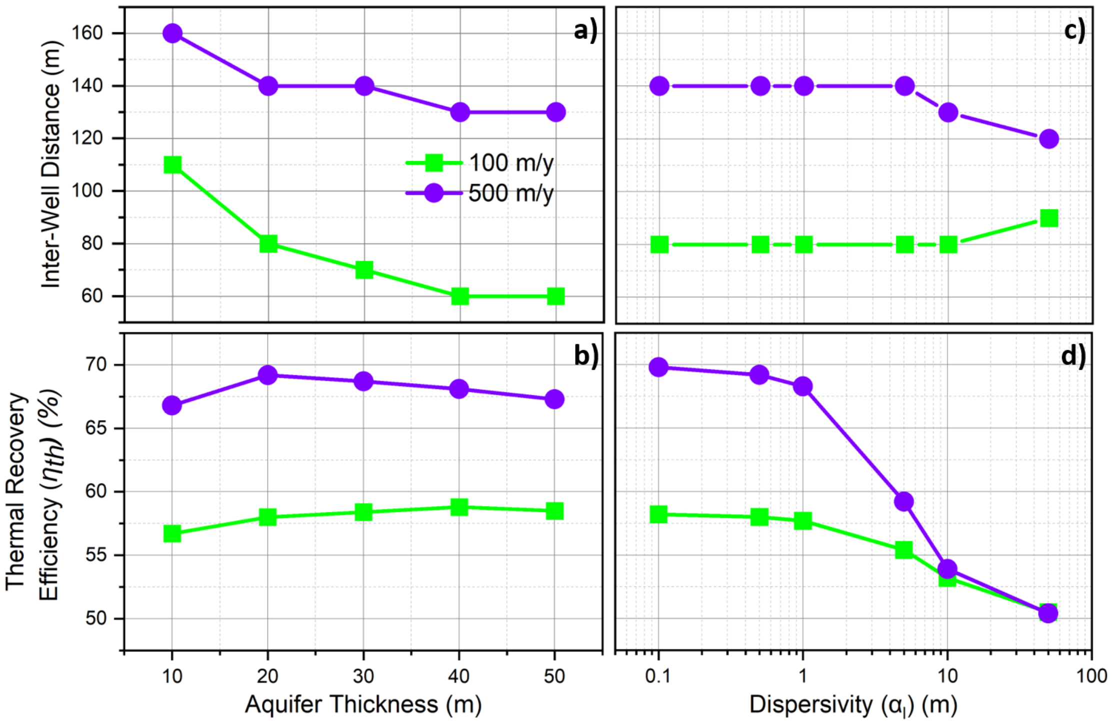

Figure 5.9 - a-b) Aquifer thickness (H) vs inter-well distance (d) and thermal recovery efficiency (η_{th}), respectively. c-d) Longitudinal dispersivity (α_l) vs inter-well distance (d) and thermal recovery efficiency (η_{th}), respectively.

5.5.2 Effects of natural variability of GW flow velocity and direction

To configure and build UD-ATES systems, a thorough understanding of the GW flow direction and u in the aquifer used as storage is important. Once a UD-ATES is designed, and the *d* fixed, a natural variation of *u* or direction can affect the system's performance. The effect of GW flow *u* and direction on η_{th} of UD-ATES was quantified by modelling different scenarios considering a fixed *V* of 100,000 m^3/season, a *d* of 110 m, and a *u* of 300 m/y. By reducing the *u* by 5%, 10% and 15%, the η_{th} dropped by 0.7%, 1.5% and 2.5% respectively. At the same time, modifying the GW flow direction by 5°, 10° and 15° from the longitudinal direction of the two wells in respect to the GW flow direction reduces the η_{th} by 0.2%, 1.0% and 2.6%, respectively.

These scenarios demonstrate that a good knowledge of the GW flow direction and *u* is imperative to establish the best position and *d* of the doublets, which allows to obtain the maximal η_{th} from the system.

The best way to estimate the GW flow u and direction is to perform direct measurements through a long-term monitoring, to characterise their variations over time. In this way, it would be possible to test the model within the entire range of variability of these parameters and to evaluate how much η_{th} could change in specific periods, reducing the operation risks.

5.5.3 Effects of energy imbalance between the two season

In order to obtain the maximum η_{th}, all of the simulations conducted during this study were perfectly balanced in terms of the volume extracted in the two seasons, as well as for the energy produced, since the delta temperature of extraction and injection remained unchanged.

This section will demonstrate how the imbalance in the extracted volume between the two seasons affects the η_{th} of a traditional ATES geothermal system. As was illustrated in **Figure 5.6** in chapter 5.4.2 the threshold value of u for which a traditional ATES configuration is more advantageous than a uni-directional ATES for the minimum V considered (100,000 m^3/season) is 220 m/y. Given that the estimated value of u in most of the city of Milan is less than 200 m/y (as will be presented in the next chapter, in section 6.3), the most appropriate solution would be to install traditional ATES configurations. Consequently, the impact of energy imbalance on the η_{th} was investigated.

The municipality of Milan is densely populated with conventional open-loop geothermal systems; therefore, this study seeks to demonstrate the potential for enhanced efficiency gains through the conversion of conventional open-loop systems into traditional or uni-directional ATES configurations.

The imbalance imposed on the simulation was achieved by progressively decreasing the extracted and injected V (i.e. 10%, 20%, 30%, and so on) in one of the two seasons while maintaining the V of the other season at its maximum (100%).

Figure 5.10 shows the η_{th} for both summer and winter conditions (on the X-axis) in different scenarios of energetic imbalance (on the Y-axis) for both seasons. The graph highlights that in perfectly balanced (100%) conditions the η_{th} tends to a homogenous value in both seasons, while the greater the energetic imbalance (0%), the higher the disproportion between the values of η_{th} in summer or winter will be.

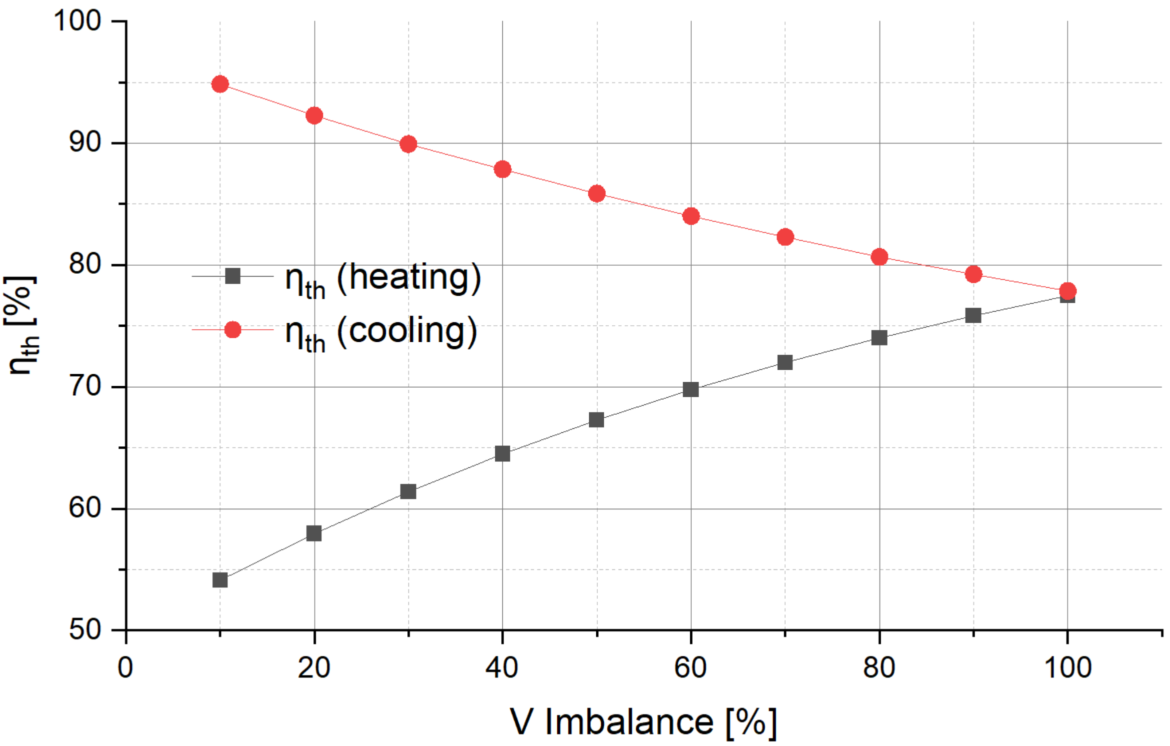

Figure 5.10 – Thermal recovery efficiency (η_{th}) for both summer and winter conditions in different scenarios of energetic imbalance for a traditional ATES geothermal system.

With this information was also generated **Figure 5.11**, which shows the gradual increment of efficiency with the decrement of the imbalance compared to a conventional O-L system. The graph demonstrates that also in the worst imbalanced conditions between the two seasons (10% and 100%), the η_{th} increment compared to a conventional O-L is greater than 15%.

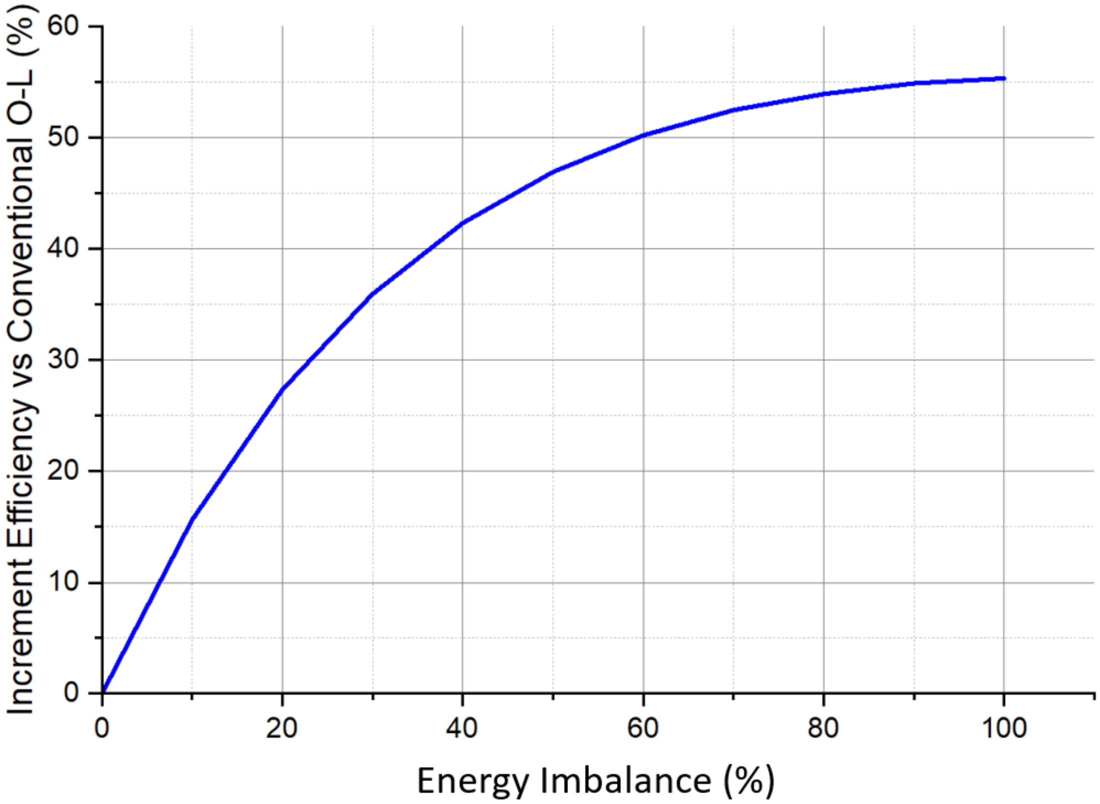

Figure 5.11 – Relation between the energy imbalances of a traditional ATES system with the increment of thermal recovery efficiency (η_{th}) compared to a conventional open-loop (O-L) system.

5.5.4 Cost comparison

Furthermore, in a dense urban setting, such as metropolitan cities, several geometric constraints may also hamper the installation of wells at the optimal required spacing and orientation to obtain the maximum η_{th} from the system. It is important to run several numerical models to evaluate the most suitable d and direction according to the geometrical constraints, in order to establish which system could be the most efficient. The need for a detailed characterization of the aquifer, which is mandatory to optimize the efficiency of the system, can lead to higher capital expenditure (CAPEX) compared to O-L and traditional ATES. However, the paper shows that an optimal configuration of the UD-ATES system in high u velocity aquifers can be 13 to 25% more efficient compared to O-L system. This higher efficiency translates into a reduction in the energy required to extract and inject water, resulting in lower operating costs (OPEX) for the system. In the long term, this should compensate for the higher CAPEX. Furthermore, greater efficiency results in lower storage volume. In this way, it might be possible to decrease the number of wells needed for system operation, reducing the relative cost. In particular, the UD-ATES system seems promising in regions with high u, such as in the Po plain of northern Italy. More generally, regions with high aquifer productivity (e.g. Sprenger et al. 2017) are all suitable for ATES systems (either traditional or uni-directional). In any case, it is important to assess the local hydraulic gradient to decide which system is best.

5.5.5 National regulation

Traditional ATES systems are installed worldwide (Sweden, Belgium, Denmark, and the USA), but more than 90% of them are operating in the Netherlands (Hoekstra et al., 2020). This is because the aquifers in this country are characterized by low GW flow velocity due to the strong presence of fine sandy layers and gradients close to 0%. In many other locations, except for these countries, there are not yet any regulations for ATES systems, because O-L configurations are more popular and widely used. In the most populated Italian Region (Lombardy), for instance, there is currently no legislation to regulate the adoption of ATES systems. In this region, the regulation (Regione Lombardia, 2017) states that the temperature difference between the extraction and injection wells must be lower than 5°C, not allowing the operation of a well doublet with an ATES configuration. Therefore, to promote this technology we propose to consider a maximal threshold value of temperature difference concerning the natural ambient temperature of the GW.

5.6 Summary

This study investigated the behaviour of UD-ATES systems, a concept of ATES that uses GW flow to store and recover thermal energy. The study performed a sensitivity analysis of the UD-ATES system for different conditions of inter-well distance (d), GW flow velocity (u), and storage volume (V). The study also compared the UD-ATES system with other ATES/open-loop systems, such as traditional ATES and O-L systems, in terms of thermal recovery efficiency (η_{th}), temperature variation, and downstream thermal plume. The study demonstrates that the UD-ATES system is feasible, especially for high u, as it can retrieve a major part of the thermal energy stored in the aquifer by a downstream well, despite heat losses due to GW flow. Recovery by a downstream well is controlled by choosing an appropriate d, depending on the V and the u.

The UD-ATES system can increase the efficiency of the thermal energy storage at high u, contrary to O-L systems, which is not capable of storing heat. The UD-ATES system can be from 16 to 25% more

efficient for *u* greater than 500 m/y, while traditional ATES can be from 18 to 40% more efficient for *u* lower than 400 m/y.
Examining the case of 100,000 m^3/season at *u* lower than 220 m/y, the traditional ATES system is more efficient, while for greater values, the UD-ATES is more convenient. This threshold value shifts to greater *u* according to which *V* is considered.
Moreover, the UD-ATES system can reduce the temperature variation and the downstream thermal plume, compared to O-L systems. The thermal plume of an O-L system can be up to 6 times longer than the one generated by a UD-ATES configuration under the same conditions.

Hence, the UD-ATES system can achieve two goals simultaneously: increasing the efficiency of the thermal energy storage wells and reducing the thermal pollution downstream, to avoid undesirable interactions between different systems located upstream and downstream.

The limitations and challenges of a UD-ATES system are the risk of short-circuit flow, which could reduce the η_{th} below 50%, and the effect of uncertainties and variations in well placement options, GW flow direction and *u*, and heating and cooling load. The study contributes to the development of a new ATES concept that can improve the performance and sustainability of O-L systems, by providing insights and guidelines for the design and operation of UD-ATES systems. Future research should focus on validating the UD-ATES model with field data and exploring the potential of UD-ATES systems for different applications and scenarios.

6. Integration of existing databases and regional scale modelling of geothermal plants

This section of the project was developed under a collaboration agreement between MUSA (Multilayered Urban Sustainability Action), MCM (Metropolitan City of Milan), and MoM (Municipality of Milan). This collaboration was established in response to the elevated GW (groundwater) temperatures observed in the shallow aquifer, particularly in the central regions of the city. This phenomenon can be attributed to the significant geothermal exploitation and the SUHI (Sub-Urban Heat Island) effect, but also for the increasing GW temperature related to climate change (CC) (Menberg et al., 2014). Therefore, the local public authorities (MCM and MoM) approached MUSA to address the problem and identify a solution. The main issues raised by the public authorities were disputes between private users of geothermal systems about the higher costs they had to bear compared to the projected costs assumed while sizing the plant. This is likely due to the fact that the authorities do not have a geodatabase to monitor and evaluate the permits for the construction of new systems, which could lead to the installation of several plants too close to each other, creating a short-circuit flow that reduces its efficiency, increasing the operating costs (OPEX).

6.1 Digitalization of the authorisation for existing geothermal systems

As a first step, MCM shared 1069 reports for the construction of shallow geothermal systems in the MCM, 556 of them located in the MoM and represented the data source for the numerical model. Each permit was related to a specific shared folder, which contained several documents such as the technical report, the hydrogeological report, and the well's reports. The scope of looking through all the shared permits was the creation of a database, which would gather information related to all the technical aspects of the geothermal systems designed. **Table 6.1** shows all the parameters collected during the digitalisation process.

Table 6.1 - Parameters collected for the creation of the database

Digitalized Parameter	**Measuring Unit**
File number	-
Geothermal wells testing date	-
Wells' coordinates	-
Wells' topographic altitude (Z)	-
Number of extraction wells	-
Number of injection wells	-
Well's depth	m
Well's radius	m
Filter's depth	m

Buildings volume splayed	m^3
Number of operative months	-
Yearly operative hours (cooling/heating)	-
Total annual flow rate (cooling/heating)	m^3/y
Energy (cooling/heating)	kWh
COP - EER	-
Peak flow rate	m^3/s
Power (cooling/heating)	kW
Delta temperature (cooling/heating)	°C
Average monthly discharge (cooling/heating)	m^3/s
Energy produced for each month (cooling/heating)	kWh

Once the data were all gathered into a database, post-processing was performed to recognise possible mistakes made during the copying procedure mostly in terms of coordinates misplacing or pumped volume. For the scope of this thesis, the data collected were used to evaluate the potential increment in efficiency in case conventional open-loop (O-L) geothermal systems (like most of the plants in MoM) would be reconverted into traditional or uni-directional Aquifer Thermal Energy Storage (ATES or UD-ATES, respectively) configurations.

6.2 Statistical analysis of the collected parameters

Several aspects were statistically analysed to evaluate data distribution across various parameters. The number of geothermal systems included in the analysis varied depending on the availability of information obtained through the digitalization process. This variation arose because, certain geothermal systems lacked specific data that were available in others, while in a few cases, complete datasets were present. This section provides frequency bar charts and maps illustrating the spatial distribution of the data within the MCM.

The total energy output for both the summer and winter seasons was analysed. **Figure 6.1a** illustrates that the majority of geothermal systems are concentrated in the city centre, gradually diminishing towards the peripheral areas of the city. The frequency bar chart in **Figure 6.1b** demonstrates a bimodal Gaussian distribution, with peaks observed for medium-sized geothermal systems (200 – 1,000 MWh of energy production) and medium-to-large-sized systems (2,000 – 10,000 MWh of energy production).

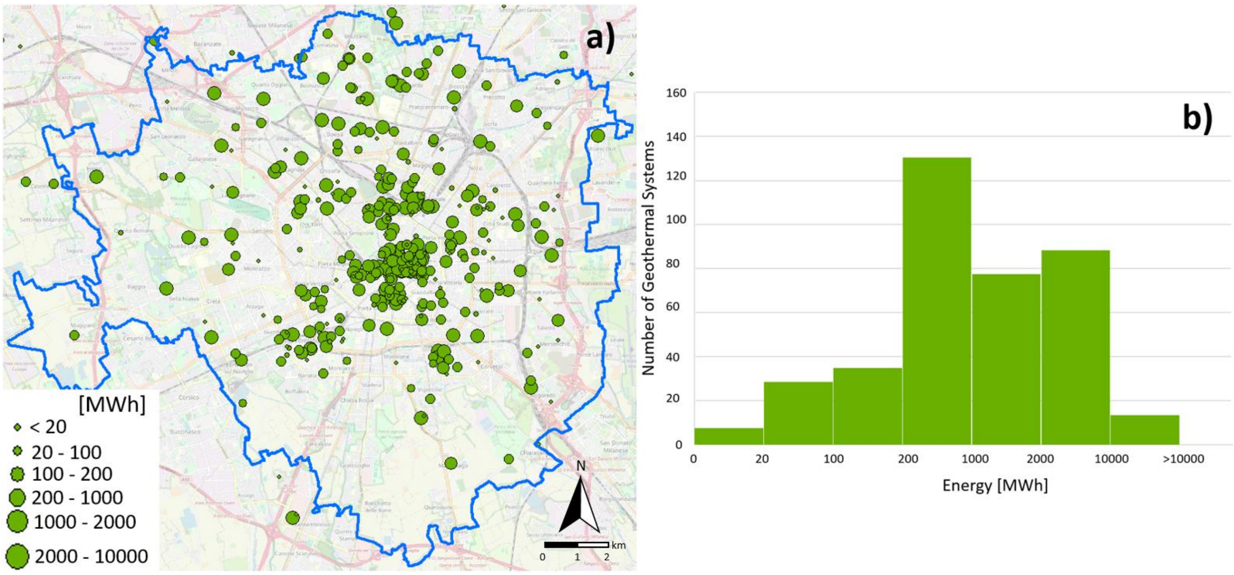

Figure 6.1 – a) Spatial distribution of centroids for geothermal systems within the metropolitan area of Milan. The size of the green dots corresponds to the scale of the total energy produced (in both seasons) for each geothermal plant, providing a visual representation of their relative dimensions. b) Frequency bar plot highlighting the presence of a bimodal Gaussian distribution characterizing the total energy produced by the geothermal systems.

Figure 6.1 was analysed to examine the distribution of energy generated during the winter and summer seasons, corresponding to heating and cooling, respectively.

Figure 6.2a illustrates the spatial distribution of geothermal systems that produce energy for cooling. **Figure 6.2b** presents a frequency bar plot corresponding to the data in the map. These two figures demonstrate a strong alignment with the patterns observed in **Figure 6.1**. It is important to note that geothermal systems not generating energy during the summer season were excluded from this analysis.

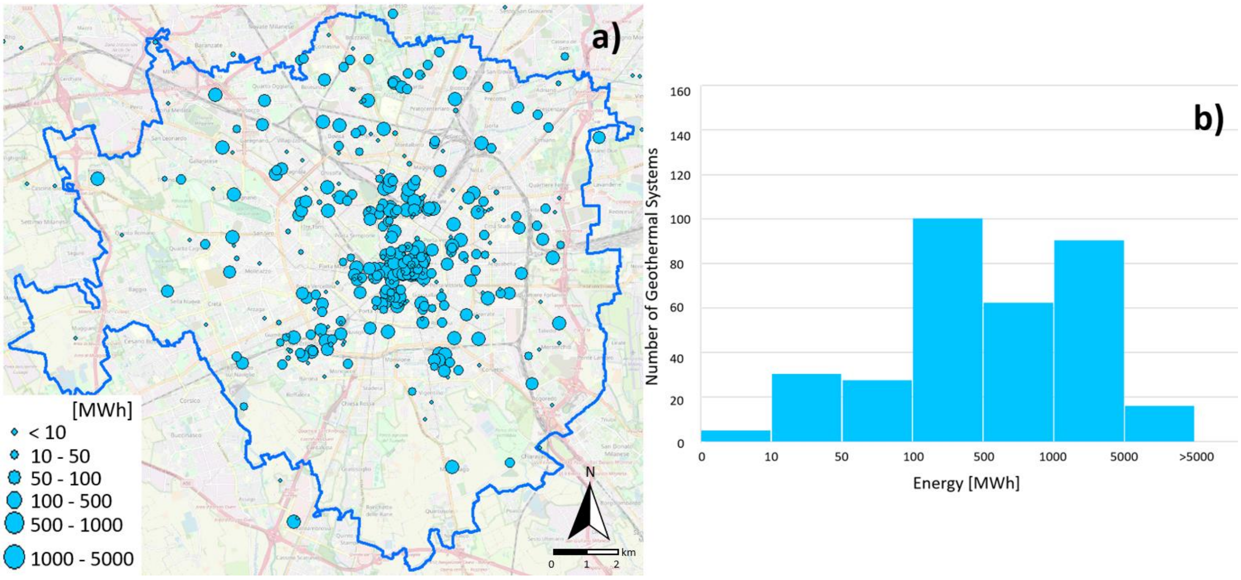

Figure 6.2 – a) Spatial distribution of centroids for geothermal systems within the metropolitan area of Milan. The size of the blue dots represents the magnitude of cooling energy produced during the summer season for each geothermal plant. b) Frequency bar chart revealing a bimodal Gaussian distribution, characterizing the cooling energy output of the geothermal systems.

Figure 6.3a illustrates the spatial distribution of geothermal systems that generate energy for heating during the winter season. **Figure 6.3b** presents a frequency bar plot corresponding to the data depicted on the map, revealing a uni-modal Gaussian distribution with a prominent peak for medium-sized geothermal systems. This trend can be attributed to a comparatively lower demand for heating energy in medium-to-large-sized plants, opposite trend is shown by moderately sized systems. Notably, geothermal systems that do not produce energy during the winter season were excluded from this analysis.

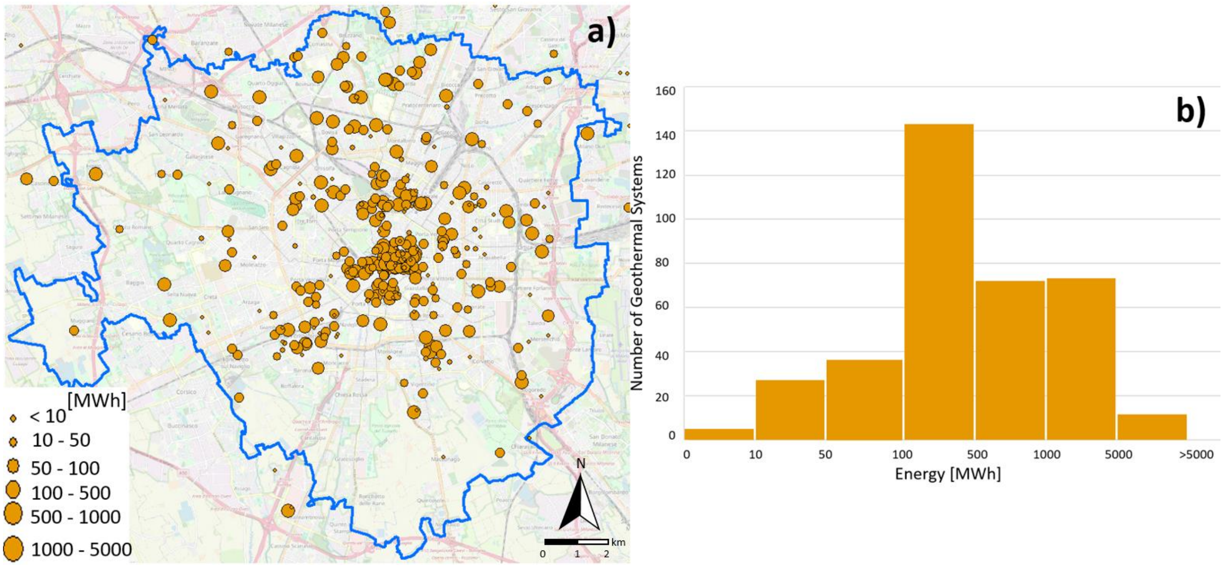

Figure 6.3 – a) Spatial distribution of centroids for geothermal systems within the metropolitan area of Milan. The size of the orange dots represents the magnitude of heating energy produced during the winter season for each geothermal plant. b) Frequency bar plot revealing a unimodal Gaussian distribution spiking for medium-sized plants, characterizing the heating energy output of the geothermal systems.

Further statistical analyses were conducted on the extraction and injection wells. **Figure 6.4** presents a frequency bar chart illustrating the distribution of injection and extraction wells' number across the geothermal systems considered. The most prevalent configuration consists of systems with a single injection and extraction well, followed by those featuring two wells for each purpose.

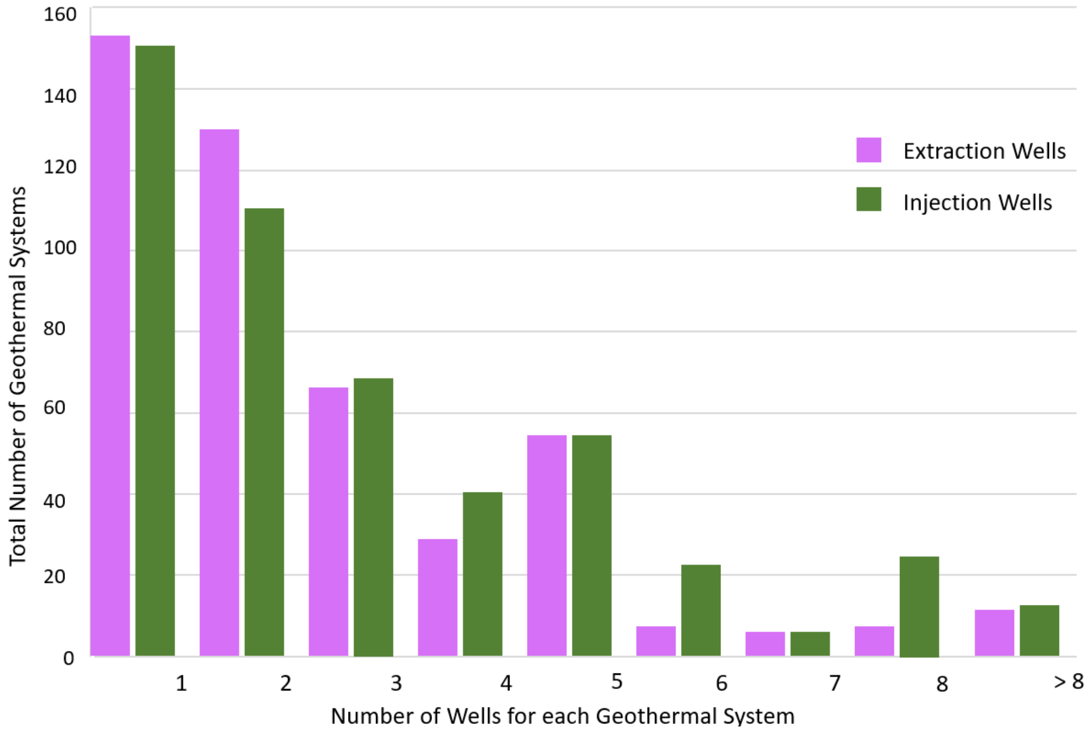

Figure 6.4 – Frequency bar plot depicting the distribution of injection and extraction well counts characterizing each geothermal system considered.

The relative inter-well distance (*d*) was determined by calculating the centroid of the coordinates for both injection and extraction wells, obtained as the average of their respective coordinates. **Figure 6.5** presents a frequency bar plot illustrating the distribution of inter-well distances characterizing each geothermal system under consideration. The bar plot reveals a unimodal distribution, with a prominent peak corresponding to *d* ranging from 30 to 40 meters. It is important to note that the final bin represents systems with *d* exceeding 100 meters, including systems with distances up to 700 meters. This bin was created to emphasize the analysis of *d* below 100 meters, which are of primary relevance for the project.

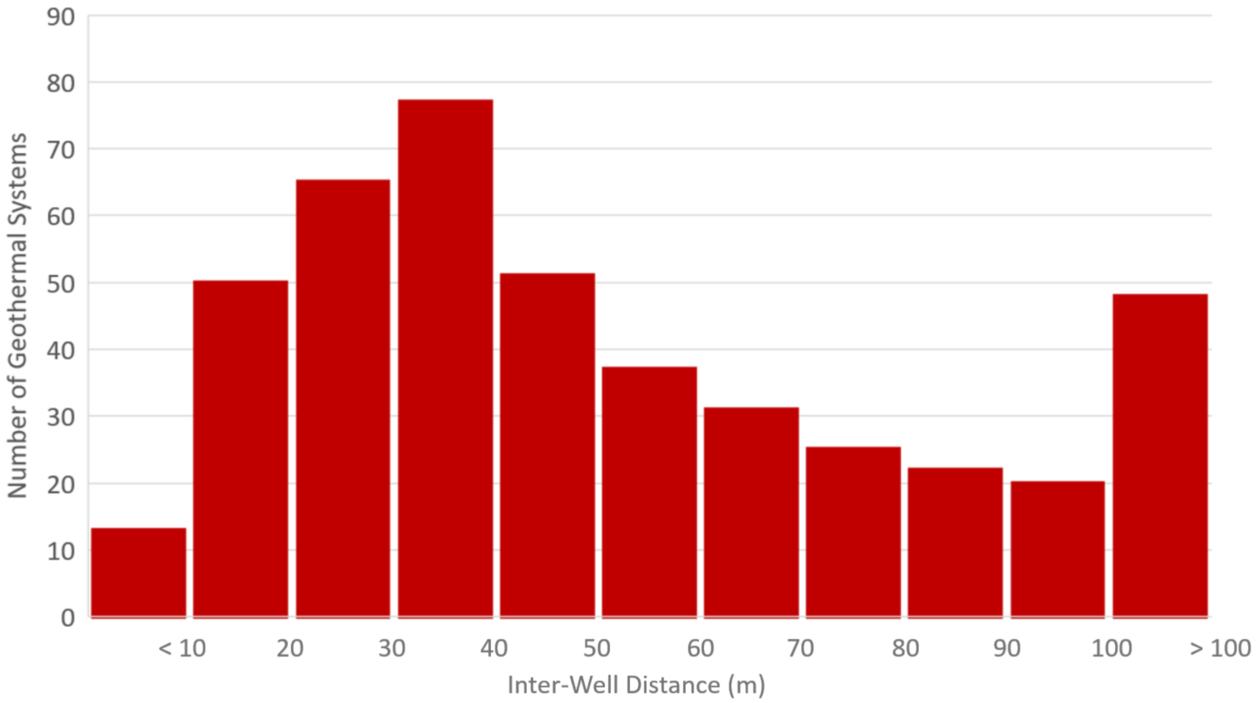

Figure 6.5 – Frequency bar chart highlighting the distribution of the inter-well distances characterising the geothermal systems under consideration.

Figure 6.6 presents a frequency bar plot illustrating the distribution of geothermal system by year of installation. The graph reveals two prominent peaks corresponding to the period between 2019 and 2022, during which approximately 250 geothermal systems were installed in the municipality of Milan. This trend aligns with the introduction of the national decree known as the 'Superbonus 110%,' proposed in 2020. As noted by Confcommercio (2020), this decree "provides for the deduction of 110% of the expenses incurred between 1 July 2020 and 31 December 2021 for specific interventions aimed at increasing the energy efficiency of buildings (ecobonus)," which included the installation of geothermal systems. Therefore, the decree significantly stimulated the adoption of geothermal systems in MCM during the 2019 – 2022 period.

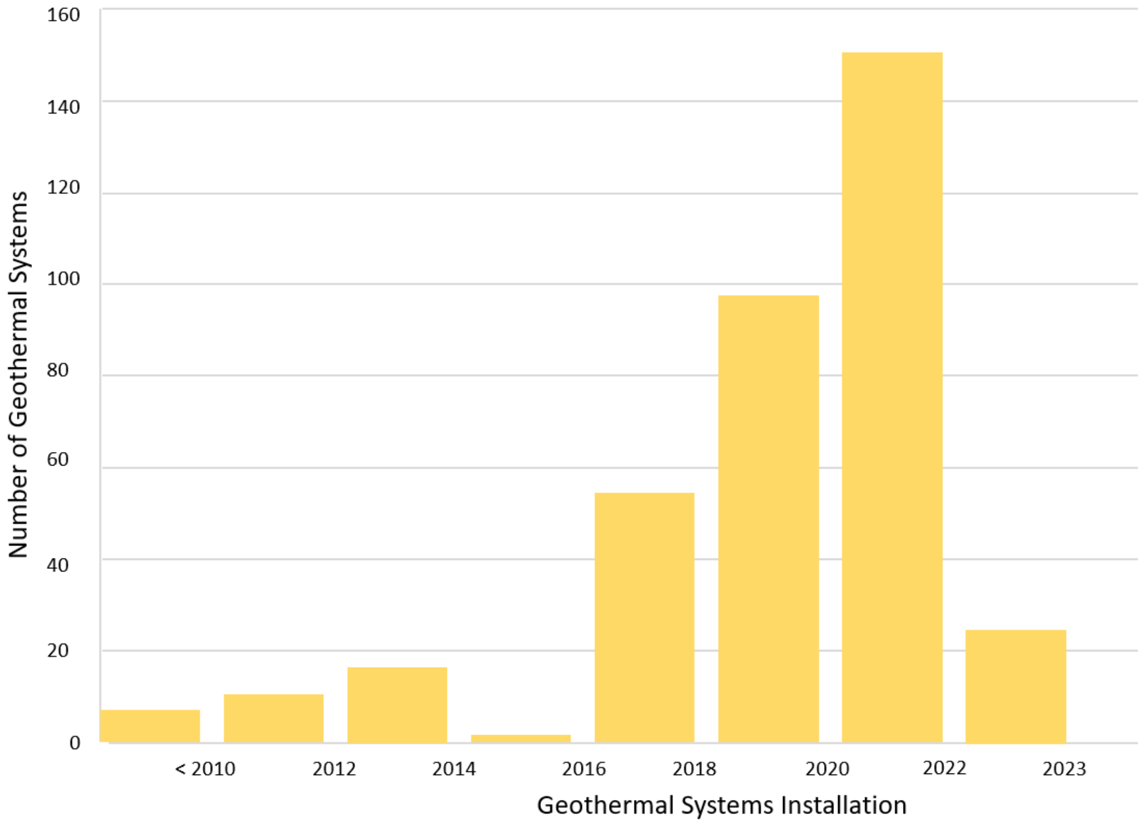

Figure 6.6 - Frequency bar plot depicting the construction of geothermal systems considered in this study, classified according to their year of installation.

6.3 Feasibility assessment of non-conventional geothermal systems in terms of groundwater flow velocity

As demonstrated in chapter 5.4.2, more specifically in **Figure 5.6**, the threshold value for which it is more convenient to install a UD-ATES compared to a traditional ATES is 220 m/y for the smallest storage volume (*V*) considered (100,000 m^3/season). For this reason, the groundwater (GW) flow velocity (*u*) of the MoM was calculated to evaluate which are the most suitable locations for installing one system or the other.

Once a geothermal system has been constructed, a well drawdown test must be carried out to obtain a site-specific transmissivity (*T*). In this study, the *T* was estimated by using Cassan's (1980) method, which takes into account the ratio between the extraction flow rate (*Q*) and the induced drawdown in the well (S_w). Cassan's method is a simplification of Thiem's (1906) method, which is based on the following assumptions:

- The aquifer's thickness (*H*) is constant;
- Hydraulic conductivity is homogeneous (K_h);
- In phreatic aquifers, the drawdown induced by the well extraction is negligible compared to the aquifer thickness ($S_w << H$).

In this method, *T* is determined based on the ratio of *Q* and S_w, obtained by the drawdown tests performed after the construction of each well, and also the relation between θ and σ. These parameters are derived by applying the following formulae:

$$\sigma = \frac{S_w}{i \cdot r_w} \qquad \text{(Eq. 6.1)}$$

$$T = \frac{\theta \cdot Q}{2 \cdot \pi \cdot S_w} \qquad \text{(Eq. 6.2)}$$

For each test, the values of θ were derived from the theoretical curve (**Figure 6.7**) proposed by Cassan (1980).

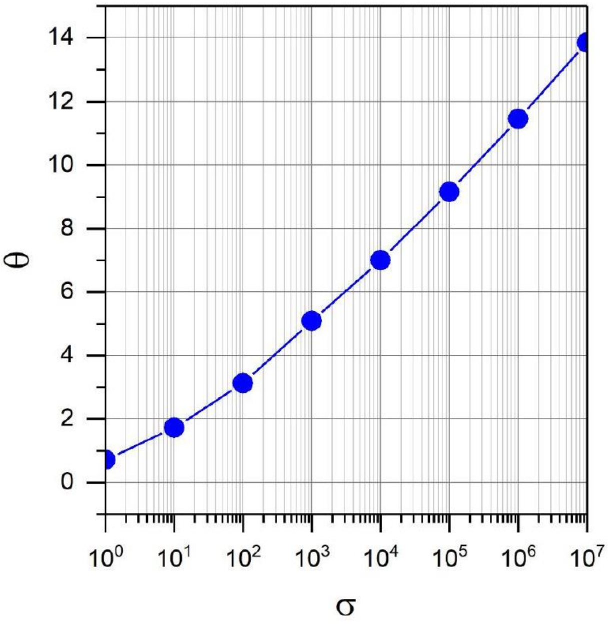

Figure 6.7 - Characteristic curve proposed by Cassan, (1980) showing the relation between θ and σ parameters to obtain the transmissivity (T) from equation 6.2.

All the pointwise information was processed with a linear interpolator (Kriging) to generate a *T* map (**Figure 6.8a**). It was also calculated the horizontal hydraulic conductivity (K_h) with the following relation (eq. 6.1):

$$K_h = \frac{T}{H} \qquad \text{(Eq. 6.3)}$$

Where H represents the aquifer thickness, which was assumed to be homogeneously 40 m (the average thickness of the shallow aquifer in the MoM).

Once the K_h map was obtained, was calculated the Darcy velocity (u_D) (eq. 6.2) shown in map **Figure 6.8d**. This was done with the function raster calculator of ArcMap, which allows to multiply the cells values of one raster with another one. In this way, the K_h map (**Figure 6.8b**) was multiplied by the gradient's (i) raster (**Figure 6.8c**) of September 2022 (retrieved from MoM's website).

$$u_D = K_h \cdot i \qquad \textit{(Eq. 6.4)}$$

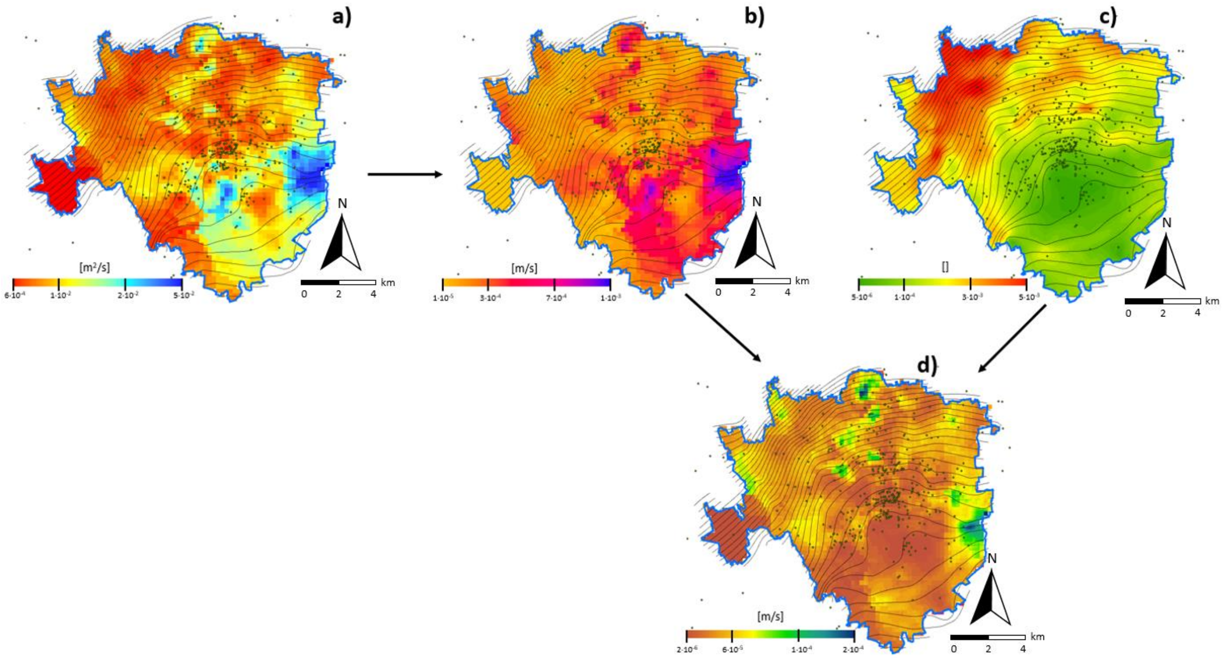

Figure 6.8 – Four rasters show the municipality borders of Milan's municipality illustrating four different parameters a) Transmissivity (T) map [m^2/s], b) Horizontal hydraulic conductivity (K_h) map [m/s], c) Gradient (i) map [], d) Darcy groundwater flow velocity (u_D) map [m/s]. In all four maps, the dots represent the centroid (average of both the injection and extraction wells coordinates) of each geothermal system considered.

By transforming the u_D in real GW flow velocity (u) (eq. 6.3); assuming an effective porosity (ϕ_{eff}) of 0.2 a relation between the two velocities was created:

$$u = \frac{u_D}{\phi_{eff}} \qquad \textit{(Eq. 6.5)}$$

Thermal recovery efficiency

The results of this section will be presented in terms of Thermal recovery efficiency (η_{th}), as it was done for chapter 5.

The energy extracted from the GW by the system was calculated for each time step by multiplying V by the specific heat capacity of water (c_w), by its density (ρ_w) and by the difference between the extraction (T_{ext}) and injection (T_{inj}) temperatures (eq. 5.1).

Within the model, the total energy (E_{season}) was retrieved by summing up all the energy values for each time step (7 days), separately for the two different seasons (summer and winter). From this value, the η_{th} percentage (eq. 5.2) was computed by comparison with the maximum potential seasonal energy (E_{max}) that could be collected in one season for a fixed ΔT of 10°C.
Both E_{season} and η_{th} were retrieved starting from the 5th year of simulation, assuming the average annual temperature downstream of the injection point to reach stationarity with only seasonal oscillations.

Outcomes

Figure 6.9a depicts **Figure 5.6** in relation to a bar chart that illustrates the velocity (u_D and u) distribution in the cells of the considered domain (**Figure 6.9b**). The plot illustrates that by setting a threshold value of 40 m/y or 200 m/y in terms of u_D and u, respectively, the majority of the cells (97%) in the domain are described by a value that is lower than the selected threshold.

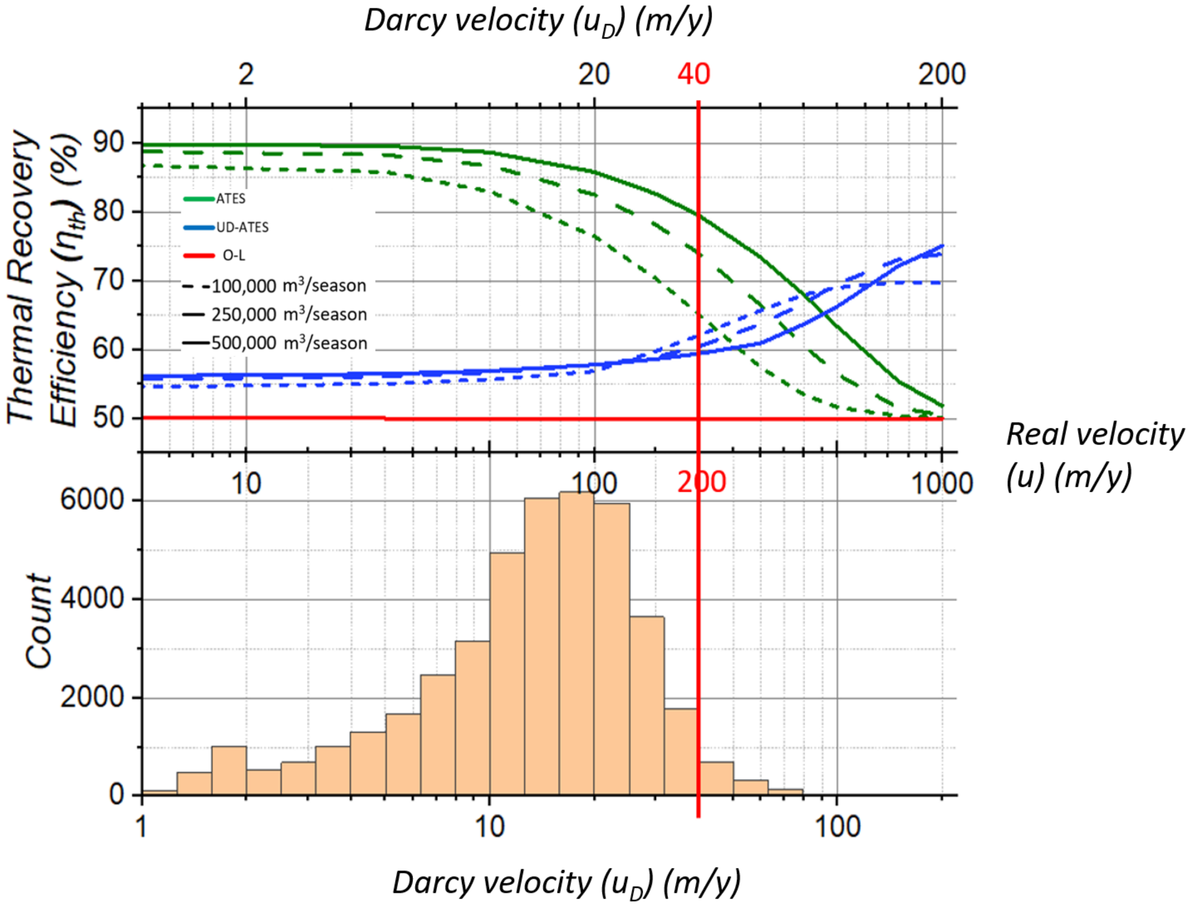

Figure 6.9 – a) As figure 5.6 of Section 5.4.2. b) Frequency bar plot showing the distribution of the GW flow velocity values, both in terms of Darcy velocity (u_D) and real velocity (u). The red line illustrates the parameter for which is more convenient to install a traditional or a uni-direction ATES.

Once the threshold value was selected, a map of the MoM was generated illustrating the areas more suitable for installing traditional or uni-directional ATES (**Figure 6.10**).

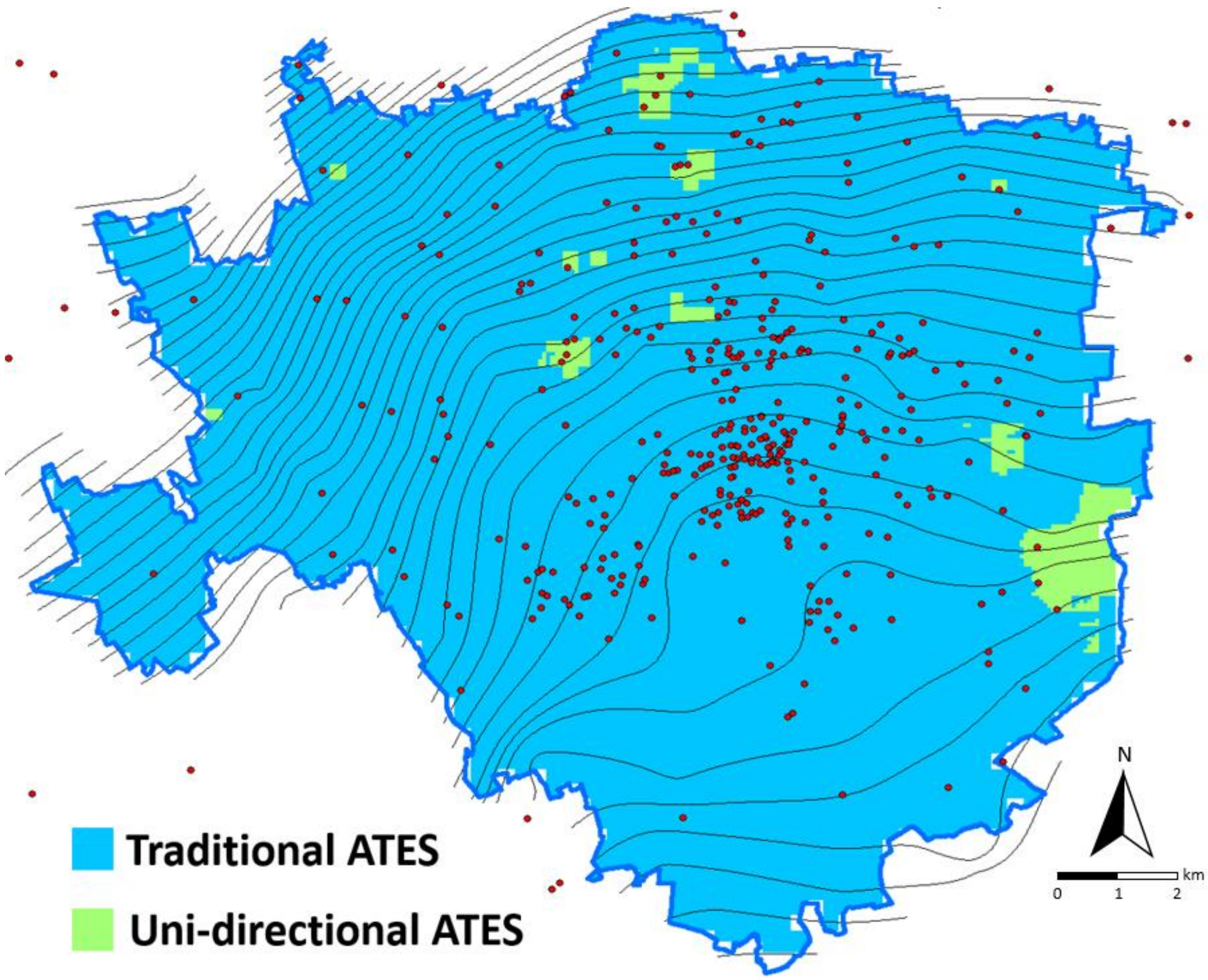

Figure 6.10 – Optimal locations for the installation of traditional or uni-directional ATES geothermal systems in the municipality of Milan. The red dots represent the centroid (of both the injection and extraction wells coordinates) of each geothermal system considered.

6.4 Feasibility assessment for non-conventional geothermal systems in terms of seasonal energy imbalance

As shown in **Figure 5.11** (chapter 5.5.3), also in the worst conditions of imbalance between the two seasons (10% and 100%, respectively) the total increment of η_{th} is greater than 15% compared to a conventional O-L system. To evaluate this relation on the existing geothermal systems in the MoM was assumed that the injection/extraction delta temperature should be constant at 5°C for all the geothermal installations considered in the MoM. Therefore, considering the outcomes of **Figure 5.11** independently on the imbalance of each system is always more convenient to install traditional ATES systems.

Figure 6.11a illustrates the relation between **Figure 5.11** and the frequency bar plot of the volume imbalance of geothermal systems considered in the MoM, retrieved by the ratio between heating and cooling volumes (**Figure 6.11b**). It is highlighted that approximately 75% of the systems exhibit an imbalance below 40%, resulting in increment in η_{th} of over 40% compared to conventional O-L. The theoretical threshold of 40% was established due to the significant decline in efficiency gains observed in systems with imbalances exceeding this value when compared to conventional O-L systems.

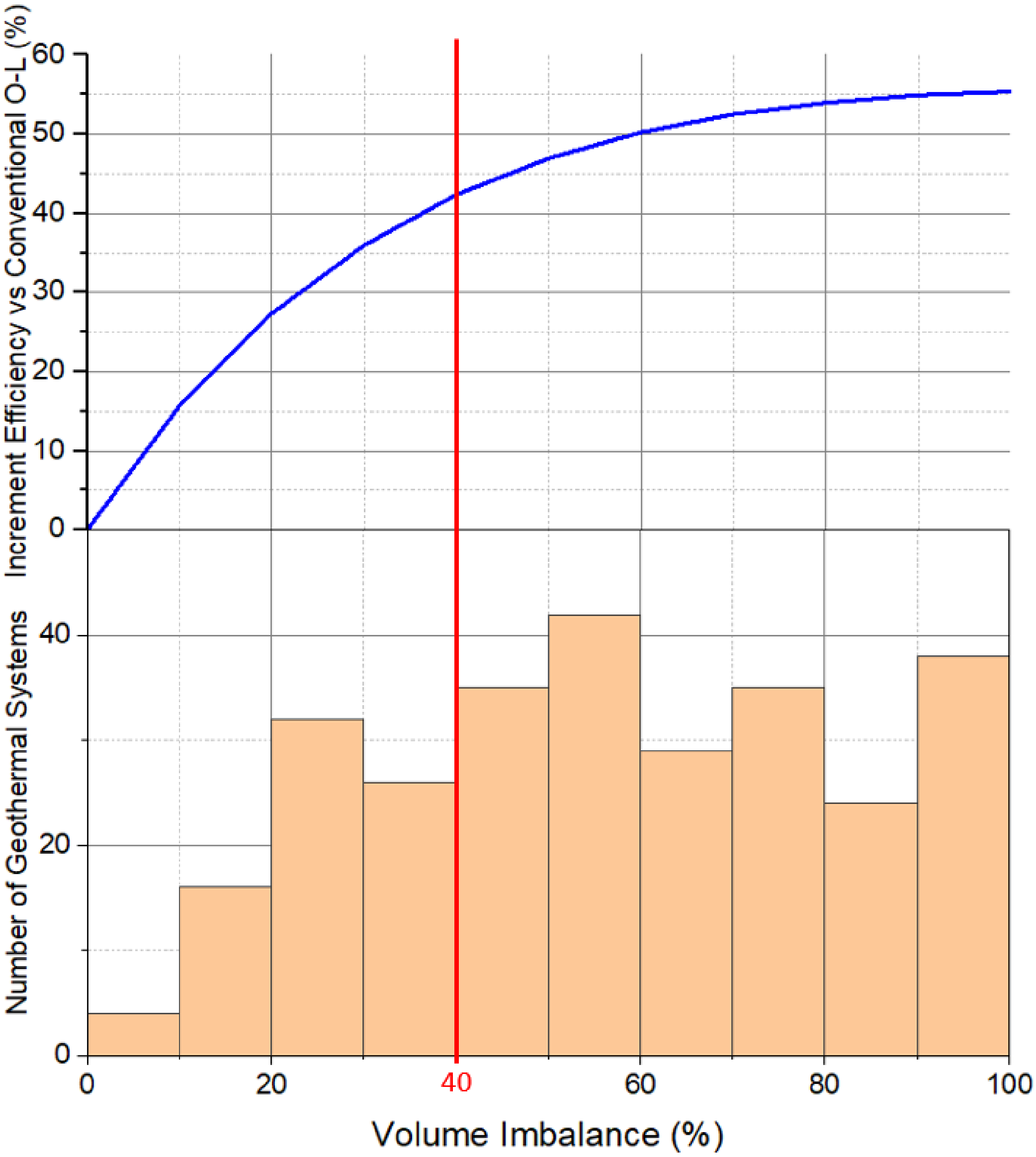

Figure 6.11 – a) As figure 5.10 of Section 5.5.3. b) Frequency bar plot showing the distribution of the volume imbalance of geothermal systems considered in the municipality of Milan. The red line illustrates that almost 80% of the systems are characterised by an imbalance lower than 40%.

Figure 6.12 illustrates the spatial distribution of the geothermal systems considered in the MoM classified according to their imbalance, obtained by the ratio of the heating and cooling volumes. It is important to note that fully imbalanced systems (those in which no water is extracted during either the summer or winter season) were considered not representative.

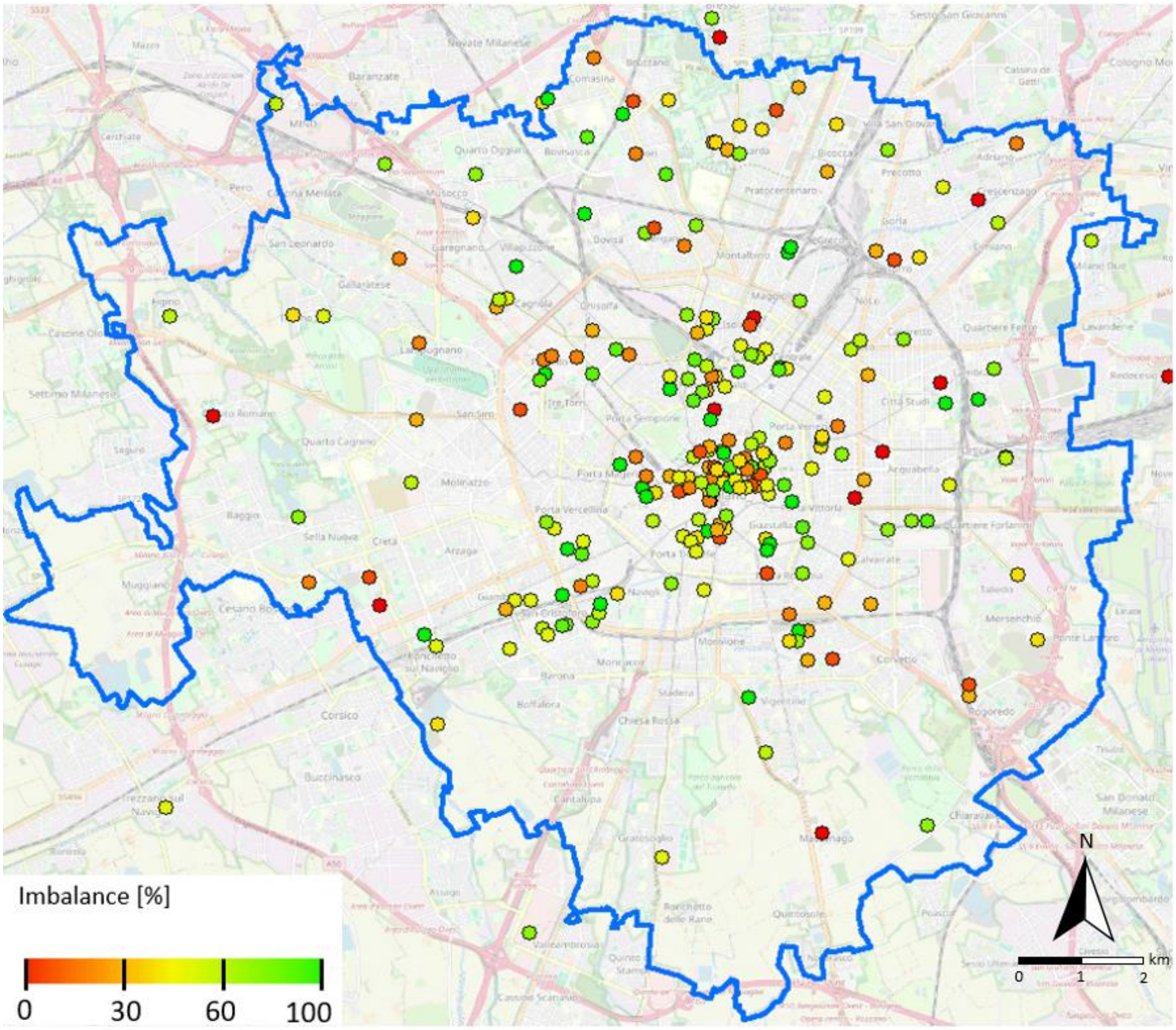

Figure 6.12 – Spatial distribution of the geothermal systems considered in terms of imbalance, obtained by the ratio between heating and cooling volume.

To assess the increment in η_{th} of traditional ATES compared to conventional O-L systems in the existing geothermal installations within the municipality of Milan, it was necessary to make an assumption. A uniform delta temperature of 5 °C was applied across all the considered geothermal systems to enable comparisons with the theoretical conditions analysed in Chapter 5. The first step involved deriving the equation representing the function depicted in **Figure 5.11**, which was obtained through a regression process.

$$y = -58.46 \cdot e^{\left(-x/_{30.8}\right)} + 58.18 \qquad \text{(Eq. 6.6)}$$

Where y is the η_{th} increment relative to a conventional O-L, while x denotes the energy imbalance.

Based on this relationship, a map (**Figure 6.13a**) was generated, where the size of the blue dots indicates the percentage increment in η_{th} when employing a traditional ATES system compared to a conventional O-L system. The red areas on the map correspond to regions where u_D 40 m/year, identifying zones more suitable for the installation of UD-ATES systems. Of the 281 geothermal systems displayed on the map, only 10 are located within these high-velocity areas.

Figure 6.13b visualises the function described in Section 5.5.3, populated with data from the geothermal systems considered in this study, thereby illustrating their distribution along the curve. To further highlight this distribution, a frequency bar plot (**Figure 6.13c**) depicts the number of geothermal systems classified according to their respective increments in η_{th}. The analysis reveals that the most imbalanced systems, which are also the fewest in number, exhibit relatively limited improvements in thermal recovery efficiency when converted into traditional ATES configuration. In contrast, systems with an imbalance of less than 40% experience a significant enhancement in η_{th}, with increments exceeding 40% when converted into traditional ATES systems.

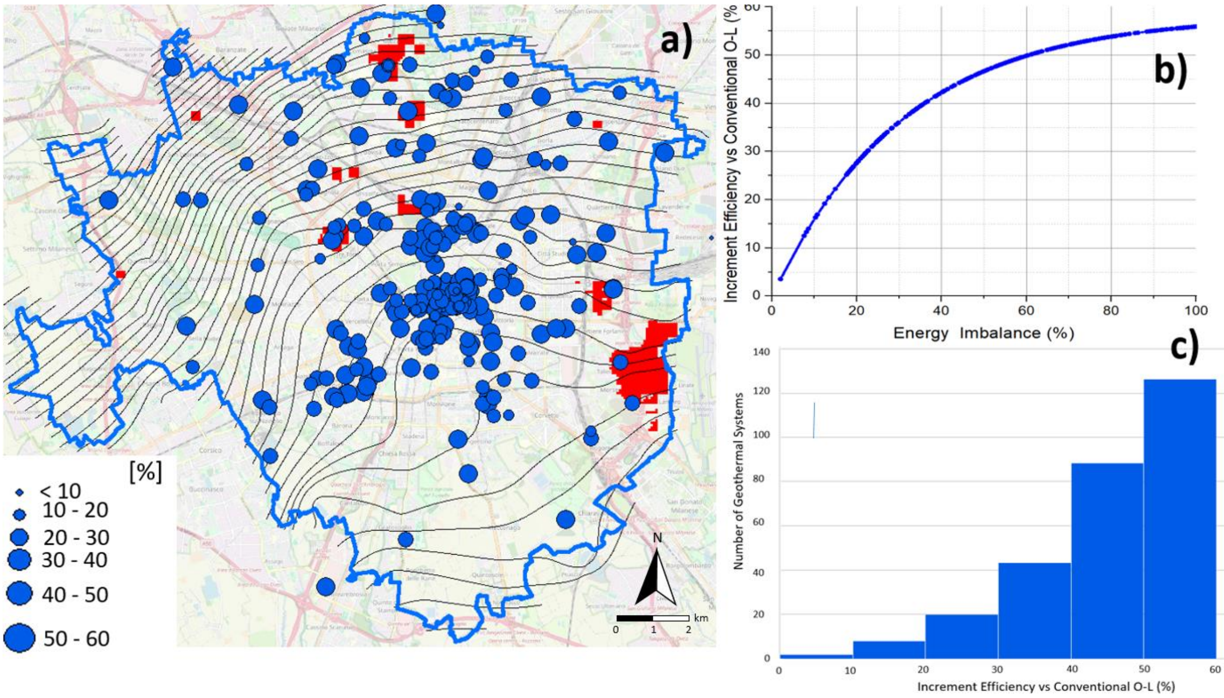

Figure 6.13 - a) Map delineating the borders of the Milan geothermal systems, where the blue dots represent the centroids of the geothermal systems. The size of each dot is proportional to the percentage increase in thermal recovery efficiency that could be achieved by converting the systems into traditional Aquifer Thermal Energy Storage (ATES) systems, assuming a uniform delta temperature of 5°C in all geothermal plants analysed. Areas with groundwater velocities exceeding 40 m/y are highlighted in red, indicating regions where the installation of uni-directional ATES systems would be more advantageous. b) Graph illustrating the

functional relationship used to derive the thermal recovery efficiency increment as a function of the system imbalance. The dots in this graph represent the distribution of the existing geothermal systems. c) Frequency bar plot showing the distribution of geothermal systems according to the percentage increase in thermal recovery efficiency.

7. Conclusions

7.1 Thermal characterisation of soils

The understanding of subsurface materials' thermal conductivity for geothermal applications was deeply analysed in this study. Were employed two instruments, the ThermTest Transient Line Source-100 (TLS-100) needle probe and the Heat Flow Meter (HFM) to measure the thermal conductivity under various saturation and void index conditions. The findings highlighted the complex interplay of factors that influence soil thermal properties.

During the test's performance, several challenges were encountered, primarily related to sample preparation and water distribution. In the case of the TLS-100, early testing methods often produced inconsistent results due to uneven saturation, which created oversaturated zones that produced unreliable measurements. To mitigate this issue, a revised sample preparation method was adopted to ensure uniform saturation. The TLS-100 needle probe demonstrated versatility, allowing measurements to be conducted in situ and in the laboratory on both intact and reconstructed samples. However, the presence of coarse grains occasionally hindered probe insertion, resulting in inconsistent output.

On the other hand, the Heat Flow Meter (HFM), while designed for solid materials, required significant adaptations to test loose soils. The inability of the HFM to handle high saturation levels due to water leakage further highlighted its limitations in this application.

The two instruments used in the study offered both complementary strengths and limitations.

Thermal conductivity was also influenced by the soil's void index, with compacted samples exhibiting higher conductivity. Compaction reduced porosity and improved particle-to-particle contact, facilitating heat transfer. Furthermore, the grain size distribution and mineral composition of the soil played a crucial role in thermal behaviour. Soils rich in sand and quartz showed better conductivity than finer materials like clay and silt, due to the higher thermal conductivity of quartz. The results aligned well with the theoretical model proposed by De Vries, which predict conductivity trends across varying saturation levels and soil compositions. This agreement validated the experimental approaches and highlighted the applicability of these models for assessing soil thermal properties.

Overall, is emphasized the critical importance of precise sample preparation, testing methodologies, and the integration of empirical data with theoretical models.

7.2 Hydrogeological parametrisation

This section will be focused mainly on the outcomes of the activity that I personally carried out, more than how were used to implement the Po plain geodatabase and its relative results.

The integration into a dataset of 165 borehole logs, including grain size distributions and lithological classifications, was used to derive hydraulic conductivity values and define hydrofacies.

The research relied on digitised and standardised datasets encompassing 1485 geological horizons. These datasets included grain size distribution analyses and stratigraphic descriptions. These data were used in empirical equations to calculate the hydraulic conductivity. The data, originally collected from the tube line's construction sites, were supplemented by historical archives. MATLAB tools facilitated the interpolation of different grain size distribution data, ensuring consistency in grain size parameters and enabling accurate hydraulic modelling.

Key hydrofacies were defined using the classification system of the Italian Geotechnical Association (A.G.I.) and by the previous work of De Caro et al. (2020). A total of 26 hydrofacies categories were identified, reflecting variations in gravel, sand, silt, and clay content across the study area.

Empirical equations formulas were applied to calculate hydraulic conductivity values for these hydrofacies. These equations proved effective in capturing the variability of hydraulic properties, gravel-dominated hydrofacies exhibited the highest hydraulic conductivity values, reflecting significant permeability, whereas clay-rich classes showed the lowest due to their fine texture and cohesive nature. Silt-rich sediments, while often misidentified due to visual biases, revealed intermediate properties, emphasizing the importance of accurate classification. Notably, the tendency to label fine-grained samples as "clay" when they were predominantly silt underlines the critical need for objective, quantitative approaches in soil classification. By linking hydrofacies to corresponding hydraulic conductivity and porosity values, the research provided a practical methodology to predict subsurface hydraulic behaviour, crucial for urban infrastructure development and water resource management.

7.3 Numerical model generation

The core of this study emphasized the critical insights gained from the numerical modelling and sensitivity analysis of Aquifer Thermal Energy Storage (ATES) systems, with a focus on the novel Uni-Directional ATES (UD-ATES) configuration. The chapter demonstrates that numerical modelling, using MODFLOW’s MT3DMS code, provides a robust framework for evaluating the thermal recovery efficiency (η_{th}) of various ATES configurations under different groundwater (GW) flow velocities, inter-well distances, and storage volumes. The model revealed that UD-ATES offers significant efficiency gains, particularly in aquifers with high GW flow velocities, compared to open-loop (O-L) systems. The ability to recover a greater proportion of stored thermal energy from downstream wells, by utilizing the natural GW flow to transfer heat, is one of the outcomes of the analysis.

For traditional ATES systems, efficiency decreases with higher GW velocities due to the dispersion of thermal energy away from the well, leading to losses in stored heat. UD-ATES configuration proves especially effective at velocities above 220 m/year, where the thermal recovery efficiency surpasses that of traditional ATES. The model shows that, for higher velocities (above 500 m/year), UD-ATES systems achieve a thermal recovery efficiency that is up to 25% higher than conventioanl O-L systems. In contrast, for velocities below 220 m/year, traditional ATES systems remain more effective due to the reduced likelihood of thermal energy being transported away from the extraction well.

Larger storage volumes increase systems efficiency by reducing thermal losses. The results indicate that larger volumes shift the velocity threshold at which UD-ATES outperform traditional ATES to higher GW flow velocities. This is because larger thermal plumes associated with greater storage volumes are less prone to short-circuiting between wells.

Summarising, in UD-ATES, the optimal inter-well distance varies according to the GW velocity and storage volume. At low velocities, shorter distances are sufficient, while higher velocities require larger distances to prevent short-circuiting effects.

One of the key conclusions relates to the thermal pollution downstream of geothermal systems. The analysis revealed that UD-ATES systems produce significantly shorter and less intense thermal plumes compared to traditional ATES and conventional O-L systems, in high GW flow velocities. This is crucial for urban environments, where excessive downstream thermal pollution can interfere with other geothermal systems. The reduced thermal plume length observed in UD-ATES systems is attributed to the strategic placement of wells relative to the storage volume and GW flow velocity, which limits the spread of thermal anomalies beyond the downstream wells. This finding supports the idea that UD-ATES systems are not only more efficient but also more sustainable for the aquifer lifespan.

Finally, the chapter addresses the impact of natural variability in GW flow velocity and direction, aquifer thickness, thermal diffusivity, and seasonal energy imbalances. Changes in GW velocity and flow direction have a minor effect on the efficiency of UD-ATES systems, with only small reductions in efficiency when the flow velocity decreases or shifts by a few degrees. Similarly, variations in aquifer thickness and dispersivity affect thermal plume shape but do not significantly reduce recovery efficiency. The study also shows that seasonal imbalances in heating and cooling demand can affect the thermal recovery efficiency, but even under extreme imbalance scenarios, the efficiency of UD-ATES remains higher than the one of conventional O-L systems.

The findings underscore the potential of UD-ATES configuration to enhance the sustainability of geothermal energy storage, especially in areas with high groundwater flow velocity, and highlight the importance of precise aquifer characterization to achieve optimal design. The conclusions of this chapter provide essential guidance for the development, regulation, and deployment of future ATES systems in both urban and non-urban environments.

7.4 Integration of existing databases and regional scale modelling of geothermal plants

The final section emphasized the critical role of data integration, statistical analysis, and regional-scale modelling in optimizing the efficiency of geothermal systems in the Metropolitan City of Milan. By consolidating 1,069 permits into a comprehensive geodatabase, Milan’s authorities and stakeholders can better understand system distribution, well configurations, and operational patterns, which previously lacked proper oversight. This effort addresses key challenges faced by local authorities, especially for the absence of an organized database to monitor geothermal installations, leading to inefficient system placement, short-circuit flow, and increased operational costs (OPEX) for users.

The statistical analysis of the database revealed notable trends in system design and performance. The concentration of geothermal systems in Milan’s city centre, combined with the spatial distribution of heating and cooling demands, demonstrated the importance of system location in influencing efficiency. The analysis also highlighted a bimodal distribution in the energy production capacity of geothermal systems, with peaks corresponding to medium-sized and medium-to large-sized installations. Seasonal energy production for heating and cooling exhibited distinct patterns, and it was observed that most systems are characterized by a relatively balanced distribution of energy production between the two seasons. This balance has significant implications for thermal recovery efficiency, as imbalanced systems are associated with lower efficiency. Was also identified the optimal locations for converting conventional open-loop geothermal systems into traditional ATES or uni-directional ATES configurations, according to the groundwater velocity characterising a specific area. The analysis showed that 97% of Milan's shallow aquifer has a groundwater flow velocity below the 200 m/year threshold, which is the limit where traditional ATES systems are preferred over uni-directional ATES. This finding provides a basis for targeted system upgrades that could significantly enhance efficiency.

Another key outcome of the study was the assessment of energy imbalance between summer cooling and winter heating in existing geothermal systems. Plants with high imbalance have reduced thermal recovery efficiency, and the study revealed that about 75% of Milan’s geothermal systems exhibit an imbalance below 40%. This indicates a strong opportunity to convert existing systems into traditional ATES, which can achieve efficiency gains of over 40% compared to conventional O-L systems. This potential efficiency improvement is particularly relevant given the current focus on energy savings and aquifer’s sustainability in urban areas.

The study underscores the need for clear guidelines and regulatory frameworks to promote the use of ATES and uni-directional ATES systems, especially in densely populated cities like Milan. It suggests that policymakers should consider revising permitting criteria to ensure that future installations are better spaced and aligned with system performance goals. Furthermore, the research proposes that policymakers adopt a system for monitoring thermal pollution and thermal imbalances to prevent conflicts between users and to support the equitable distribution of geothermal resources.

7.5 Conclusive remarks

This study explored key aspects of geothermal energy systems, focusing on thermal characterization, hydrogeological parametrization, numerical modelling of Aquifer Thermal Energy Storage (ATES) systems, and the integration of regional data for optimizing geothermal plant operations in Milan.

Thermal conductivity, critical for assessing geothermal potential, was evaluated using two instruments: the ThermTest Transient Line Source - 100 needle probe and the Heat Flow Meter. The results revealed the significance of factors like saturation, void index, and grain composition in influencing thermal properties. Challenges in sample preparation and instrument limitations highlighted the need for precise methodologies.

Hydrogeological analysis incorporated data from 1,485 geological horizons and 165 borehole logs to define hydrofacies and calculate hydraulic conductivity. Gravel-dominated hydrofacies exhibited high permeability, while clay and silt showed lower values, emphasizing the need for accurate classification.

Numerical modelling, using MODFLOW’s MT3DMS code, demonstrated the efficiency of the uni-directional ATES configuration, particularly in high groundwater flow environments. Compared to traditional ATES, uni-directional ATES systems achieved up to 25% higher thermal recovery efficiency at GW velocities exceeding 500 m/year. These systems also generated shorter thermal plumes, reducing downstream thermal pollution and enhancing sustainability.

In Milan, the integration of 1,069 geothermal permits into a geodatabase revealed inefficiencies in system placement and operations. Statistical analysis identified optimal locations for converting open-loop systems to ATES or uni-directional ATES. About 97% of the aquifer exhibited GW velocities favouring traditional ATES, with potential efficiency improvements exceeding 40%.

The findings underscore the importance of precise characterization, robust modelling, and data-driven policies to maximize geothermal efficiency while minimizing environmental impacts.

Acknowledgements

This work was realized thanks to the PON funding related to the project named “BICMIB - Blue-green infrastructures for the City of Milano in Bicocca”, which funded also the abroad period at TU Delft with the supervision of Martin Bloemendal. Special acknowledgment is extended to the geothermal research team at the University of Milan-Bicocca for their collaboration with me. Furthermore, sincere gratitude is owed to ARUP for hosting me during a six-month internship.

References

1. A. G. I. (1963). Nomenclatura geotecnica e classifica delle terre. Geotecnica, 4, 275-286.
2. Aimar, F. (2023). Limiting soil sealing and depaving: local actions for regenerating public spaces to build green infrastructures. In Green Infrastructure: Planning Strategies and Environmental Design (pp. 127-137). Cham: Springer International Publishing.
3. Alberto, P., & Crosta, G. B. (2021). Characterization of the subsurface urban heat island and its sources in the Milan city area, Italy. *Hydrogeology Journal*, *29*(7), 2487-2500.
4. Al-Khoury, R. (2011). *Computational modeling of shallow geothermal systems*. CRC press.
5. Alrtimi, A., Rouainia, M., & Haigh, S. (2016). Thermal conductivity of a sandy soil. Applied Thermal Engineering, 106, 551-560.
6. ASTM, D. (2006). Standard test methods for maximum index density and unit weight of soils using a vibratory table. *D4253-00*.
7. ASTM, D. (2006). Standard test methods for minimum index density and unit weight of soils and calculation of relative density. *D4254-00*.
8. ASTM, D. (2022). Standard test method for determination of thermal conductivity of soil and rock by thermal needle probe procedure. D5334-22
9. ASTM, E. (2013). 1225,"Standard test method for thermal conductivity of solids using the guarded-comparative-longitudinal heat flow technique,". Standard, West Conshohocken, PA.
10. Bakker, M., Post, V., Langevin, C.D., Hughes, J.D., White, J.T., Starn, J.J., Fienen, M.N. 2016. Scripting MODFLOW model development using Python and FloPy. Groundwater 54(5), 733-739.
11. Banks, D. (2009). An introduction to 'thermogeology' and the exploitation of ground source heat. Quarterly Journal of Engineering Geology and Hydrogeology
12. Barry-Macaulay, D., Bouazza, A., Singh, R. M., Wang, B., & Ranjith, P. G. (2013). Thermal conductivity of soils and rocks from the Melbourne (Australia) region. Engineering Geology, 164, 131-138.
13. Bayer, P., Attard, G., Blum, P., & Menberg, K. (2019). The geothermal potential of cities. *Renewable and Sustainable Energy Reviews*, *106*, 17-30.
14. Bayer, P., Saner, D., Bolay, S., Rybach, L., & Blum, P. (2012). Greenhouse gas emission savings of ground source heat pump systems in Europe: A review. *Renewable and Sustainable Energy Reviews*, *16*(2), 1256-1267.
15. Beernink, S., Hartog, N., Vardon, P.J., Bloemendal, M. 2024. Heat losses in ATES systems: The impact of processes, storage geometry and temperature. Geothermics 117, 102889.
16. Beg, M. N. A., Carvalho, R. F., & Leandro, J. (2018). Effect of surcharge on gully-manhole flow. Journal of Hydro-environment Research, 19, 224-236.
17. Bloemendal, M., & Hartog, N. (2018). Analysis of the impact of storage conditions on the thermal recovery efficiency of low-temperature ATES systems. *Geothermics*, *71*, 306-319.
18. Bloemendal, M., & Olsthoorn, T. (2018). ATES systems in aquifers with high ambient groundwater flow velocity. *Geothermics*, *75*, 81-92.

19. Bloemendal, M., Jaxa-Rozen, M., Olsthoorn, T. 2018. Methods for planning of ATES systems. Applied Energy 216, 534-557.
20. Bloemendal, M., Olsthoorn, T., & Boons, F. (2014). How to achieve optimal and sustainable use of the subsurface for Aquifer Thermal Energy Storage. *Energy Policy*, *66*, 104-114.
21. Blum, P., Campillo, G., Münch, W., & Kölbel, T. (2010). CO2 savings of ground source heat pump systems–A regional analysis. *Renewable Energy*, *35*(1), 122-127.
22. Brear, R. (2018). Blue and green cities. The role of blue-green infrastructure in managing urban water resources.
23. Bristow, K. L., Kluitenberg, G. J., Goding, C. J., & Fitzgerald, T. S. (2001). A small multi-needle probe for measuring soil thermal properties, water content and electrical conductivity. Computers and electronics in agriculture, 31(3), 265-280.
24. Bundschuh, J., & Arriaga, M. S. (2010). Introduction to the numerical modeling of groundwater and geothermal systems. *Introduction to the Numerical Modeling of Groundwater and Geothermal Systems*, 217-284.
25. Burrato, P., Ciucci, F., & Valensise, G. (2003). An inventory of river anomalies in the Po Plain, Northern Italy: evidence for active blind thrust faulting. Annals of Geophysics.
26. Capodaglio, P., Baietto, A., Casasso, A., Della Valentina, S., Andorno, E., Caldera, D., Saggese, M., Rajver, D., Bucci, A., Böttcher, F., Zambelli, P. & Olmedo, M. (2018): Geotermia a bassa entalpia: aspetti ambientali, energetici ed economici. Il Progetto INTERREG Spazio Alpino GRETA in Valle d'Aosta. GRETA project booklet, ARPA, Aosta, 85 p.
27. Casasso, A., & Sethi, R. (2017). Models and tools for the assessment of thermal-short circuit in open-loop geothermal systems. RENDICONTI ONLINE DELLA SOCIETÀ GEOLOGICA ITALIANA, 42, 50-53.
28. Cassan, M. (1980). Les essais d'eau dans la reconnaissance des sols.
29. Castiglioni, S., Valsecchi, S., Polesello, S., Rusconi, M., Melis, M., Palmiotto, M., Manenti, A., Davoli, E. & Zuccato, E. (2015). Sources and fate of perfluorinated compounds in the aqueous environment and in drinking water of a highly urbanized and industrialized area in Italy. Journal of hazardous materials, 282, 51-60.
30. Chae, H., Nagano, K., Sakata, Y., Katsura, T., Kondo, T. 2020. Estimation of fast groundwater flow velocity from thermal response test results. Energy and Buildings, 206.
31. Clauser, C., & Huenges, E. (1995). Thermal conductivity of rocks and minerals. *Rock physics and phase relations: a handbook of physical constants*, *3*, 105-126.
32. Constantz, J. (1998). Interaction between stream temperature, streamflow, and groundwater exchanges in alpine streams. Water resources research, 34(7), 1609-1615.
33. De Caro, M., 2018. PhD Thesis: Analysis of groundwater environment change in the Milan Metropolitan area by hydrostratigraphic, groundwater quality and flow modelling.
34. De Caro, M., Crosta, G. B., Frattini, P., Perico, R., & Volpi, G. (2017). Hydrofacies reconstruction of glaciofluvial aquifers and groundwater flow modelling in a densely urbanized area under changing climatic conditions. Hydrology and Earth System Sciences Discussions, 2017, 1-44.

35. De Caro, M., Crosta, G., Frattini, P., Castellanza, R., Tradigo, F., Mussi, A., & Cresci, P. (2019, September). Blue-green infrastructures and groundwater flow for future development of Milano (Italy). In *Proceedings of the XVII European Conference on Soil Mechanics and Geotechnical Engineering (ECSMGE), Reykjavik, Iceland* (pp. 1-6).
36. De Caro, M., Perico, R., Crosta, G. B., Frattini, P., & Volpi, G. (2020). A regional-scale conceptual and numerical groundwater flow model in fluvio-glacial sediments for the Milan Metropolitan area (Northern Italy). Journal of Hydrology: Regional Studies, 29, 100683.
37. Epting, J., & Huggenberger, P. (2013). Unraveling the heat island effect observed in urban groundwater bodies–Definition of a potential natural state. *Journal of hydrology*, *501*, 193-204.
38. Ertuğrul, N. A., Bağcı, Z. H., & Ertuğrul, Ö. L. (2018). Aquifer thermal energy storage systems: Basic concepts and general design methods. Turkish Journal of Engineering, 2(2), 38-48.
39. Fadejev, J., Simson, R., Kurnitski, J., & Haghighat, F. (2017). A review on energy piles design, sizing and modelling. Energy, 122, 390-407.
40. Farr, G. J., Patton, A. M., Boon, D. P., James, D. R., Williams, B., & Schofield, D. I. (2017). Mapping shallow urban groundwater temperatures, a case study from Cardiff, UK. *Quarterly Journal of Engineering Geology and Hydrogeology*, *50*(2), 187-198.
41. Feng, S., Vardanega, P. J., Ibraim, E., Widyatmoko, I., & Ojum, C. (2019). Permeability assessment of some granular mixtures. Géotechnique, 69(7), 646-654.
42. Ferguson, G., & Woodbury, A. D. (2004). Subsurface heat flow in an urban environment. Journal of Geophysical Research: Solid Earth, 109(B2).
43. Fletcher, T. D., Shuster, W., Hunt, W. F., Ashley, R., Butler, D., Arthur, S., Trowsdale, S., Barraud, S., Semadeni-Davies, A., Bertrand-Krajewski, J.L., Steen Mikkelsen, P., Rivard, G., Uhl, M., Dagenais, D., & Viklander, M. (2015). SUDS, LID, BMPs, WSUD and more–The evolution and application of terminology surrounding urban drainage. *Urban water journal*, *12*(7), 525-542.
44. Fleuchaus, P., Schüppler, S., Godschalk, B., Bakema, G., Blum, P. 2020. Performance analysis of aquifer thermal energy storage (ATES). Renewable Energy 146, 1536-1548.
45. Freeze, R.A., Cherry, J.A., 1979. Groundwater.
46. Gago, E. J., Roldan, J., Pacheco-Torres, R., & Ordóñez, J. (2013). The city and urban heat islands: A review of strategies to mitigate adverse effects. Renewable and sustainable energy reviews, 25, 749-758.
47. Gambini, E., Ceppi, A., Ravazzani, G., Mancini, M., Valsecchi, I. Q., Cucchi, A., Negretti, A. & Tolone, I. (2024). An empirical rainfall threshold approach for the civil protection flood warning system on the Milan urban area. Journal of Hydrology, 628, 130513.
48. Garzanti, E., Vezzoli, G., & Andò, S. (2011). Paleogeographic and paleodrainage changes during Pleistocene glaciations (Po Plain, northern Italy). Earth-Science Reviews, 105(1-2), 25-48.
49. Ghofrani, Z., Sposito, V., & Faggian, R. (2017). A comprehensive review of blue-green infrastructure concepts. *International Journal of Environment and Sustainability*, *6*(1).
50. Hähnlein, S., Bayer, P., Ferguson, G., & Blum, P. (2013). Sustainability and policy for the thermal use of shallow geothermal energy. Energy Policy, 59, 914-925.

51. Harbaugh, A.W., Banta, E.R., Hill, M.C., McDonald, M.G. 2000. Modflow-2000, the U.S. Geological survey modular ground-water model-user guide to modularization concepts and the ground-water flow process.
52. Hemmerle, H., Hale, S., Dressel, I., Benz, S. A., Attard, G., Blum, P., & Bayer, P. (2019). Estimation of groundwater temperatures in Paris, France. *Geofluids*, *2019*(1), 5246307.
53. Hoekstra, N., Pellegrini, M., Bloemendal, M., Spaak, G., Gallego, A.A., Comins, J.R., Grotenhuis T., Picone S., Murrell A.J., Steeman H.J., Verrone A., Doornenbal P., Christophersen M., Bennedsen L., Henssen M., Moinier S., Saccani, C. 2020. Increasing market opportunities for renewable energy technologies with innovations in aquifer thermal energy storage. Science of the Total Environment 709, 136142.
54. Hussain, F., & Nabi, G. (2016). Empirical formulae evaluation for hydraulic conductivity determination based on grain size analysis. Pyrex Journal of Research in Environmental Studies, 3(3), 26-32.
55. ISTAT Demographic Statistics, (2023). Profili delle città metropolitane: Molte fragilità ma anche potenzialità dei contesti urbani. Istituto Nazionale di Statistica, Roma. https://www.istat.it/it/files/2023/02/Statistica-Focus-Citt%C3%A0-Metropolitane.pdf
56. Kappelmeyer, O., & Haenel, R. (1974). Geothermics with special reference to application. *Berlin gebrueder borntraeger geoexploration monographs series*, *4*, 31.
57. Kasenow, M. (2002). Determination of hydraulic conductivity from grain size analysis. Water Resources Publication.
58. Kaufman, L. P., Strickland, E. A., & Benavidez, A. A. (1979). Suggested method for the calibration of vibrating tables for maximum index density testing. Geotechnical Testing Journal, 2(3), 152-157.
59. Kavanaugh, S. P., & Rafferty, K. D. (2014). Geothermal heating and cooling: design of ground-source heat pump systems. (ASHRAE).
60. Kolawole, F., & Evenick, J. C. (2023). Global distribution of geothermal gradients in sedimentary basins. *Geoscience Frontiers*, *14*(6), 101685.
61. Kurylyk, B. L., MacQuarrie, K. T., Caissie, D., & McKenzie, J. M. (2015). Shallow groundwater thermal sensitivity to climate change and land cover disturbances: derivation of analytical expressions and implications for stream temperature modeling. Hydrology and Earth System Sciences, 19(5), 2469-2489.
62. Low, J., Loveridge, F. A., & Powrie, W. (2014). Thermal conductivity of soils by the needle probe method, for energy foundation applications.
63. Lyons, L., Lecomte, E., Georgakaki, A., Letout, S., & Mountraki, A. (2022). Clean Energy Technology Observatory: Heat pumps in the European Union-2023 Status Report on Technology Development, Trends, Value Chains and Markets.
64. Martinis, B., & Mazzarella, S. (1971). Prima ricerca idrica profonda nella pianura lombarda. Mem. Ist. Geol. Minerl. Uinv. Padova
65. Martinis, B., Mazzarella, S., 1971. Prima ricerca idrica profonda nella pianura lombarda. Mem. Ist. Geol. e Min. Univ. Padova.
66. Menberg, K., Blum, P., Kurylyk, B. L., & Bayer, P. (2014). Observed groundwater temperature response to recent climate change. Hydrology and Earth System Sciences, 18(11), 4453-4466.
67. Menberg, K., Blum, P., Schaffitel, A., & Bayer, P. (2013). Long-term evolution of anthropogenic heat fluxes into a subsurface urban heat island. *Environmental science & technology*, *47*(17), 9747-9755.

68. Mohammed, M. H., Zwain, H. M., & Hassan, W. H. (2021). Modeling the impacts of climate change and flooding on sanitary sewage system using SWMM simulation: A case study. Results in Engineering, 12, 100307.
69. Muttoni, G., Carcano, C., Garzanti, E., Ghielmi, M., Piccin, A., Pini, R., Rogledi, S. & Sciunnach, D. (2003). Onset of major Pleistocene glaciations in the Alps. Geology, 31(11), 989-992.
70. Odong, J. (2007). Evaluation of empirical formulae for determination of hydraulic conductivity based on grain-size analysis. Journal of American Science, 3(3), 54-60.
71. Pellegrini, M., Bloemendal, M., Hoekstra, N., Spaak, G., Gallego, A. A., Comins, J. R., ... & Steeman, H. J. (2019). Low carbon heating and cooling by combining various technologies with Aquifer Thermal Energy Storage. Science of the Total Environment, 665, 1-10.
72. Previati, A., 2022. PhD Thesis: The subsurface urban heat island in Milan – Anthropogenic heat sources and city-scale modeling of present and future scenarios.
73. Previati, A., Epting, J., & Crosta, G. B. (2022). The subsurface urban heat island in Milan (Italy)-A modeling approach covering present and future thermal effects on groundwater regimes. Science of the Total Environment, 810, 152119.
74. Re, V., De Filippis, G., Viaroli, S., & Di Curzio, D. (2020). Groundwater (Freeze and Cherry, 1979), ora disponibile anche in italiano. Acque Sotterranee-Italian Journal of Groundwater, 9(1).
75. Regione Lombardia (2017), Decreto Giunta Regionale, DGR/6293/17, ”Definition of the implementation methods and content of the preventive studies required by LR 38/2015, for the purpose of authorising the discharge of groundwater extracted for heat pump heat exchange into the aquifer”.
76. Regione Lombardia, 2016. PTUA 2016. Elaborato 2: caratterizzazione, monitoraggio e classificazione dei corpi idrici sotterranei [WWW Document]. URL https://www.regione.lombardia.it/wps/portal/istituzionale/HP/DettaglioRedazionale/servizi-e-informazioni/Enti-e-Operatori/territorio/governo-delle-acque/piano-tutela-acque-pta/piano-tutela-acque-pta
77. Regione Lombardia, ENI, 2002. Geologia degli acquiferi padani della Regione Lombardia. SELCA, Firenze.
78. Regione Lombardia, ENI, 2002. Geologia degli acquiferi padani della Regione Lombardia. SELCA, Firenze.
79. Rostampour, V., Jaxa-Rozen, M., Bloemendal, M., Kwakkel, J., & Keviczky, T. (2019). Aquifer Thermal Energy Storage (ATES) smart grids: Large-scale seasonal energy storage as a distributed energy management solution. *Applied Energy*, *242*, 624-639.
80. Saner, D., Juraske, R., Kübert, M., Blum, P., Hellweg, S., & Bayer, P. (2010). Is it only CO2 that matters? A life cycle perspective on shallow geothermal systems. *Renewable and Sustainable Energy Reviews*, *14*(7), 1798-1813.
81. Scott, S., Driesner, T., & Weis, P. (2016). The thermal structure and temporal evolution of high-enthalpy geothermal systems. *Geothermics*, *62*, 33-47.
82. Self, S. J., Reddy, B. V., & Rosen, M. A. (2013). Geothermal heat pump systems: Status review and comparison with other heating options. *Applied energy*, *101*, 341-348.

83. Sprenger, C., Hartog, N., Hernández, M., Vilanova, E., Grützmacher, G., Scheibler, F., Hannappel, S. 2017. Inventory of managed aquifer recharge sites in Europe: historical development, current situation and perspectives. Hydrogeology Journal 25(6), 1909.
84. Standard, A. S. T. M. (2021). C518; Standard Test Method for Steady-State Thermal Transmission Properties by Means of the Heat Flow Meter Apparatus. ASTM International: West Conshohocken, PA, USA.
85. Stemmle, R., Rostampour, H., Blum, P., & Menberg, K. (2024). City-scale heating and cooling with aquifer thermal energy storage (ATES). *Geothermal Energy*, *12*(1), 2.
86. Thiem, G., (1906). Hydrologische Methoden: Gebhardt, Leipzig.
87. TLS-100 Portable Meter user manual
88. Tzoulas, K., Korpela, K., Venn, S., Yli-Pelkonen, V., Kaźmierczak, A., Niemela, J., & James, P. (2007). Promoting ecosystem and human health in urban areas using Green Infrastructure: A literature review. *Landscape and urban planning*, *81*(3), 167-178.
89. Vardon, P., Bruhn, D., Steiginga, A., Cox, B., Abels, H., Barnhoorn, A., Drijkoningen, G., Slob, E. & Wapenaar, K. (2020). A geothermal well doublet for research and heat supply of the TU Delft Campus. *arXiv preprint arXiv:2003.11826*.
90. VDI 4640/2, 2001. Thermal use of the underground (German guidelines) – Ground source heat pump systeems.
91. Visser, P. W., Henk, K., Bense, V., & Emiel, B. (2020). Impacts of progressive urban expansion on subsurface temperatures in the city of Amsterdam (The Netherlands). Hydrogeology Journal, 28(5), 1755-1772.
92. Wild, T., Fuchs, G., & Davis, M. (2024). Sitting in our own soup? Combined sewers, climate change and nature-based solutions for urban water management in Berlin. Nature-Based Solutions, 5, 100113.
93. Woodside, W. M. J. H., & Messmer, J. H. (1961). Thermal conductivity of porous media. I. Unconsolidated sands. *Journal of applied physics*, *32*(9), 1688-1699.
94. Woodside, W. M. J. H., & Messmer, J. H. (1961). Thermal conductivity of porous media. I. Unconsolidated sands. *Journal of applied physics*, *32*(9), 1688-1699.
95. Yang, L., Qian, F., Song, D. X., & Zheng, K. J. (2016). Research on urban heat-island effect. Procedia engineering, 169, 11-18.
96. Zheng, C., & Wang, P. P. 1999. MT3DMS: a modular three-dimensional multispecies transport model for simulation of advection, dispersion, and chemical reactions of contaminants in groundwater systems; documentation and user's guide.
97. Zhu, K., Blum, P., Ferguson, G., Balke, K. D., & Bayer, P. (2010). The geothermal potential of urban heat islands. *Environmental Research Letters*, *5*(4), 044002.

Website References

1. Confcommercio: https://www.confcommerciomilano.it/web/news/argomenti_fiscali/Riqualificazione-energetica-degli-edifici-Superbonus-110-pubblicati-in-G.U.-i-decreti-attuativi-per-i-requisiti-tecnici-e-per-lasseverazione/

2. European Commission: https://environment.ec.europa.eu/topics/nature-and-biodiversity/green-infrastructure_en
3. European Council, 2020, “Energy efficiency in buildings”, https://commission.europa.eu/news/focus-energy-efficiency-buildings-2020-02-17_en.
4. European Council, 2021, “Fit for 55”, https://www.consilium.europa.eu/en/policies/green-deal/fit-for-55-the-eu-plan-for-a-green-transition/.
5. IRENA, 2023, “Power to heat and cooling: Status”, https://www.irena.org/Innovation-landscape-for-smart-electrification/Power-to-heat-and-cooling/Status
6. Legambiente, 2021 “Riscaldamento edifici in Italia, studio Elemens: il peso del settore su inquinamento e consumi”, https://www.legambiente.it/comunicati-stampa/riscaldamento-edifici-in-italia-studio-elemens-il-peso-del-settore-su-inquinamento-e-consumi/
7. United Nations: https://www.un.org/uk/desa/68-world-population-projected-live-urban-areas-2050-says-un#:~:text=Calendar-,68%25%20of%20the%20world%20population%20projected%20to%20live%20in%20urban,increase%20to%2068%25%20by%202050.

La borsa di dottorato cofinanziata con risorse del
Programma Operativo Nazionale Ricerca e Innovazione 2014-2020 (CCI 2014IT16M2OP005),
risorse Fondo Sociale Europeo REACT-EU, Azione I.1 “Dottorati Innovativi con caratterizzazione industriale”, Azione IV.4 “Dottorati e contratti di ricerca su tematiche dell’innovazione” e Azione IV.5 “Dottorati su tematiche Green”